# Osteogenic Effect of Magnesium and Its Potential Application for Fracture Healing Enhancement in Ovariectomized Rats

**ZHANG, Yifeng**

**A Thesis Submitted in Partial Fulfilment**

**of the Requirements for the Degree of**

**Doctor of Philosophy**

**in**

**Orthopaedics and Traumatology**

**The Chinese University of Hong Kong**

**May 2015**

## Thesis Assessment Committee

Professor Li Gang (Chair)

Professor Qin Ling (Thesis Supervisor)

Professor Zheng Yufeng (Thesis Co-supervisor)

Professor Cheung Wing Hoi (Committee Member)

Professor Leung Kwok Sui (Committee Member)

Professor Ding Ming (External Examiner)

Professor Lu Jian (External Examiner)

# Declaration

The experiments and studies documented in this dissertation were performed within the Department of Orthopaedics and Traumatology, the Chinese University of Hong Kong, between September 2011 and January 2015. The author assumes full responsibility for all the work described in this dissertation and affirms that no part was submitted by any other researcher for academic credit.

# Abstract

In the rodent femur, almost 99% of all sensory nerves are distributed densely in the periosteum. Neuropeptides encapsulated in the synaptic vesicles are located at the axon terminals and released through exocytosis after being stimulated at the sensory nerve endings. The neuropeptides released from nerve endings have an osteo-anabolic effect on osteoblasts. Among the many kinds of neuropeptides, which include α-calcitonin gene-related peptide (CGRP), substance P, and other amino molecules, CGRP is the classical and dominantly distributed peptide in sensory nerve endings. In aged animals, decreased serum CGRP and loss of bone Mg content may be the factors inhibiting fracture healing.

In this study, Mg was found to significantly promote new bone formation in the subperiosteal cortical region after it was intramedullarily implanted in the rat femur canal. Histomorphological analysis revealed that the newly formed bone grew from periosteum, a fibrous membrane constituted of blood vessels, sensory serves, and mesenchymal stem cells, and did not form any cartilage-like tissue, the latter of which is a feature of intramembranous ossification. Observation that Mg-induced new bone formation disappeared at the periosteum-stripped region revealed the existence of an interaction between the periosteum and Mg ions.

Based on previous findings, this study examined the following hypotheses: (1) Mg ions from Mg implanted in the rat femur canal act on sensory nerve endings in the periosteum and promote neuropeptide CGRP release, (2) mass CGRP release in the periosteum promotes periosteum-derived stem cells osteoblastogenesis and leads to new bone formation. Mg ions affect synaptic replasticity in dorsal root ganglia neurons, and (3) pure Mg metal affects fracture healing in ovariectomized (OVX) rats. **Neuropeptide CGRP plays a pivotal role in Mg-induced new bone formation.**

This hypothesis was supported by femur bone analysis showing that CGRP content significantly increased in Mg-implanted femur bone compared to control femur bone. When rat sensory nerves were destroyed by administration of high-dose capsaicin, induction of new bone formation by Mg implantation significantly decreased, proving that sensory nerves play an important role in Mg-induced osteogenesis. Because neuropeptide CGRP from sensory nerve endings may play a pivotal role in Mg's osteogenic process, the effective CGRP antagonist BIBN4096bs was administered to Mg-implanted rats. Administration of the CGRP antagonist significantly reduced newly formed bone volume after Mg implantation. To examine whether this phenomenon is dependent on the interaction between neuropeptides and MSCs, which are richly distributed in the periosteum, periosteum-derived stem cells (PDSCs) and bone marrow-derived mesenchymal stem cells (BMSCs) were isolated from the periosteum and bone marrow, respectively. It was observed that high concentrations of CGRP significantly promoted osteogenic differentiation in both PDSCs and BMSCs while high concentrations of CGRP had an obvious chemotaxis effect on BMSCs.

**Mg increases CGRP release by affecting DRG neurons.** The results of immunochemical staining and ELISA CGRP quantification analysis of femur samples showed that femur CGRP content in Mg-implanted samples was almost twice that of controls. Previous studies reported that Mg ions could promote neural synaptic replasticity in hippocampus neurons *in vitro*. This study examined the hypothesis that Mg ions could promote synaptic replasticity in DRG neurons. The neural synaptic vesicles, which contain neuropeptides of DRG neurons, including CGRP, derived from the L3-5 dorsal root ganglion were stained *in vitro*. The synaptic vesicles were found to significantly increase in number when their medium was changed from Mg-

free medium to Mg-rich medium of 1 mM and 2 mM and to migrate from the neuron body to its axon terminals. These results proved that Mg could facilitate neuron replasticity and prompt synaptic vesicle aggregation at axon terminals, indicating that much neuropeptide release occurs after stimulation. Real-time recording of the intracellular Mg signal revealed that DRG neuron Mg influx significantly increased after Mg medium had been added and that Mg influx into neurons was mainly through the membrane Mg ion channel MagT1. Implantation of Mg ions ($MgCl_2$) of high concentration was found to promote stem cell (PDSCs and BMSCs) osteogenic differentiation. Although the mechanism of Mg's osteogenic effect on stem cells was not thoroughly studied, cellular Mg influx was found to increase in high-Mg medium through the membrane ion channel MagT1.

**Mg accelerated bone fracture in ovariectomized rats.** Mg metal is too soft to repair bone fracture in animal models. To overcome this challenge, we designed a novel intramedullary nail containing Mg to accelerate osteoporotic bone fracture healing in ovariectomized (OVX) rats. The novel nail is a hollow stainless steel needle with several interlacing arranged holes drilled midway through the needle. The Mg pin is inserted into the needle canal and Mg ions released through the holes on the needle reach the fracture line during degradation *in vivo*. Our findings indicate that use of this Mg-containing intramedullary nail could accelerate bone fracture healing in OVX rats. Review of post-surgery X-ray results showed that the fracture callus of the Mg-treated group was significantly larger than that of the control group at weeks 2 and 4. Review of micro-computed tomography (micro-CT) scanning images indicated that both the total volume and area of callus bone in the Mg-treated group exceeded those of the control group at week 4. However, no significant difference was found between the two groups regarding callus area and volume at week 12.

Histomorphological analysis showed a wider intramembranous ossification area and woven bone area in the Mg-treated group at weeks 2 and 4 and more cartilage tissue at the callus site in the Mg-treated group at week 4. Double fluorescence labeling staining revealed more densely stained newly formed bone in the Mg-treated group than the control group at week 4, indicating accelerated callus bone formation in the Mg-treated group. The callus was observed to be undergoing endochondral ossification and woven bone remodeling at weeks 8 and 12. Review of polarized light images showed brighter and more regularly arranged collagen fibers in the Mg-treated group compared to the control group. Biomechanical testing at week 12 revealed that the ultimate load of shaft bone in the Mg-treated group had increased 30% more than that of the control group. These results indicate that the novel Mg-containing intramedullary nail designed in this study could significantly accelerate and optimize osteoporotic fracture healing in OVX rat model.

**Significance:** The results of this study contribute to a thorough understanding of the osteogenic effect of Mg by explicating its bioeffect on neurons and stem cells. The novel Mg-containing intramedullary nail designed in this study appears promising in osteoporotic fracture healing and to have many potential clinical applications.

# 论文摘要

我们的研究是基于发现镁金属的成骨现象。在我们组之前的工作中，我们发现大鼠股骨骨髓腔内植入镁棒后，在很短时间内（一周后）就会在股骨骨膜下部位形成新骨。这种镁导致的成骨现象是怎样发生的，以及我们能否利用镁金属的这种特性去促进骨质疏松骨折的愈合？对这两个问题的解答便构成了本篇论文的主要内容。

因为镁诱导的新生骨产生在骨膜下方，并且植入镁棒产生的成骨现象在骨膜剥除的部位消失，所以我们认为骨膜是镁成骨的关键点。骨膜是富含感觉神经纤维和干细胞的组织，而且动物骨的感觉神经分布主要集中在骨膜（约占总的神经数量的 99%以上）。骨膜神经末端不仅仅感知痛觉触觉和温度觉，而且在外界刺激下释放感觉神经递质。神经递质包裹于处于神经末梢的囊泡当中，CGRP 是经典的也是分布最广的感觉神经递质。在动物体内，血液中 CGRP 的含量随年龄的增加而减少，同时骨内的镁含量也随之流失。这也是老年龄动物骨折愈合较慢的原因之一。所以我们提出本课题的研究假设：镁金属降解产生的镁离子作用于骨膜部位的感觉神经末梢，刺激神经递质 CGRP 的释放。骨膜内增多的 CGRP 作用于骨膜内的干细胞进行成骨分化，最后形成新骨。我们进一步检测镁的这种成骨作用能否促进骨质疏松鼠骨折的愈合。

首先我们用过量的辣椒素破坏大鼠股骨的感觉神经末端之后，镁的成骨显著减少，这说明镁的成骨作用相当程度上依赖于通过骨膜的神经组织。我们通过免疫组化染色及蛋白定量测定发现，植入镁后的骨组织内 CGRP（降钙素基因相关肽，一种感觉神经末端分泌的主要神经递质）含量增加了一倍多。我们用 CGRP 受体拮抗剂同样发现可以部分抑制镁的成骨作用。我们推测镁降解过

程中产生的镁离子在骨膜部位增加了感觉神经递质的释放，骨膜部位增多的神经递质作用于骨膜源性间充质干细胞以及骨髓源性间充质干细胞想成骨方向分化成骨。体外试验结果表明，CGRP 在高浓度下显著促进骨膜及骨髓源性干细胞的成骨分化。我们从大鼠的脊髓腰段 L3-5 背根神经节分离出背根神经节神经元，在体外用荧光对神经元内的突触小泡进行染色，发现当培养液中的镁离子浓度升高时（1-2mM），这些富含神经递质 CGRP 的突触小泡不但数目增加，而且从胞体中心向轴突末梢迁移。在这个过程中，我们同时记录到显著的镁离子内流。实验结果表明，镁离子可以促进神经元的复极化以及神经递质向轴突末端迁移聚集，从而在下一次刺激中释放出更多的神经递质。同时体外干细胞分化实验结果表明高浓度的镁离子（5-10mM）显著促进干细胞的成骨分化。对干细胞和神经元的胞内镁离子内流检测发现，在胞外镁离子浓度升高的情况下，胞内镁离子内流主要通过一种膜通道 MagT1。至此，关于镁成骨的机制可以归纳为：镁金属在降解过程中产生的镁离子作用于骨膜感觉神经末梢，使之释放出更多的神经递质，增加释放的神经递质和镁离子共同促进分布在骨膜和骨髓的干细胞进行成骨分化，从而增加成骨。

镁的成骨效应使之有很大的潜力用于骨质疏松骨折的修复。由于镁金属强度不足以直接用来固定大鼠骨折，所以我们设计了一种中空的不锈钢针管作为髓内骨折固定针。针管中部与骨折线对应的部位开出一些小孔，细的镁棒可以插入针管，在体内镁降解产生的镁离子可以从中部的小孔释放出去发挥其成骨效应，进而促进骨折的愈合。我们用卵巢切除大鼠进行闭合性骨折造模，然后用我们设计的髓内针固定。X 射线结果表明，手术后第二、四周镁治疗组骨折愈合组织的面积和宽度显著大于对照组。Micro-CT 扫描结果也同样表明，镁治

疗组骨折部位愈合组织的总体积和骨组织体积在术后第四周显著大于对照组。组织学染色表明，在术后第二周，镁治疗组的骨折部位的骨膜内成骨大量增加，并且有大量间充质细胞充塞与骨折部位。第术后第四周，更多的软骨组织形成于镁治疗组的骨折部位。荧光双染色结果也表明，镁治疗组的骨折部位在第四周有更多的新生骨形成。第八周和十二周的偏振光图像表明，镁治疗组的骨折愈合部位形成的胶原纤维比对照组更规则且更多更亮。这说明在骨折愈合后期软骨内成骨以及编制骨向层状骨转化的过程中，镁治疗组的骨重建更加规则。最后在第十二周的力学实验结果证明，镁治疗组的骨干所能承受的最大压力显著高于对照组（大约增强了 27%）。这部分体内试验证明镁金属可以加速并优化大鼠骨质疏松骨折的愈合，而且我们设计的中空含镁髓内针可以作为将来临床新型骨折髓内固定针的原型。

结论：我们对镁成骨的作用和其机制进行了比较深入全面的研究，并初步证实镁金属可以用于动物骨质疏松骨折的修复。我们的研究结果为将来镁金属在临床尤其是骨科领域的实际应用提供了一些基本的理论依据。

## Acknowledgments

I would like to express my great gratitude to my supervisor, Prof. Qin Ling, for offering me a wonderful opportunity within a highly interdisciplinary department to learn, study, and complete my dissertation. I will never forget your patience, guidance, teaching, tolerance, and broad understanding, sterling characteristics deserved to be enjoyed by all students engaged in lifelong learning. Furthermore, I would like to thank for your efforts in enabling cooperation among several groups to support my project, which significantly broadened my learning and views.

I would also like to express my gratitude to my co-supervisor, Prof. Zheng Yufeng, who first led me onto the scientific road and introduced me to the orthopaedic biomaterial field after my MPhil study. I would also like to thank him for the encouragement and strong support he gave me to finish my PhD study. Thanks again to my dear teacher Zheng.

I especially admire and appreciate Dr. Jerry Xu Jiankun, who shared with me all his experimental skills *in vivo* and *in vitro* without any reservation. Thank you for your great assistance and association with my project. You are so selfless, earnest, intelligent, and assiduous; you are one of my most important friends and greatest teachers. I sincerely hope that you achieve your great ambitions over the next decade. We will be great friends forever.

I am very grateful to Prof. Guo Xia and Dr. Wang Xiaoyun as promotors of the CGRP study.

I must send my great appreciation to Prof. Chan Hsiao Chang and Prof. Ruan Yechun, who supported my key experiments in the School of Biomedical Sciences (CUHK) and provided very valuable suggestions, especially regarding the neuron and stem cell study. This thesis is also dedicated to you both.

I would especially like to thank Ms. Priscilla, who provided me with great help during the neuron and stem study. I will remember your assistance along with many flash points in CUHK. I would also like to thank Mr. Shi Dufang and TianLi, who helped design the fracture healing needle and performed the FEA simulation, the important parts of my study.

Special thanks go to my office colleagues Mr. Michael O, Laughlin, Ms. Priscilla, and Dr. Ruan Ye Chun in SBS; Mr. Shi Dufang, Dr. Wang Xiaoyun, Mr. Wang Jiali, Mr. Tong Wenxue, Mr. Tian Li, Ms. Helen Huang, Dr. Cathey Chen, Ms. Zhen Lizhen, Dr. Dick Chow, Dr. Xie Xinhui, Dr. Eric, Ms. Maggie Cheuk; my friends Dr. Huang Shuo, Dr. Frank Wei, and Dr. Guo Anyun; and our secretary, Ms. Debbie Ho, for every shared minute of difficulty and happiness. Thanks to everyone who contributed to this work.

Finally, I am indebted to my parents and my sister for caring for so many years: I love you from the depths of my heart.

Thanks for life!

# Abbreviations

| Abbreviation | Full spelling |
|---|---|
| 2-APB | 2-aminoethyl diphenyl borinate |
| cAMP | Cyclic adenosine monophosphate |
| ALP | Alkaline phosphatase |
| ANOVA | Analysis of variance |
| ATP | Adenosine triphosphate |
| AMPA | α-amino-3-hydroxy-5-methyl-4-isoxazolepropionic acid |
| BV | Bone volume |
| BDS | Brainstem-derived serotonin |
| BMD | Bone mineral density |
| BMSC | Bone marrow-derived mesenchymal stem cell |
| BMP-2 | Bone morphogenetic protein-2 |
| BIBN | 1-[3,5-Dibromo-N-[[4-(1,4-dihydro-2-oxo-3(2H)-quinazolinyl)-1-piperidinyl]carbonyl]-D-tyrosyl-L-lysyl]-4-(4-pyridinyl)-piperazine |
| Cy5 | Indodicarbocyanine 5 |
| CCL | C-C motif chemokine |
| CD 90 | Cluster of differentiation 90 |
| Ca | Calcium |

| | |
|---|---|
| CGRP | α-calcitonin gene-related peptide |
| COL-1 | Collagen I |
| CREB | cAMP response element-binding protein |
| DAPI | 4',6-diamidino-2-phenylindole |
| DMEM | Dulbecco's modified eagle’s medium |
| DPX | p-xylene-bis-pyridinium bromide |
| DRG | Dorsal root ganglion |
| ECM | Extracellular matrix |
| FEA | Finite elemental analysis |
| FBS | Fetal bovine serum |
| GAPDH | Glyceraldehyde 3-phosphate dehydrogenase |
| GFP | Green fluorescent protein |
| HG-DMEM | High glucose Dulbecco’s Modified Eagle Medium |
| HA/TCP | Hydroxyapatite-tricalcium phosphate |
| $H_2O_2$ | Hydrogen peroxide |
| H&E | Hematoxylin and eosin |
| HRP | Horseradish peroxidase |
| HSC | Hematopoietic stem cell |
| K | Potassium |
| iPSC | Induced pluripotent stem cell |

| | |
|---|---|
| IL | Interleukin |
| IF | Immunofluorescence |
| LG-DMEM | Low glucose Dulbecco’s Modified Eagle Medium |
| ρ-MOI | Moment of inertia |
| MTT | 3-(4,5-dimethyl-2-thiazolyl)-2,5-diphenyl-2-H-tetrazolium bromide |
| Mg | Magnesium |
| MSC | Mesenchymal stem cell |
| NGF | Neural growth factor |
| NMDG | N-methyl-D-glucamin |
| NMDAR | N-methyl-D-aspartate receptor |
| NO | Nitric oxide |
| NaCl | Sodium chloride |
| OPG | Osteoprotegerin |
| OPN | Osteopontin |
| OCN | Osteocalcin |
| OVX | Ovariectomized |
| PBS | Phosphate-buffered saline |
| PDSC | Periosteum-derived stem cell |
| PGE | Prostaglandin E |
| PTH | Parathyroid hormone |

| | |
|---|---|
| qRT-PCR | Quantitative real-time reverse transcription-polymerase chain reaction |
| REA | Repressor of estrogen receptor activity |
| RANK | Receptor activator of nuclear factor kappa-B |
| RANKL | Receptor activator of nuclear factor kappa-B ligand |
| RUNX2 | Runt-related transcription factor 2 |
| SCI | Spinal cord injury |
| SD | Standard deviation |
| Sox9 | Transcriptional factor, SRY-box 9 |
| SDF-1 | Stromal cell-derived factor-1 |
| TBS | Theta-burst stimulation |
| TH | Tyrosine hydroxylase |
| TDSC | Tendon-derived stem cell |
| TGF-β1 | Transforming growth factor beta 1 |
| TRPM6/7 | Transient receptor potential melastatin 6/7 |
| TRPV1 | Transient receptor potential cation channel 1 |
| TRAP | Tartrate-resistant acid phosphatase |
| TV | Total bone volume |
| VEGF | Vascular endothelial growth factor |
| VIP | Vasoactive intestinal peptide |
| XRD | X-ray diffraction |

# Table of Contents


Declaration ..... 3
Abstract ..... 1
论文摘要 ..... 5
Abbreviations ..... 10
Chapter 1 ..... 16
*1.1 History of Mg and its alloys as biomaterials in orthopaedics* ..... 17
*1.2 Role of Mg in the biomineralization process* ..... 22
*1.3 Mg and bone metabolism* ..... 28
*1.4 Role of bone innervation and neuropeptides in osteogenesis* ..... 33
*1.5 Osteoporosis and fracture repair* ..... 39
*1.6 Hypotheses and objectives* ..... 47
Chapter 2 ..... 49
2.1 Introduction ..... 50
2.2 Materials and Methods ..... 52
2.2.1 Intramedullarily implanted Mg pin into the rat femur ..... 52
2.2.2 Periosteum stripping ..... 53
2.2.3 Capsaicin administration ..... 54
2.2.4 CGRP receptor antagonist BIBN4096bs administration ..... 55
2.2.5 Imaging and histology ..... 59
2.3 Results ..... 63
2.3.1 The periosteum is critical in Mg-induced new bone formation ..... 63
2.3.2 Neuropeptide CGRP is pivotal in Mg-induced new bone formation ..... 65
2.4 Discussion ..... 73
Chapter 3 ..... 78
3.1 Introduction ..... 79
3.2 Materials & Methods ..... 80
3.2.1 Isolation and culture of rat PDSCs and BMSCs ..... 80
3.2.2 Fluorescence staining for the stem cell markers ..... 81
3.2.3 Cell Proliferation Assay ..... 82
3.2.4 Cell migration assay ..... 82
3.2.5 qRT-PCR assay for osteogenic markers ..... 83
3.2.6 Alizarin red and ALP staining assay ..... 85
3.2.7 Colony forming and osteogenic differentiating ability of PDSCs at passage 1 ..... 86

3.2.8 qRT-PCR assay for adipogenic markers....86
3.3 Result....88
3.3.1 PDSCs were critical in periosteal osteogenesis....88
3.3.2 Effects of CGRP on MSCs' proliferation, migration, and differentiation....88
3.3.3 Effect of Mg ions on MSCs' proliferation, migration and differentiation....89
3.4 Discussion....100
Chapter 4....106
4.1 Introduction....107
4.2 Materials & Methods....109
4.2.1 DRG neuron isolation and culture....109
4.2.2 Synaptic replasticity under Mg treatment....110
4.2.3 Cell Mg influx detection....112
4.3 Results....115
4.3.1 Mg ions promoted synaptic replasticity in DRG neurons....115
4.3.2 Mg entered neuron through channel MagT1....115
4.3.3 Mg influx in MSCs under different pH circumstances....116
4.4 Discussion....123
Chapter 5....128
5.1 Introduction....129
5.2 Materials & Methods....131
5.2.1 Intramedullary nail designing....131
5.2.2 Experimental design of fracture healing....134
5.2.3 Radiography and histomorphometry analysis....138
5.3 Results....142
5.3.1 Design of intramedullary nail....142
5.3.2. Mg accelerated fracture healing in OVX rats....144
5.4 Discussion....158
Chapter 6....164
6.1 General Conclusion....165
6.2 Limitations of the Study....165
6.3 Future studies....166
Funding Acknowledgement....168
References....170
Appendix....181

# Chapter 1

# General Introduction

This chapter outlines the history of magnesium (Mg) as an attracting orthopaedic biomaterial, bodily Mg content in bone metabolism, scientific exploration of the function of Mg coupled with Calcium (Ca) in biomineralization, bone and periosteum innervation, cell membrane Mg ion channels, and osteoporotic bone fracture repair. This mini review provides a basic background of the study.

### ***1.1 History of Mg and its alloys as biomaterials in orthopaedics***

Many years ago, the preferred weight-bearing biomaterials developed for orthopaedic applications were stainless steel, titanium, and cobalt-chromium based alloys. These materials provided strong and stable mechanical strength, durability, and wear resistance. Metallic properties were known to be superior to ceramic and polymer properties, making metallic biomaterials the most popular-used orthopaedic implants in routine clinical treatment[1,2]. However, metal was known to be naturally prone to cause stress shielding to bone, and an elastic moduli mismatch between metal implants (Young's modulus 100–200 GPa) and adjacent cancellous bone (Young's modulus 10–30 GPa) had been identified. The stress-shielding effect along with the accumulation of toxic metallic ions and wear debris at the implant–bone interface was found to adversely affect new bone formation and remodeling at the implant–bone interface[2-9]. Another issue was that in the obligatory secondary surgery, non-degradable metallic implants foreign bodies were carrying in a long term. The metal plates, screws, and pins used in bone fracture fixation were removed after tissue had sufficiently healed, and the repeated surgery increased costs and morbidity[2,10].

Great effort has been made in identifying new biomaterials possessing the characteristics of biocompatibility, bioactivity, and biodegradability. Mg and its alloys are considered prospective materials in future orthopaedic applications in virtue of

their highly cancellous bone-similar elastic moduli (Young's modulus 40–50 GPa), biodegradability, and biocompatibility (T**able 1**[2]).

**Summary of the physical and mechanical properties of various implant materials and natural bone**[2]

| Property | Natural bone | Mg | Ti alloy | Co–Cr alloy | Stainless steel | Synthetic HAP* |
|---|---|---|---|---|---|---|
| Density ($g/cm^3$) | 1.8–2.1 | 1.74–2.0 | 4.4–4.5 | 8.3–9.2 | 7.9–8.1 | 3.1 |
| Elastic modulus (Gpa) | 3–20 | 41–45 | 110–117 | 230 | 189–205 | 73–117 |
| Compressive yield strength (Mpa) | 130–180 | 65–100 | 758–1117 | 450–1000 | 170–310 | 600 |
| Fracture toughness ($MPa.m^{1/2}$) | 3–6 | 15–40 | 55–115 | N/A | 50–200 | 0.7 |

*HAP: Hydroxyapatite

Mg and its alloys were developed for more than one century after the commercial production of Mg became reality in 1852[11]. After the first clinical application of metallic Mg as a ligature to stop vessel bleeding by Huse in 1878, Mg was broadly used in the cardiovascular, general surgery, and musculoskeletal fields in the early 20th century[11]. On one hand, Mg's rapid biodegradation made it not the best candidate for use in fixator pins, nails, wires (cerclage), pegs, cramps, Mg sheets, or plates used for orthopaedic applications. On the other hand, the advantages provided by Mg's rapid biodegradation brought great inspiration and hope to researchers and clinicians for a long period[11-19]. However, its rapid corrosion rate still hampered Mg's application to orthopedic usages, especially due to its decreased mechanical sustainability before bone fracture healing.

Determining how to control the rapid corrosion rate of Mg *in vivo* was an important step in its use in clinical fields. Among the several effective processing methods for

controlling the rapid degradation of Mg are purification, alloying, surface coating, and anodization[13,15].

**Purification and alloying:** Studies have proved that the purification of Mg considerably affects its rate of corrosion, with less purity leading to a faster rate of corrosion[7]. As the application of pure Mg to orthopaedics and other load-bearing functions is restricted due to its low yield strength, elements such as calcium (Ca), zinc (Zn), strontium (Sr), silicon (Si), manganese (Mn), copper (Cu), tin (Sn), and aluminum (Al), considered the most effective elements in enhancing Mg's strength and corrosion resistance (Figure 1)[18,20], have been added to Mg applications. Ca and Zn, both essential elements in the human body that provide for basic safety in biomedical applications[15,20], act as grain-refining agents to improve both corrosion resistance and mechanical properties. Ca has also been reported to improve the corrosion resistance of Mg-based alloys in simulated body fluid. With increasing Ca content, more and coarser $Mg_2Ca$ phase precipitates are distributed along grain boundaries, enhancing both the corrosion resistance and mechanical properties of Mg–Ca alloys[2,14,15]. Meanwhile, the addition of Zn increases the strength of Mg-based alloys, primarily due to precipitation strengthening.

Of the approximately 140 mg of Sr, which shares metallurgical, chemical, and biological properties with Ca and Mg, in the human body, 99% is contained in bone tissue. Proper addition of Sr (Mg-2Sr), which exhibits the highest strength and the lowest corrosion rate of all Mg alloys[21,22], can refine the grain size of Mg alloys. Of the trace elements Si and Mn, Si plays an important role in the development of bone and connective tissue, aiding the healing process and helping build the immune system. While Mn helps overcome the harmful corrosive effect of iron (Fe) and nickel (Ni) impurities that might be present in Mg alloys, high concentrations of Mn may

induce neurotoxicity[18].

Al was once a major alloying element in Mg-based alloys, but its poor biocompatibility was found to cause phosphate depletion in tissues and lower phosphate absorption from the digestive tract[15]. Other alloying elements, such as cadmium (Cd), tin (Sn), iron (Fe), nickel (Ni), copper (Cu), and cobalt (Co), as well as rare earth elements such as cerium (Ce), lutetium (Lu), and praseodymium (Pr), are deleterious to the corrosive properties of Mg and generally considered toxic to the human body[15]. In short, refinement of Mg microstructure by Ca and Zn has proven an effective way to improve the mechanical and corrosion properties of Mg alloys, leading to the development of new Mg-Zn-Ca alloys for potential use as biodegradable and bioabsorbable implant materials[20,23-25].

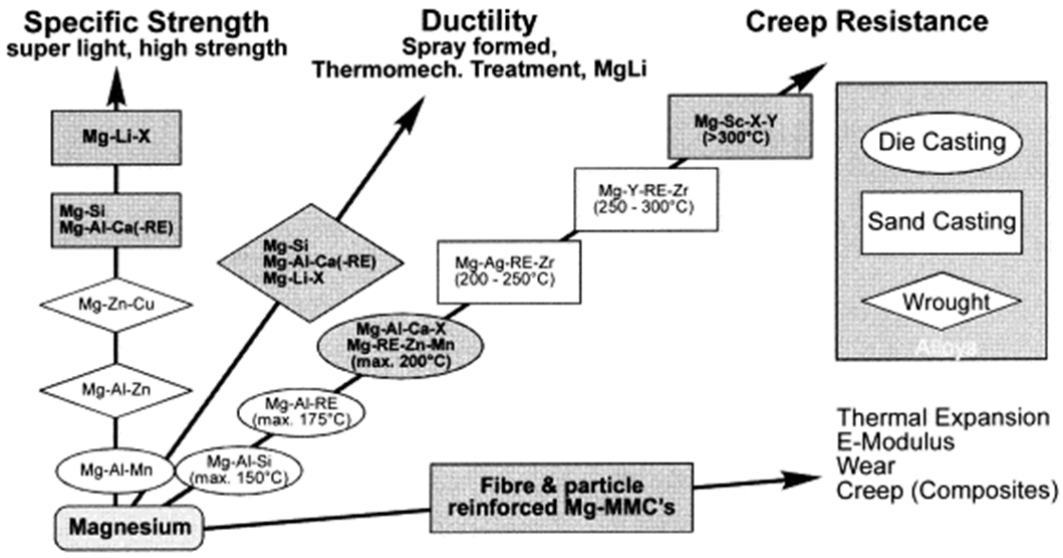


Figure 1. Process of alloy development[18]

**Coating and anodization process:** In the coating and anodization of Mg and its alloys, hydroxyapatite (HA) and other types of calcium phosphate (Ca-P) materials have generally been of high interest. This interest is due to their excellent biocompatibility and bioactivity, which are attributed to their structural and chemical

similarities to bone minerals[19]. Although use of chemical methods is the proper way to prepare HA coating on Mg substrates, direct synthesis of HA on Mg alloys was a scientific challenge because Mg ions prevent HA crystallization with the substitution of Mg atoms. Microarc oxidation (MAO) followed by electrochemical deposition (ED) of HA has been recognized as a very promising technique for developing degradable Mg alloys coating due to its capacity to overcome single HA coating on a porous substrate or one with a complex shape, relatively higher bonding strength, controllability with regard to the thickness and chemical composition of the coating, and low deposition temperature. Anodization can be used to fabricate nanostructure coatings with desirable corrosive-protective, decorative, and functional properties while increasing film thickness, hardness, corrosion resistance, and wearing resistance and providing better adhesion for Mg metal and its alloys. Many studies have reported that a variety of self-ordering electrochemical processes can be used to produce oxide nanostructures from aqueous or nonaqueous fluoride-containing solutions[7,19,26,27]. Despite research indicating that Mg and its alloys are suitable biomaterials in orthopaedics, no mature Mg-based materials are yet being used clinically.

Besides observing its specific metallic properties, our group recently observed that Mg promoted new bone formation in the subperiosteal region when an Mg intramedullary pin was implanted into a rat femur, a phenomenon first reported by Witte six years ago[28]. Even 90 years ago, Lambotte and McBride both observed periosteal proliferation progress and marked stimulation of periosteal bone formation using pure Mg (99.7%) and Mg-Al-Mn alloy screw and nail transfixion in humans, rabbits, and dogs who had sustained bone fracture[11]. This newly noticed characteristic of Mg shed new light on Mg's osteosynthetic applications in bone fracture repair. This thesis aims to provide additional insight based on observation of Mg's bone-

promoting effects in the rat femur.

### ***1.2 Role of Mg in the biomineralization process***

The architecture of biominerals endows these organic–inorganic composites with superior strength and toughness, allowing them to outperform many other synthetic materials. Their superior material properties have been attributed to their composition, specifically of organic–inorganic hybrid building bricks precisely arranged over several nanometers. However, the process of biomineralization has long remained a mystery in biology evolutional history[29]. Debate has persisted for several decades despite application of high-resolution microscopy yielding more and clearer images revealing the characteristics of the inner side of the complex structure in biominerals, such as bone tissue. The classical "deck of cards" view proposed that the biomineralization process was ignited by a small soluble Ca-P molecule that migrated and attached to the collagen frame and mineralized to HAP in the gaps and cavities between intrafibrillar crosslinking collagens[30]. In the debate that began in the 1960s, many researchers argued that amorphous calcium phosphate (ACP) precursors that might be undetectable by conventional analytical techniques could be used in fibrillar biomineralization[31-34].

**Hierarchical levels of bone**

With the aid of scanning electron microscopy (SEM) and transmission electron microscopy (TEM), Weiner and Wagner[35] described osteon bone as composed of several hierarchical levels from basic components, including mineralized collagen fibrils, fibril arrays, fibril array patterns, cylindrical motifs (osteons), and spongy or compact bone to whole bone. The starting basic components are nanoscopic platelets of HAP oriented within self-assembled collagen fibrils. The structure of type I

collagen, which took many years to identify, is composed of repeating amino acid residues consisting of –(Gly-X-Y-)n– assembled into a triple helical structure referred to as tropocollagen. The collagen fibrils bend in a tube-like fashion and have regular array of gaps 40 nm wide[36]. Individual small (length 25–50 nm, width 15–30 nm, and thickness 2–10 nm) and "poorly crystalline" (4–6% carbonate, 0.9% Na, and 0.5% Mg impurity, with a Ca:P ratio less than 1.67) HAP crystals have been found in deproteinated bone[34,37,38]. It is important to realize that the crystals outgrew the dimension of the gap zones in the fibrils, leading to consideration of how HA crystals could have formed and embedded into the intrafibrillar collagen gaps. It could not be explained by HAP mineralization firstly and embedding secondly, because precise proposition of oversize crystalline would be a puzzling question. Pre-mineralized Ca-P clusters should first aggregate into the intrafibrillar gap before mineralization occurs. However, consideration of this process leads to consideration of how Ca-P clusters directionally migrate or are attracted to the collagen fiber site.

Gebauer and Pouget showed that close to the mineralization site at the collagen fibril, a stable pre-nucleation cluster based on calcium biominerals couples with non-collagen proteins (NCPs) aggregated into an amorphous precursor phase, and subsequently transforms into a crystal[39]. Nudelman[40] *et al* subsequently reported that polyaspartic acid, a soluble negatively charged nucleation inhibitor, stabilizes and formulates amorphous calcium phosphate (ACP) into a loose and highly mobile structure *in vitro*. This process leads to the deposition of a dense network of pre-nucleation clusters bound with nanosized and positively charged amino residues located inside the gap and overlapping zones in the collagen fibrils. This network is then transformed into ACP and, finally, oriented crystalline hydroxyapatite[34,41]. Mahamid and Beniash *et al.* recently observed enormous ACP phases in zebrafish fin

bones and tooth enamel, which are characterized by a fast bone-forming process[42]. Their observation effectively supports a concept contrasting with the classic view of crystallization in bone biomineralization.

**Different chemicals constituted by Ca/P**

In rudimentary ACPs, the main mineral constituents are calcium orthophosphates consisting of the major elements of Ca, P, O, and H. According to the Ca/P molar ratio, several kinds of calcium orthophosphates exist in nature (T**able 2**). [43]

**Table 2 Ca/P Molar Ratios and Chemical Formulas and the Solubility[a] of Calcium Orthophosphate Minerals[43]**

| Ca/P molar ratio | Compound | Formula | Solubility 25 °C, −log(Ksp) | Solubility 37 °C, −log(Ksp) | Solubility product 37 °C |
|---|---|---|---|---|---|
| 1.00 | Brushite (DCPD) | $CaHPO_4 \cdot 2H_2O$ | 6.59 | 6.73 | $1.87 \times 10^{-7}$ $M^2$ |
| 1.00 | Monetite (DCPA) | $CaHPO_4$ | 6.90 | 6.04 | $9.2 \times 10^{-7}$ $M^2$ |
| 1.33 | Octacalcium phosphate (OCP) | $Ca_8(HPO_4)_2(PO_4)_4 \cdot 5H_2O$ | 96.6 | 98.6 | $2.5 \times 10^{-99}$ $M^{16}$ |
| 1.20–2.20 | Amorphous calcium phosphate (ACP) | $Ca_xH_y(PO_4)_z \cdot n$ $H_2O$, $n$ =3–4.5; 15–20% $H_2O$ | ~ | ~ | |
| 1.50 | α-tricalcium phosphate (α-TCP) | α-$Ca_3(PO_4)_2$ | 25.5 | 28.5 | $2.8 \times 10^{-29}$ $M^5$ |
| 1.50 | *β*-tricalcium phosphate (*β*-TCP) | *β*-$Ca_3(PO_4)_2$ | 28.9 | 29.6 | $2.5 \times 10^{-30}$ $M^5$ |
| 1.67 | Hydroxyapatite (HAP) | $Ca_{10}(PO_4)_6(OH)_2$ | 116.8 | 117.2 | $5.5 \times 10^{-118}$ $M^{18}$ |
| 1.67 | Fluorapatite (FAP) | $Ca_{10}(PO_4)_6F_2$ | 120.0 | 122.3 | $5.0 \times 10^{-123}$ $M^{18}$ |

[a]The solubility is given as the logarithm of the ion product of the given formulas

(excluding hydrate water) with concentrations in mol/L (M). (~ Cannot be measured precisely)

HAP has been found to have the least soluble phase and most thermodynamic state among all Ca-P phases. Dicalcium phosphate anhydrous (DCPA) and octacalcium phosphate (OCP) are considered precursors in forming apatite, but have been rarely observed during *in vivo* crystallization. As ACP is an unstable phase in the thermodynamic state, several stabilizers should be added to keep ACP precursors stable in the transporting process into collagen fibril gaps. It has been reported that some peptides, such as alkaline phosphatase (ALP), osteocalcin (OC), and bone sialoprotein (BSP), and small chemical molecules, such as free citrate and carbonate anions and alkaline ions such as $Na^{+}$, $Zn^{2+}$ and $Mg^{2+}$, are all able to inhibit spontaneous $CaO_x$ crystallization and regulate crystal growth in calcium phosphates[41,43].

**Mg in bone mineralization**

It has been found that 60% of bodily Mg content is in bone and exists mainly as the surface substituent of the hydroxyapatite mineral component in forms of $MgCO_3$. Researchers have explored the role of the Mg ion in biomineralization for decades. In a study analyzing the tibia/fibula mineral content of normal S/D rats, James found that the mineral content increased between 4 and 22 weeks of age, while the ratio of Mg/Ca progressively declined from 0.035 to 0.027 and the $CO_3/PO_4$ rate progressively increased from 0.105 to 0.16[44]. These findings indicate that Mg may play a pivotally active role in the bone mineralization progression. In 1984, Nancollas found that Mg ions appreciably retarded the OCP growth rate and strongly inhibit thermodynamically stable HAP crystallization[45,46]. They further proved that Mg ions

at concentrations ranging from 0.0099 to 0.99 mM reduce the HAP growth rate by 51% and 93%. After finding that Mg's inhibitory effect is enhanced by synergization with $CO_3$ anions, Cao proposed that Mg ions induce a significant inhibitory effect on the larger crystal growth of HAP by forming a surface complex at the active growth site of newly formed small HAP crystals and bonding to small crystals to prevent unceasing precipitation of Ca-P[45,46]. It has been suggested that $Mg^{2+}$ kinetically hinders nucleation and subsequent growth of HAP by competing for structural sites with chemically similar but larger $Ca^{2+}$.[47,48]

Carried out mostly by chemists and environmental scientists, these studies' initial purpose was finding an effective way to remove phosphorus from wastewater to avoid eutrophication and reuse the precipitated phosphorus in agriculture. However, biologists and medical scientists noted that this procession occurs in mineral crystal formation, which has great significance in understanding the mechanical property of bone in physiological situations and the non-bone-tissue calcification germinated in arterial and renal systems under pathological conditions[45-47,49].

The many detailed investigations of the mineral phase or crystal size (range 10–40 nm in normal bone), which have contributed to understanding of bone mechanics in medical science, repeatedly demonstrated that while mineralization yields normal bone tissue stiffness and strength, excessive mineralization leads to poor bone ductility[44,50-52].

**Mg loss in aging animals**

In a study of the anterior, medial, lateral, and posterior quadrants of cadaveric femurs in 16 people aged 52 to 85 years[52], Yerramshetty found that in two types of bone tissue with similar mineral weight content, bone with smaller or shorter crystal length had greater deformability and failure-strain resistant ability than bone with larger or

longer crystal length. Many studies have also observed that the mechanically strong bones of younger animals have a mixture of larger mature and smaller crystals, while osteoporotic bones or those of older animals contain more mature and larger crystals. Boskey hypothesized that bone mineral crystal size and perfection affect bone's ability to respond to load and that bone with a greater number of larger crystals than optimal would have reduced resistance to load, i.e., would be more brittle [50] (**Table 3**).[50]

**Table 3. Crystal size variation and compromised bone mechanical properties[50]**

| Animal model | Crystal size alteration relative to control | Mechanical property | Method of crystal size analysis |
|---|---|---|---|
| Ovariectomized monkeys and mice | Larger | Increased fragility | XRD, IR |
| Human and mouse osteogenesis imperfecta | Smaller intrafibrillar, larger extrafibrillar | Brittle (absorb little energy before failure) | XRD, TEM, IR |
| Hypophosphatemic mice | Smaller | Weak and ductile | XRD |
| Rachitic rats and chicks | Larger | Weak and ductile | XRD |
| Sr-osteomalacia (rat) | Smaller | ? | XRD |
| Ia/ia osteopetrotic rat | Smaller | Stiff and brittle | XRD |
| Osteopontin-null mice | Larger | Increased whole bone strength | FTIRM and FTIRI |
| Osteonectin-null mice | Larger | Reduced stiffness/increased brittleness | FTIRM and FTIRI |
| Osteocalcin-null mice | Smaller | Increased whole bone strength | FTIRM |

Evidence supports Boskey's observation of bone with increased crystal size and reduced bone mechanical properties in ovariectomized (OVX) monkeys, osteonectin-null mice, osteopontin-null mice, and Mg-deficient rats. These findings indicate that crystal properties, including mineral composition, particle size, and distribution,

should be considered important factors in bone properties and fracture resistance, because mineral crystal optimization is a crucial step in osteoporosis therapy.

Undoubtedly, Mg plays an important role in bone mineralization. Indeed, dietary Mg deficiency has been found to be correlated with osteoporosis in both animals and humans[50]. While the research findings to date indicate that Mg applications are low cost and highly efficacious candidates in the treatment of senile bone fracture, many considerations remain. These include identification of the concentration range of Mg ions that has the best effect on bone tissue mineralization, especially in enhancing bone strength and ductility in older people and people with osteoporosis, and how to apply Mg findings in the lab to clinical applications for osteoporosis prevention and therapy.

### ***1.3 Mg and bone metabolism***

Mg is the eighth most common element in the Earth's crust and the fourth most abundant cation in the body. It plays an important role in plants and animals as a central ion of chlorophyll and is the second most common intracellular cation after potassium, making it vital for numerous physiological functions[53,54]. As Mg is a critical element in maintaining body metabolism, imbalance of bodily Mg status might result in cardiovascular, neuromuscular, and nervous disorders, and even pathological bone disorders[55].

**Mg resorption**

Dietary Mg is mainly absorbed in the colon and cecum through the epithelial cell junctions and reabsorbed in the renal Henle loop epithelial cells, while excess Mg is secreted out the kidneys and intestine by urine and feces, respectively[56-58]. There are two transport systems in the Mg-absorption process: an electrochemical gradient-driven passive paracellular channel (the primary way of absorbing Mg through the gut

and kidneys in animals) and a transient receptor-potential channel melastatin member channel (TRPM6/7) regulated by the cell membrane-crossing transporter, which plays a small role but is vital for body Mg regulation through the kidneys[55]. The kidneys play a crucial role in Mg homeostasis by controlling its secretion and reabsorption. It is noteworthy that different from that of most other ions, the major reabsorption site of Mg transport is not the proximal tubule but rather the thick ascending limb of the loop of Henle. Sixty to seventy percent of Mg that flows through the glomeruli is reabsorbed at the Henle loop, while approximately 10% is reabsorbed in the distal convoluted tubules (DCTs)[54,59,60]. While Mg reabsorption mainly depends on Mg plasma levels, hormones, including parathyroid hormone, anti-diuretic hormone, glucagon, and calcitonin but not estrogen, play only a minor role[61].

To examine impaired renal and/or intestinal $Mg^{2+}$ resorption, the genes of patients with hypomagnesemia with secondary hypocalcemia (HSH) were studied using a positional candidate gene approach. It was found that they had mutations in CHAK2 encoding TRPM6 that had previously been mapped to chromosome 9q22[61,62]. When, based on this finding, several groups analyzed TRPM6/7's role in renal and intestinal $Mg^{2+}$ homeostasis, they confirmed that TRPM6 and its closest homologue TRPM7 are closely and functionally related. Studies in mice showed that TRPM7 is distributed ubiquitously, whereas TRPM6 is predominantly expressed in the kidneys, lungs, cecum, and colon, which are the main sites of active $Mg^{2+}$ (re)absorption[63].

Hoenderop *et al.*[64] showed that TRPM6 is specifically localized along the apical membrane of the renal distal convoluted tubule and the brush-border membrane of the small intestine; that TRPM6 is permeable to both $Mg^{2+}$ and $Ca^{2+}$, although the TRPM6 channel has a 5-fold higher affinity for $Mg^{2+}$ than for $Ca^{2+}$[62]; that the renal TRPM6 mRNA level is significantly reduced in OVX rats; and that 17-estradiol

treatment but not 1,25-dihydroxyvitamin D3 or parathyroid hormone could normalize TRPM6 mRNA levels[65]. Hoenderop *et al.* also identified repressor of estrogen receptor activity (REA) as an interacting protein of TRPM6 that binds to the 6th, 7th, and 8th β-sheets in its α-kinase domain and that REA is co-expressed with TRPM6 in DCT and significantly inhibits the activity of TRPM6 rather than TRPM7. They further observed that the TRPM6-mediated current in HEK293 cells is significantly enhanced under 17-estradiol treatment *in vitro*[62,65,66], while the dynamic interaction between REA and TRPM6 could be dissociated by short-term 17-estradiol treatment. These studies opened a new direction in which to explore the mechanism of osteoporosis and its treatment.

**Mg storage in bone**

Through circulation, 50–60% of Mg is reserved in the bone, 20% in the muscle, and 20% in the soft tissue, while only 1% is distributed in extracellular fluids[67]. Thus, bone provides a large exchangeable pool for whole body Mg consumption through buffering serum Mg concentration fluctuation. The total Mg content of the human body has been reported to be ~20mM/kg of fat-free tissue, meaning that a 70 kg adult with 20% fat tissue would have approximately 24 g of Mg, and thus about approximately 40-fold more Ca than Mg[68]. The physiological serum Mg concentration ranges from 0.65–1.2mM, with a normal serum Ca concentration ranging from 2.2–2.6mM. Total serum level and erythrocyte Mg level can be measured to monitor changes in Mg status, although these values do not necessarily reflect total body Mg content[56,69]. Alfrey found that 30% of bone Mg is in a surface limited pool, either within the hydration shell or the bone mineral crystal surface[70], while 70% forms an integral part of the bone crystal and is associated with the bone matrix. Both Mg pools are decreased in chronic hypomagnesaemia and renal

transplantation patients, who are associated with decreased serum Mg[70]. *In vitro* studies suggest that rapid changes in surface Mg reflect changes in serum Mg level[68], indicating that the serum Mg level is the major factor determining Mg content in bone. Overall, one third of skeletal Mg is exchangeable, serving as a reservoir for maintaining physiological extracellular Mg level. Mg deficiency due to lack of dietary Mg and/or renal failure leads to direct mobilization of bone Mg in the circulation to meet the Mg demand of other organs. If cases of low Mg intake (below 300–400 mg/d) for a long period, Mg deficiency will affect only bone but also the nerve system, cardiovascular system, muscles, endocrine glands, and other systems and organs, producing pathological symptoms such as hypertension, cardiac arrhythmia, myocardial infarction, hypokalemia, and hypocalcemia.

**Mg in cell and bone metabolism**

In the cell, Mg primarily fulfills various intracellular physiological functions as a cofactor of DNA, RNA, ATP, and almost all enzymes[71,72]. Mg has two general types of interaction with an enzyme: (i) binding to an enzyme substrate in the reaction of kinases with Mg $ATP^{2-}$(Mg-ATP), thereby forming a complex with the enzyme, and (ii) binding directly to the enzyme, thereby altering its structure and/or serving as a catalytic player (e.g., in exonuclease, topoisomerase, and RNA and DNA polymerases). Overall, the predominant action of Mg is related to ATP utilization, and thus it exists in all cells primarily as Mg-ATP[72]. Through interaction with universally required ATP, Mg metabolism also influences glucose utilization, fat and protein synthesis, methyl group transfer, nucleic acid and coenzyme activity, muscle contraction, normal neurological functions, release of neurotransmitters, regulation of vascular tone and heart rhythm, platelet-activated thrombosis, bone formation, and many other processes[73]. Mg is also reported to be an important modulator in cell

adhesion and migration, and even stem-cell differentiation[74]. Further, Mg has long been suspected of affecting insulin secretion and sensitivity in Mg-deficient animals. Recent epidemiological studies suggest that Mg deficiency at a relatively early gestational age negatively affects the mother and fetus[75-79]. As a natural Ca antagonist for the same binding site on the plasma molecule, Mg acts as an anti-apoptotic factor to relieve Ca overload-triggered apoptosis in mitochondrial permeability transition.

Mg deficiency always affects bone metabolism initially and severely. Epidemiological studies have built a small but sufficient evidence base of the correlation between osteoporosis and Mg deficiency in bone and serum[80-83]. The existence of a link between dietary Mg intake and bone mass appears to be an exception when women are in the early postmenopausal period, during which the effect of acute sex steroid deficiency may mask the effect of dietary factors such as Mg deficiency[83]. Estrogen deficiency also could provoke Mg absorption in the intestine and at the renal site. In addition, diets deficient in Mg are usually lacking in other nutrients, especially Ca. Further investigations are needed to precisely identify the correlation between dietary Mg inadequacy and osteoporosis. Although a recent study of TRPM7 knock-out mice indicated that reduced dietary Mg could lead to osteoporosis, more experiments and evidence are needed to support this finding[84].

It remains unclear how Mg promotes osteo-anabolic activity and why Mg loss in bone leads to osteoporosis in aged humans and animals. Bone remodeling markers such as serum OC, ALP, urine deoxypyridinoline, and N-telopeptide have been evaluated for prediction of bone loss in low Mg-intake conditions[83]. In one case, Mg intake was found to be negatively correlated with urinary excretion of pyridinoline and deoxypyridinoline despite not being associated with serum OC level. This finding suggests that a low-Mg diet is associated with increased bone resorption. Moreover,

decreasing osteoblast number and function plus increasing osteoclast recruitment and activity were observed *in vivo* with Mg deficiency. The effect of Mg level on serum PTH level, 1,25-$(OH)_2$-vitamin D level, and Ca content in hypomagnesemic patients is considered a critical mechanism in Mg-deficiency-caused osteoporosis[85-87]. As discussed in the previous chapter, low Mg-containing bone matrix forms larger HAP crystals and leads to bone fragility and low intensity.

Limited basic scientific and clinical data are available regarding the long-term effects of low Mg dietary intake on bone mass and constitution in human body. Fundamental considerations are how Mg level influences bone mass, bone turnover, bone-related hormones, and cytokine levels; the Mg intake level required to maintain skeletal health; and the correlation between deficiency of Mg and that of other common nutrients, including Ca and vitamin D. In addition, the differentiation of bone marrow-derived mesenchymal stem cells (BMSCs) and periosteum-derived stem cells (PDSCs) under Mg treatment should be well investigated.

Elucidating the effect of low Mg intake on the development of osteoporosis has increased as the risk of osteoporotic fractures continues to increase with an aging population, contributing to greater health care costs[88]. Exploration of the mechanism underlying decreased serum and erythrocyte Mg concentration and Mg malabsorption with aging should also be conducted.

### ***1.4 Role of bone innervation and neuropeptides in osteogenesis***

As early as 1545, the French anatomist Charles Estainne drew nerve fibers and innervated bone using a wood-cut panel. In 1925, De Castro showed that a single sympathetic nerve fiber was wrapped with capillaries at the growth line and made channels to bone along with blood vessels that branched to form several rings around

bone cells[89,90]. The innervation of bone from a humanistic view by realistic detection using available immuno-histochemical and microscopic methods persisted for almost four centuries. In a landmark report published in the *Journal of Bone and Joint Surgery* in 1966 and subsequently in *Science* in 1968, Cooper reported that cortical bone appears densely innervated under electron microscopy[91,92]. After immunochemical staining had been developed, Hohmann *et al.* observed sympathetic fibers containing vasoactive intestinal peptide (VIP) in bone in 1986[93]. To date, bone's innervation from the central to peripheral system has received great attention, leading to investigation of bone metabolism and the means of treating bone pathological lesions and pain in fracture, inflammation, and tumors.

**Nerve fibers in bone**

The peripheral nerve fibers innervated into bone are mainly classified as sympathetic and sensory nerves, both of which are peptidergic nerves, although glutamatergic innervation has also been detected in bone[94]. In a study of mineralized bone and bone marrow to examine sympathetic and sensory innervation of normal mouse femur periosteum, Mach found that the periosteum is the most densely innervated tissue per area. However, regarding the total volume of nerve fiber content, bone marrow has the greatest total number of sympathetic and sensory nerve fibers, followed by mineralized bone and then the periosteum[94]. Nerve fibers circulate throughout the periosteum and are accompanied by nutrient vessels in the Haversian and Volkmann's canals. Dense nerve fibers are proximate to more metabolically active parts of bone, such as those in the osteochondral junction of the epiphyseal growth plate and in the metaphysis in long bone[92,95]. Among these nerve fibers, peptidergic myelinated and thin/unmyelinated nerves, including A-β-, A-δ-, and C-type fibers, are all present, but not non-peptidergic unmyelinated fibers. The relative density of sensory nerve fibers

per unit volume is greatest in the periosteum, followed by bone marrow, mineralized bone, and cartilage, with the respective relative densities being 100:2:0.1:0[94]. Although peripheral sympathetic and sensory nerve fibers of bone are believed to have both afferent and efferent functions, they have distinct neurotransmitter release mechanisms and different roles in bone remodeling.

**Neuropeptides and bone metabolism**

Neural synapse communication provides direct cell-to-cell communication in most nerve-to-nerve signal transmissions and in many nerve-to-end organ transmissions. Nonetheless, this communication ultimately depends on receptor–ligand interactions, as do paracrine, autocrine, and hormonal endocrine functions[92]. To date, no classical synapse–cell connection has been found to be involved in nerve endings in osteoblasts, osteoclasts, or osteocytes. However, nerve fibers with active expression of various neurotransmitters have been observed to be in close spatial association with bone cells. Furthermore, the receptors of almost all of these neural ligands are expressed in bone cells, and thereby potential affect bone metabolism[96]. In general, neural transmitters of bone nerve endings include catecholamines, glutamate, dopamine, serotonin, and a number of small polypeptides formed by alternative RNA splicing from larger genes[92,97,98]. Table 4 shows the classification of all known neuropeptides found in bone tissue by their neural sources and individual characteristics.

**Table 4 Neuropeptides in bone**[92,95-105]

| Neurotransmitter(s) | Nerve attribution | Receptors on bone cells | Putative intermediary mechanism | Putative action |
|---|---|---|---|---|
| Endocannabinoids | Sensory nerve | CB1 and CB2 receptors | G-protein-coupled | Bone formation |
| Calcitonin gene-related peptide | Sensory nerve | CGRP-R1, CGRP-R2 | cAMP | Bone formation |

| Substance P | Sensory nerve | Neurokinin-1 | cAMP | Bone formation<br>Bone resorption |
|---|---|---|---|---|
| Vasoactive intestinal peptide | Sympathetic nerve | VIP-1R, VIP-2R, PACAP-R | cAMP<br>PGE-2<br>RANK<br>RANKL(down regulate)<br>OPG<br>IL-6 | Bone formation?<br>Osteoclast formation (down-regulation)<br>Osteoclast resorption? |
| Neuropeptide Y | Sympathetic nerve | Y1, Y2, Y4, Y5 and Y6 receptors | G-protein-coupled | Bone resorption |
| Dopamine, serotonin | Sympathetic nerve | adrenergic receptor (Adrβ2), Htr1b receptor | cAMP<br>PGE-2 | Bone formation (in brain)<br>Bone resorption (in peripheral) |
| Catecholamines | Sympathetic nerve | β-2, α-1 adrenergic receptors | cAMP<br>PGE-2 | Bone formation<br>Bone resorption |
| Glutamate | Glutamatergic nerve | NMDA, AMPA, metabotropic Glu (mGluR) and kainate receptors | Ionotropic or ion channel gating and metabotropic or G-protein-coupled | Bone formation |

Bone cells, including osteoblasts, osteoclasts, osteocytes, mesenchymal stem cells, and lining cells, function directly with these neuropeptides through the receptors on the cell surface[105]. Moreover, bone neuropeptides indirectly regulate bone cells via mediation by vascular endothelial cells, immune cells such as mast cells, CD3+ lymphocytes, and macrophages in a process that we termed "neuroinflammation"[96,106,107]. CGRP and substance P from nociceptors of sensory nerve endings act directly on vascular endothelial cells and produce vasodilation effects[108]. Their adhesive and proliferative modulating effects on endothelial cells are dependent on nitric oxide (NO) level, as well as that of other endothelial products,

such as endothelin, hydrogen peroxide ($H_2O_2$), and prostaglandins, involved in bone metabolism[109].

Many other neuropeptides (see http://www.neuropeptides.nl/), including catecholamines, VIP, neuropeptide Y, and glutamate, as well as other molecular mediators, such as adrenomedullin, neurokinin A and B, gastrin-releasing peptide, and cytokine eotaxin, may interact with bone immune cells (mast cells and monocyte/macrophages) and adaptive immune cells (T lymphocytes)[92]. Activation of immune cells by neuropeptides leads to release of preformed and stored histamine, heparin, various newly produced lipids (e.g., LTB4 and PGD2), and cytokine (e.g., IL-6 and TNFα) mediators, amplifying their effects on bone metabolism[110,111]. Conversely, activation of the immune system equally promotes neurotransmitter synthesis and release, even in immune cells (T lymphocytes)[112,113]. However, the latter finding was not the focus of this thesis study.

**Models of bone denervation**

An animal model of peripheral denervation of bone by surgical sciatic neuroectomy has been used as a standard model of disuse osteopenia. However, this model confounds the examination of the effects of motor nerves, sympathetic nerves, and sensory nerves on bone. Chemical sympathectomy by neurotoxin guanethidine dramatically decreases the number of tyrosine hydroxylase (TH)- and VIP-staining fibers, significantly reducing lumbar vertebral and femur mineral content and density and the number of serum osteomarkers and osteoclast numbers in adult rats[114-116]. Capsaicin, a sensory specific neurotoxin, selectively destroys unmyelinated sensory neurons, inducing loss of trabecular integrity and reduced bone mass and strength[117,118]. Pain from fracture/nonunion/joint degeneration and complex regional pain syndrome, such as Sudeck's atrophy (reflexing sympathetic dystrophy), reflects

the direct impact of peripheral neural pathological lesions on bone[94].

**Bone metabolism regulation by the central nerve system**

The development of many syndromes, including hemiplegic-stroke induced osteoporosis, spinal cord injury (SCI)-related skeletal bone loss at earlier stages, heterotopic ossification after head injury, Charcot neuroarthropathy in diabetes mellitus, and osteoporosis in obesity, indicate that the central nerve system affects bone metabolism[119-123]. The finding that leptin as an opening regulator is a potent inhibitor of bone formation acting through the central nervous system initiated research into the central nature of bone mass control and its disorders[120]. Leptin is a small polypeptide hormone secreted primarily by adipocytes in human fat tissue that controls body weight and gonadal function by binding to its receptor on specific neurons in the hypothalamus[120]. Karsenty *et al*. found that leptin- deficient mice (ob/ob type) and leptin receptor-deficient mice (db/db type) both have high bone mass phenotype preceding obesity and coexisting hypogonadism and hypercortisolism.

Observation that hypogonadism and hypercortisolism are both osteoporosis-favoring conditions and lead to a low bone mass phenotype, as well as that leptin has no direct effect on osteoblasts, led to the hypothesis that leptin's bone-regulation effect is controlled by the central nervous system in 2002[120]. In 2009, Karsenty *et al*. verified that leptin inhibits the serotonergic neurons of the brain stem and reduces the synthesis of brainstem-derived serotonin (BDS)[103]. BDS has Htr2c receptors on ventromedial hypothalamic neurons and functions as a potential regulator of bone metabolism through its sympathetic tone, but leptin's abrogation of BDS synthesis inhibits bone mass accrual. Given the newly conceived notion of bone's regulatory role in controlling other physiological processes, such as fertilization and gonadal hormone secretion, bone metabolism in the neural and gonadal systems should be

reexamined[100-102].

### ***1.5 Osteoporosis and fracture repair***

As the skeleton is essential in terrestrial animals, humans ultimately evolved bone, which is of sufficient lightness and strength to prevent disabling fracture during flexible and rapid actions. However, with advancing age in men and in women after menopause, the entire muscular skeletal system, including that involved in neuron-muscle activity; bone tissue metabolism; and bone structure degenerate, increasing the risk of fracture. Systemic skeletal disease characterized by low bone mass and microarchitectural deterioration of bone tissue in aged men and women is considered osteoporosis.

**Etiology of osteoporosis**

Development of osteoporosis is a natural life phase in normal humans. Bone mass diminishes with increasing age as a result of changes in circulating levels of hormones, particularly in decreased estrogen levels after menopause in women. Meanwhile, decreased physical activity in aged people leads to decline of mechanical loading stimulation to the skeletal system. Depressed anabolic and slow bone remodeling activities in aged people reflect not only the body's attenuating metabolism but also negative feedback to other organs[124].

Osteoporosis initially develops through cellular and biochemical disturbance of stem cells, osteocytes, osteoblasts, and osteoclasts in bone mesenchymal tissue. The dysfunction or re-coordination of these bone cells alters osteoid generation and degradation, mineralization, and osteon constitution at the macro level of bone structure and its biomechanical properties[125]. Initially, bone trabecular thins with increasing perforation, reducing connectivity and quantity, followed by thinning of

the layer of cortex and growth of its external diameter. This fabrication of long bone is the fundamental process in the aged[126]. Under Raman microscopic imaging analysis, the mineral content (degree of mineralization) of osteoporotic tissue and the carbonate content are observed to decrease while HAP crystal size and structural perfection increase. Meanwhile, the acid phosphate and Mg content decline, which subsequently changes the crystal–collagen ratio and microarchitecture[127-129]. Decreased cross-linking between subchondral bone and thinning trabeculae during the osteoporotic bone resorption process leads to fewer, thinner connections, which increases the fragility and flexibility of the femur neck[125]. The subtle reduction of bone mass in the transverse direction increases the intensity of trabecular in the loading axis, a structural change that may effectively resist loading when the direction of the loading coincides with that of the trabecular orientation. However, such structural change narrows the tolerable loading directions, which in turn may increase fracture risk[125,126].

**Epidemiological review of osteoporotic fracture**

Osteoporotic fracture is a common cause of disability and a major contributor to medical cost in many countries[130-132]. Caucasians are most vulnerable to osteoporosis, followed by individuals of African origin and individuals of Asian origin[133]. Worldwide, 100 to 200 million people are at risk of osteoporotic fracture each year[134-136]. Statistics indicate that 25% of the European population was over the age of 65 by the end of 2012 and that 52 million will be over 65 by 2020 in the United States. In China, there will be 250 million individuals 60 this largest developing country until 2020[137]. Zhang *et al.* analyzed pooled data published in 91 articles up to January 2013 regarding 139,912 Chinese adults to assess osteoporosis prevalence in Mainland China, Taiwan, and Hong Kong[138]. They found the age-standardized prevalence of osteoporosis adjusted by the WHO world standard in those aged 50 years was 24.6%

in women and 3.5% in men at the lumbar spine and over 13.3% in women and 5.9% in men at the femur neck[139]. In Mainland China, they found the 50-year age-standardized prevalence of osteoporosis to be 23.9% and 12.5% in women and 3.2% and 5.3% in men, respectively, at the lumbar spine and femur neck[138]. In 2010, about one third of Chinese women aged 60–69 years and half of those aged 70 years and over were found to have osteoporosis, while men in the same age group were found to have a much lower prevalence of osteoporosis. Due to changing demographics due to population aging and increasing life expectancy, an astonishing number of older people will have osteoporosis and osteoporotic fractures in the near future[140-142].

Low bone mass and osteoporosis, a systemic condition, increase the risk of almost all types of fractures. Fractures at the proximal femur (hip), the vertebrae (spine), and the distal forearm (wrist) have long been regarded as the most frequent types of osteoporotic fractures. Hip fractures are regarded as the most severe osteoporotic fractures and are considered the international barometer of osteoporosis because they are strongly correlated with low bone mineral density (BMD), are more expensive to treat, and cause more disability than other types of osteoporotic fracture. With age-related decrease in BMD, fracture risk at the proximal femur rises, especially in women, who are affected by estrogen deficiency after menopause and live longer than men[143]. Osteoporotic fracture is associated with increased morbidity, mortality, and cost. The cost of treatment, which was RMB 17,007 per year per patient in China in 2012, will increase with the expected increase in the osteoporosis population to 250 million in China by 2020[137,144]. Gaining understanding of the biological process of fracture is essential for its prevention and cure.

**Fracture healing process**

Ontogenetic development is characterized by a series of steps initiated at fertilization

and terminating with the differentiation, growth, and maturation of specialized tissues and organs. These developmental processes involve both the molecular specialization that accompanies and determines cellular differentiation and the biological morphogenesis in which cells are organized into functional structures. Although this developmental process is terminated when animals reach sexual maturity, the morphogenetic processes could be reinitiated in specific tissues, such as bone, as a consequence of injury.

The bone fracture healing process is a special post-natal repair that recapitulates aspects of embryological skeletal development[145,146]. The repair process occurs during three overlapping phases—the inflammatory, repair and remodeling phases[147]—that are similar in large animals like humans and small animals like rats. In rats, diaphyseal fracture first leads to blood vessel rupture in the surrounding soft tissue and inside bone, as well as damage to musculoskeletal tissue, which promotes the initiation of the inflammatory cascade. Inflammation along with vasodilatation and exudation of plasma and leukocytes and fibrinogen in the fracture gap forms fracture hematoma as a result of blood clotting. This process occurs 24 h after fracture and is characterized by hypoxia due to vessel breakage and the presence of low pH and blood-derived inflammatory cells with proinflammatory and anti-inflammatory cytokines. Short-lived (one-day) polymorphonuclear neutrophils (PMNs) first recruited at the fracture gap rapidly accumulate during the first hour after injury. Several chemokines, such as C-C motif chemokine 2 (CCL2) and IL-6, are secreted to attract longer-lived macrophages.

Macrophages located at the endosteal and periosteal surfaces are pivotal for intramembranous ossification during early fracture healing and later endochondral ossification. A large number of inflammatory cytokines, such as IL-1, IL-6, TNF,

RANKL, the TGF-β superfamily, and the bone morphogenetic protein (BMP) family (BMP-2, 4, 5, 6), are present from the first 24 h to 7 days after injury[148,149]. Meanwhile, revascularization is initiated after the tissue damage caused by hypoxia. Inflammation cells also are existed along with the complex network of interactions among immune cells; resident tissue cells; MSCs; and released angiogenic factors, such as angiopoetin-1 and VEGF. Endothelial cells are recruited and migrate from pre-existing periosteal and endosteal vessels into the hematoma to form new blood vessels. This revascularization is a relatively long- term process that slowly increases the blood flow between days 3 and 5, reaching its peak after week 2. The extent of blood flow substantially affects bone fracture healing; low blood flow promotes revascularization during the early stages of fracture healing with greater interfragmentary movement, whereas greater blood flow in the later phases of repair is associated with more stable fixation[150].

Callus formation, which partially overlaps with the inflammatory phase, mainly consists of intramembranous bone formation, which begins as early as 3 to 7 days after injury in rats. Intramembranous ossification usually occurs at the periosteum distant from the avascular fracture ends. Precursor cells derived from periosteum-like PDSCs differentiate into the osteoblast cells involved in intramembranous bone formation[151]. Bone formation is considered to start in the region where the periosteum and vascularization are not affected by the trauma, which is why intramembranous ossification is initiated at the site distant from the fracture ends. The fracture gap is a hypoxic and low pH area harmful to MSCs, and the interfragmentary movement of the fracture gap causes large tissue strain and high hydrostatic pressure, which are detrimental to osteoblast survival[147,152].

Further callus growth is driven by production of chondrocytes derived from specific

MSCs recruited systemically from the circulation and locally from surrounding soft tissues and bone marrow[153,154]. Stromal cell-derived factor-1 (SDF-1) and its G-protein-coupled receptor CXCR-4 form an axis (SDF-1/CXCR-4) that is a key regulator of recruiting- and homing-specific MSCs to the site of trauma during endochondral fracture healing. Once MSCs are recruited, molecular cascades involved with collagen-I and collagen-II matrix production and several peptide-signaling molecules, such as transforming growth factor-beta (TGF-β) superfamily members (TGF-β2 and TGF-β3 and GDF-5), are involved in chondrogenesis and endochondral ossification[155,156]. Cartilaginous tissue formation at the fracture gap 7 to 10 days after fracture in rats is the result of insufficient blood supply, greater interfragmentary movement, and high hydrostatic pressure, which benefit chondrocyte differentiation and proliferation but impair osteoblast activity[157,158]. Because fracture healing requires sufficient blood supply, angiogenic blood vessel ingrowth occurs at the repair site, which causes chondrocyte apoptosis and cartilaginous degradation. The blood vessels invading the calcified cartilage carry MSCs and monocytes, which differentiate into osteoblasts and osteoclasts, resorb the calcified cartilage, and form woven bone[159].

After bony bridging occurs between days 28 and 35, the strain on tissue in the fracture gap and between the remaining callus wedges is sufficiently low to enable replacement of connective and granulation tissues by intramembranous ossification[160]. Once the diaphyseal fracture gap is filled with newly formed woven bone, osteoclastic activity begins at both the outer surface and inner woven bone. Vascularization during remodeling is reduced to pre-fracture levels, and the number of cytokines decreases except for that of some cytokines, particularly IL-1, TNF, and BMP, which remain highly expressed until reshaping of the diaphyseal bone is completed[161].

**Treatment of osteoporotic fracture**

A multinational survey of osteoporotic fracture management clearly indicates that many orthopedic surgeons fail to identify, assess, and treat patients with fragility fractures. Osteoporosis increases the number of traumatic fractures and contributes to their severity. The management of osteoporotic fractures is difficult due to poor bone quality, and the inadequate fixation strength of the implants used to stabilize the fracture until union occurs may be inadequate. In particular, fracture fixation is associated with increased rate of complications. Various reports suggest a nonunion rate of 2−10%, a post-surgery malalignment rate of 4−40%, a metal work failure rate of 1−10%, and a re-operation rate of 3−23%[162,163].

A common medical condition that most people experience more than once throughout their lifetime, bone fracture usually occurs due to falls, traffic accidents, and repetitive forces. Although most bone fractures heal completely without any significant complications with either non-surgical or surgical treatment, challenges remain in promoting bone fracture healing, such as delayed union and non-union, especially in osteoporotic and open high-energy fracture[163,164]. Osteoporosis influences the early, middle, and late period of fracture healing through the combined effects of prolonged endochondral calcification, high activated osteoclast cell production, and deceleration of the increase in bone mineral density followed by poor development of mature bone at the fracture area[165-167]. In clinical practice, an open high-energy fracture is less likely to result in an uncomplicated union than a closed, less traumatic fracture. The anabolic response in these cases may be impeded by tissue disruption around the fracture with avascularity and low oxygen tension. During these situations non-specific wound-repairing anabolic phenomena, such as angiogenesis and cellular recruitment and proliferation, are delayed along with more bone-specific anabolic

events, such as osteogenic differentiation and bone matrix production[168].

Treatment with osteogenic factors, gene therapy, or cell therapy achieves better surgical outcome in bone fracture healing. Bone morphogenetic proteins (BMPs) are osteoinductive agents useful in treating difficult fractures, non-unions, and large defects. However, there are several limitations in using BMPs, including (i) need for a high dose due to the rapid degradation of unprotected protein(s), with the effective concentration species dependent (in humans much higher concentrations are needed than in rodents and dogs, resulting in a large financial burden); (ii) difficulties in the incorporation of these proteins into proper vehicles due to their unstable chemistry; (iii) brief presence at the site of the lesion; and (iv) severe limitations in the gene therapy approaches apart from direct cell transduction or DNA delivery by gene-activated matrices. Intermittently administered parathyroid hormone (PTH), another important factor in bone homeostasis with both anabolic and catabolic actions, is known to increase both cortical and trabecular bone mass. While intermittently administered PTH thus has an established place in osteoporosis treatment and appears promising in closed the bone-fracture model repair, it was not found to increase the rate of union in an open fracture model[124,169-173].

Besides biomolecular therapy for treatment of osteoporosis and associated fracture, electromagnetic field stimulation has proven to offer some benefit in the treatment of delayed union and non-union of long bone fracture. However, Griffin reported its effects to be inconclusive and insufficient[124]. There is some evidence that low-intensity pulsed ultrasound might be an effective treatment for healing of non-unions because of its ability to enhance maturation of the callus. However, the critical role of low-intensity pulsed ultrasound (LIPUS) for fracture healing remains unknown because of a lack of controlled trials of treatment of delayed unions and non-unions.

More homogeneous and a greater number of controlled series are needed to further investigate its efficacy[164,174-176].

The preceding review of research into Mg, fracture, and osteoporosis indicates that the current knowledge base regarding osteoporosis and its treatment lacks a basic understanding of the effects of the loss of trace elements, especially Mg, on osteoporosis. Based on close analysis of previous findings, we propose that Mg might be beneficial in the development of treatments to prevent osteoporosis and promote osteoporotic fracture healing. This thesis assesses this proposition by exploring the osteogenic effect of Mg and its application to fracture healing in an OXV rat model.

## ***1.6 Hypotheses and objectives***

### Hypotheses

Based on the observation that Mg implantation in the rat femur canal induces new bone formation at the periosteum, we hypothesize the following:

I. The sensory nerves of the periosteum may play a crucial role in the osteotropic effect of Mg.

II. Sensory neuropeptide CGRP and Mg ions may directly affect MSC proliferation, migration, and osteogenic differentiation.

III. Mg ions may enhance synaptic replasticity in DRG neurons *in vitro*.

IV. Cellular membrane Mg ion channel MagT1 may contribute to Mg influx in cells.

V. Pure Mg metal may be used to enhance bone fracture repair in OVX rats.

### Objectives

I. To understand the osteogenic role of unmyelinated sensory nerves and neuropeptides in Mg-induced new bone formation.

II. To evaluate the effects of CGRP and Mg ions on MSC proliferation, migration,

and differentiation *in vitro*.

III. To examine the effect of Mg ions on DRG neural synaptic plasticity *in vitro*.

IV. To confirm that cellular membrane channel MagT1 is critical in Mg cell influx.

V. To evaluate the effect of Mg on fracture healing in OVX rats.

# Chapter 2

## Role of sensory nerves
and
## CGRP
in
## Mg-induced new bone formation

## 2.1 Introduction

Before our detection of pure Mg osteogenesis in the rat femur, Witte *et al*. observed the same phenomenon after implantation of an Mg alloy rod into the rat femur canal[28]. Eighty years ago, both Lambotte and McBride observed the periosteal proliferation progress and remarkable stimulation of periosteal bone formation with application of Mg (99.7%) and Mg-Al-Mn alloy screw transfixion in the treatment of bone fracture of humans, rabbits, and dogs[11]. However, their observations were challenged by other findings, and Mg-evoked periosteal bone formation has not thoroughly studied since. Thus, this attempt to explicate the mechanism of Mg-induced new bone formation is very important for exploring Mg as a biomaterial.

Hypothesizing that Mg ions released from degradation in bone marrow stimulate nerve endings in the periosteum and trigger new bone formation, we proved that the new bone-forming process terminated after stripping of the periosteum. Since there are dense sensory nerve fibers and MSCs in the periosteum, Mg's bio-effect was hypothesized to be dependent on biofactors such as neuropeptides, PDSCs, and BMSCs. This hypothesis was proven by observation of denervation of the rat sensory nerve in the femur through long term and high-dosing capsaicin administration subcutaneously above the rat spine. In capsaicin-treated rats, new bone formation around the femur is significantly less than that of controls after Mg pin implantation.

By immunochemical staining of the rat femur section, we observed the massive accretion of CGRP in the newly formed cortical bone region of Mg-implanted femur diaphysis in a treated group compared to a control group. When, based on understanding that cortical bone CGRP is derived from the dorsal root ganglia (DRG), we isolated the DRG at the L4 lumber level, sensory nerves out to constitute into sciatic nerve. Immunochemical staining of the L4 DRG section showed more densely

stained CGRP in Mg-implanted rats compared to controls, indicating that increased CGRP in newly formed bone was rooted from axon terminals of DRG neurons. Local injection of BIBN4096bs (cellular CGRP receptor antagonist) resulted in decrease in the rate of new bone formation around the injection site after Mg implantation. Based on our findings, we hypothesized that mass neuropeptides released from sensory nerve endings after Mg implantation promote new bone formation in the periosteum region.

## 2.2 Materials and Methods

Thirty one three-month-old female S/D rats were purchased from CUHK Laboratory Animal Services Centre. The animal experimental protocol, which included Mg-pin implantation, capsaicin treatment, and locally BIBN4096bs administration, was approved by the Animal Ethics Committee of the Chinese University of Hong Kong (Ref. No. 13/003/MIS-5; Appendix I). All rats were divided into four groups: (1) a control group implanted with 18G needles of a length of 20 mm (n=6), (2) a pure Mg-pin implantation group (n=6), (3) a pure Mg-pin implantation with capsaicin-treatment group (n=10), (4) a pure Mg-pin implantation with BIBN4096bs administration group (n=6), and (5) a pure Mg-pin implantation with femoral periosteum stripping group (n=3). All rats had surgery on the right femur.

### 2.2.1 Intramedullarily implanted Mg pin into the rat femur

**Pure-Mg cylinder pin preparation**

Pure Mg cylinder pins with a diameter of 12.8 mm and a length of 20 mm were provided by our collaborators from Peking University. The Mg pins had been made by copper mold injection casting under an argon atmosphere. In brief, high purity Mg (99.99%) was placed in a quartz tube and melted, then the melted Mg was quickly injected into a copper mold to obtain rod samples. X-ray diffraction (XRD) was performed using a Rigaku-D/maxrB Diffractometer (Rigaku Corporation, 9009 New Trails Drive, The Woodlands, Texas) operated at 40 kV and 100 mA at room temperature to verify the amorphous structure of the samples using Cu $K_{\alpha}$ radiation at a scan rate of 4° $min^{-1}$. Differential scanning calorimetry using a Thermal Analysis Corp Q100 Analyzer (Anasys Instruments Corp., 121 Gray Ave, Suite 100, Santa Barbara, California) was used to identify the thermal dynamic properties of prepared

samples.

**Intramedullary implantation**

Three-month-old female S/D rats were used to investigate bone response to Mg pin *in vivo*. In brief, rats were anesthetized via intraperitoneal injection with a combination of ketamine (75 mg $kg^{-1}$) and xylazine (10 mg $kg^{-1}$). The right knee of the rat was exposed and a tunnel of 1.28 mm in diameter and 30 mm in length was drilled in the medullary cavity from the distal femur along the axis of femoral shaft. Before surgery, Mg pins 1.2 mm in diameter and 20 mm in length were sterilized by immersion into 70% ethanol for 30 min and then autoclaved. The sterilized pure Mg pins were implanted into the femur canal and the wound was carefully sutured. The rats were housed in an environmentally controlled animal care laboratory after surgery. Sequential radiographs and *in vivo* HR-pQCT scanning of the distal femur were performed every week post-operation to week 8 for general inspection under general anesthesia.

### 2.2.2 Periosteum stripping

After anesthetization via intraperitoneal injection with a combination of ketamine (75 mg $kg^{-1}$) and xylazine (10 mg $kg^{-1}$), the right thigh of three female S/D rats was incised from the lateral side and exposed to femur bone. The muscle tissue was bluntly dissected from the periosteum, which was stripped cleanly using sharp forceps from the middle to distal femur shaft region. The right femur bone with periosteum stripping was implanted with Mg pins from the distal femur condyle. X-ray and micro-CT scanning were performed two weeks later to monitor the new bone formation (Figure. 2.2.1).

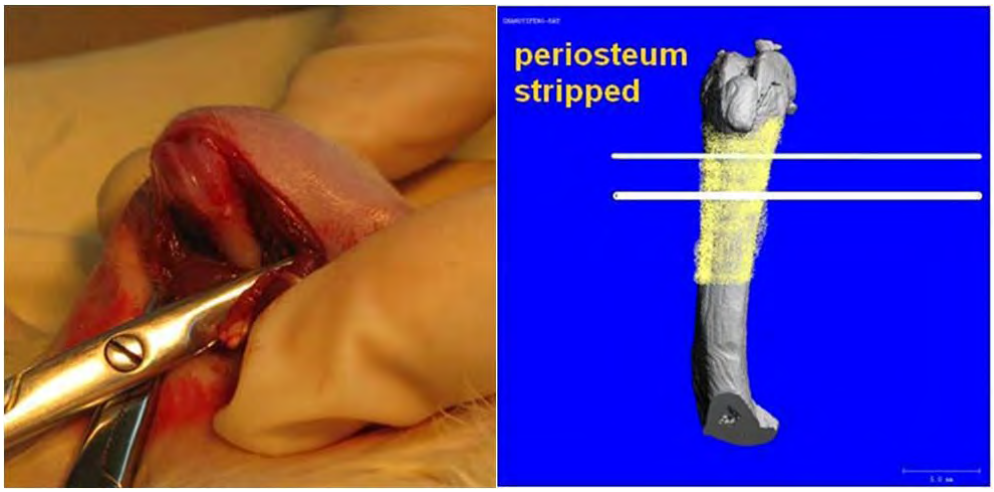


**Figure 2.2.1.** The rat femur periosteum stripping surgery (left). ROI 5-mm long by micro-CT scanning (right) was between two white lines.

### 2.2.3 Capsaicin administration

Ten three-month-old female S/D rats were treated with a high dose of capsaicin (150 mg/kg) over three consecutive days (30 mg/kg on day 1, 50 mg/kg on day 2, and 70 mg/kg on day 3) according to the protocol established by Yuxiang Ding et al[177]. Previous studies showed that capsaicin injection results in a 30–50% mortality rate due to pulmonary edema. To avoid pulmonary edema, the rats were denied drinking water for at least 6 h before capsaicin injection. Capsaicin (Sigma Aldrich, St. Louis, MO, USA) and vehicle solution (10:10:80 V/V of Tween-80, ethanol, saline) were freshly prepared before treatment each day. The capsaicin was sonicated in the vehicle solution until it was homogenously suspended. The rats were subcutaneously injected with 0.1 ml/100 g of capsaicin solution at the L3 to L5 lumber level. To prevent injection reflux, the needle was left in the skin for 30 s after injection. At day 4 of capsaicin injection, an Mg pin was implanted into the rat femur canal. Six of the 10 rats that underwent capsaicin treatment survived throughout the entire study, with

four dying due to high irritation by high-dose capsaicin administration (Figure 2.2.2).

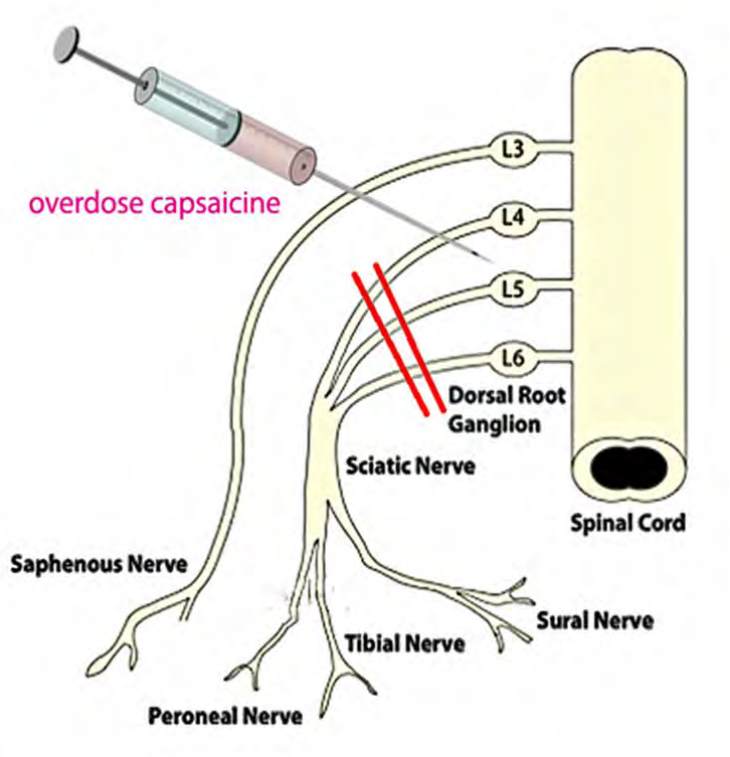


**Figure 2.2.2.** Capsaicin injection at the L3 to L5 lumber level destroyed sciatic sensory nerves of the femur bone.

### 2.2.4 CGRP receptor antagonist BIBN4096bs administration

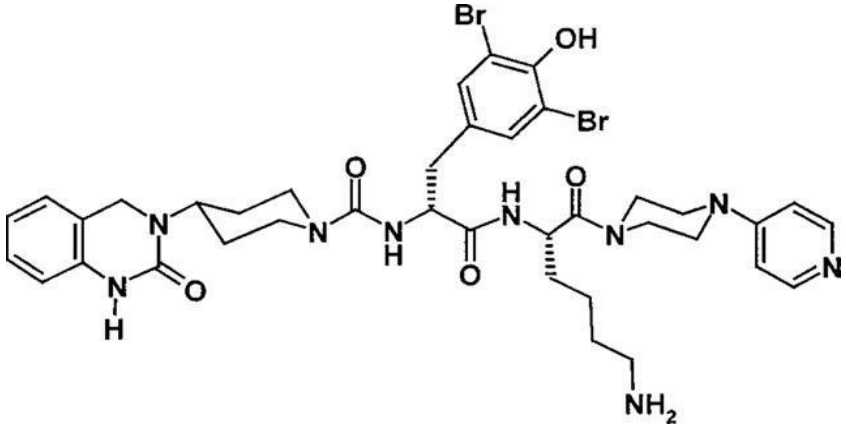


**Figure 2.2.3.** The structural formula of BIBN4096BS *(1-piperidinecarboxamide,-N-[2-[[5-amino-1-[[4-(4-pyridinyl)-1 piperazinyl]carbonyl] pentyl]amino]-1-[(3,5-*

*dibromo-4-hydroxyphenyl) methyl]-2-oxoethyl]-4-(1,4-dihydro-2-oxo-3(2H)-quinazolinyl)-,[[R-(R,(R*,S*)]).*

BIBN4096BS is a potent and novel selective CGRP receptor antagonist with a blood half-life of 13 hours[178] (Figure 2.2.3). BIBN4096BS (purity 99.14%, Shanghai Haoyuan Chemexpress, Shanghai, P.R. China) was initially dissolved in 0.5 ml of hydrochloric acid (1N) before adjustment of the pH value to 6 with sodium hydroxide. In their study, Silke Hirsch *et al.*[178] used a BIBN4096bs dosage of 300 μg/kg. In the current study, BIBN4096bs was diluted in 0.9% NaCl to a stock solution of 750 μg/ml, of which 100 μl BIBN4096bs was injected into the midshaft of the rat right femur from the lateral thigh and prevented from entering the muscle throughout the study. After Mg pins had been implanted into the right femur canal, BIBN4096bs was injected locally at the midpoint of the right femur shaft. BIBN4096bs injection was performed every 48 h and lasted two weeks. After injection micro-CT scanning and analysis were performed.

***In vivo* imaging of indodicarbocyanine (Cy5)-labeled BIBN4096bs rats**

The results of chemdraw analysis of Cy5-labeled BIBN4096bs (Guangzhou Ribobio Co. Ltd., GuangZhou, development district, Mainland China) is shown in Figure 2.2.4.

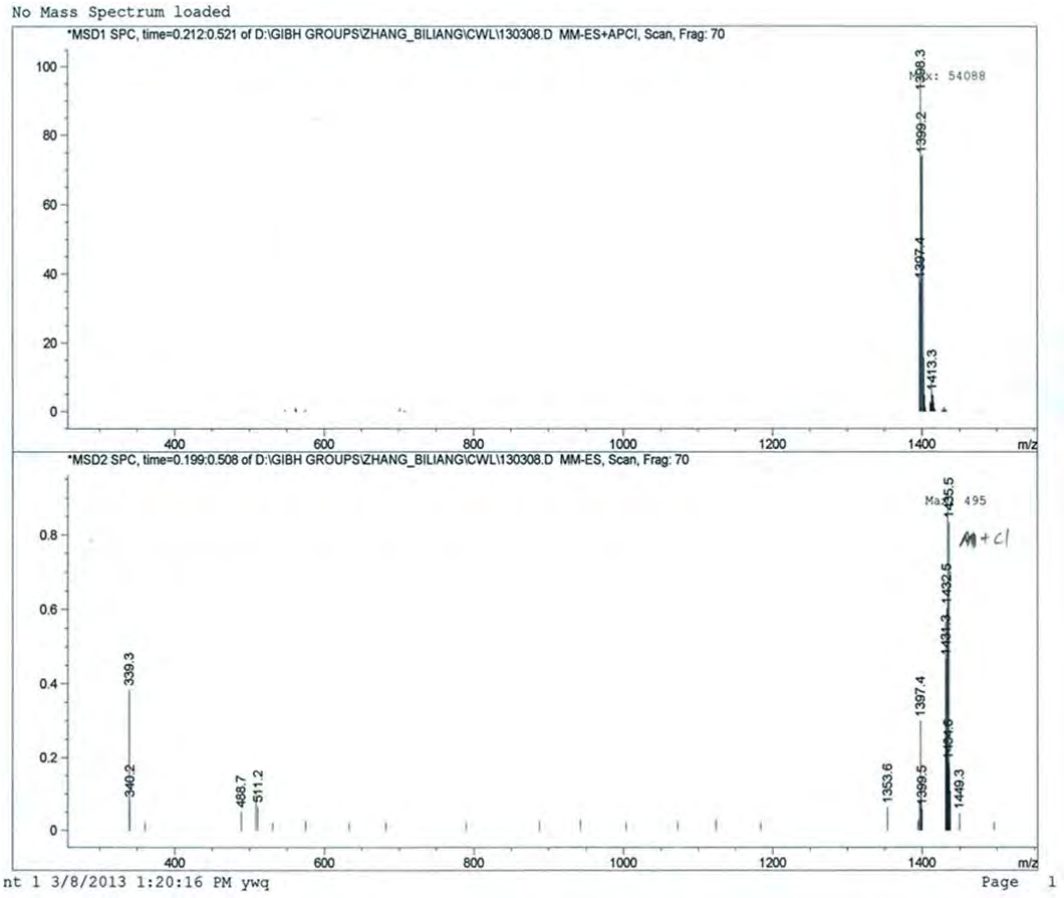


**Figure 2.2.4.** Main chemical molecules of Cy5-labeled BIBN4096bs with a molecular weight of around 1400 according to the mass spectrum report. Chemical formula: C75H88Br2N11O6+, molecular Weight: 1399.38. m/z: 1398.53 (100.0%), 1399.53 (81.2%), 1396.53 (50.2%), 1400.52 (47.6%), 1397.53 (43.4%), 1401.53 (41.5%), 1400.53 (36.4%), 1402.53 (16.9%), 1398.54 (16.8%), 1401.54 (8.8%), 1403.53 (5.2%), 1399.54 (5.0%), 1399.52 (4.0%), 1402.54 (2.1%), 1400.54 (2.1%), 1401.52 (2.0%), 1402.52 (1.6%), 1404.54 (1.0%)

Three female S/D rats aged 3 months were anaesthetized with ketamine/xylazine before the body hair was shaved completely from neck to tail. The rats were kept in a warm cage to maintain their body temperature before chemiluminescence image detection was performed. After Cy5-labeled BIBN4096bs had been diluted in 0.9%

NaCl to a stock solution of 750 μg/mL (pH 6.0), 100 μl of the prepared solution was injected cross-muscularly into midway through the femur shaft, with fluid injected at the point at which the needle tip reached the bone surface. Chemiluminescence images were captured using an IVIS imaging system (Xenogen, Alameda, CA, USA; 200 series) equipped with white-light excitation, charge-coupled device camera-based fluorescence detection, and a filter (band-pass excitation 650 nm and emission 670 nm). Successive images were taken 0, 5, 15, and 30 min and 6 and 24 h after direct cy5-BIBN4096bs injection. After the experiment had been completed, the rats were sacrificed by injection of high-dose phenobarbital before the lungs, heart, liver, spleen, kidneys, and femur were isolated to perform fluorescence imaging (Figure 2.2.5).

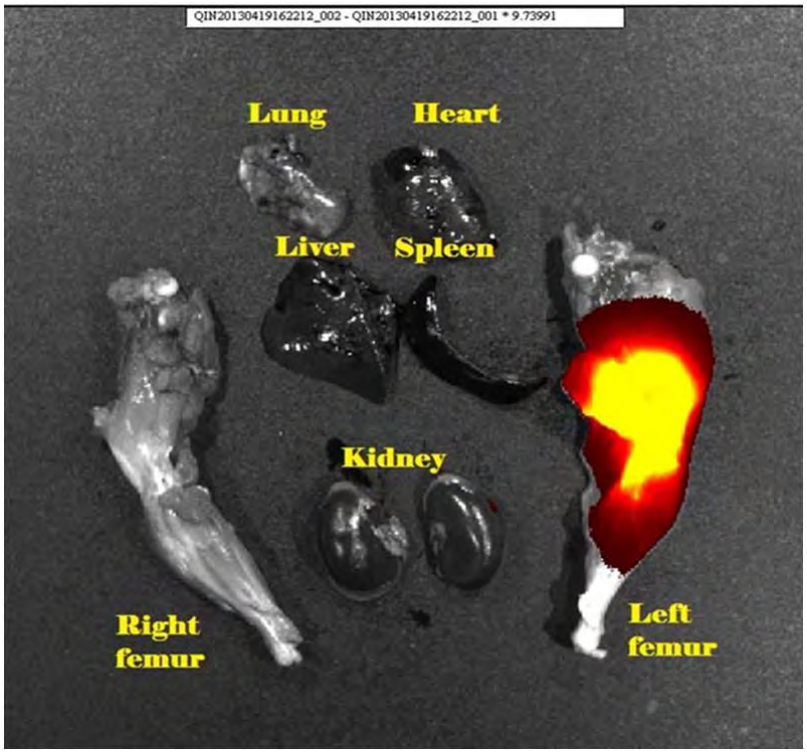


**Figure 3.2.5.** The bright light indicates the presence of cy5-labeled BIBN4096bs. The injection site was the mid-shaft of the left femur (top). The femur, lung, heart, liver, spleen and kidney were isolated 48 h later. Cy5-labeled BIBN4096bs was observed only at the left femur, indicating it had not traveled to any other organs or the lateral femur (below).

### 2.2.5 Imaging and histology

**Radiographic assessment**

Radiographs taken at week 2 post-surgery were analyzed according to our established protocol[179]. The whole femur images of Mg and Mg plus capsaicin groups were compared.

**Micro-CT analysis**

The femur was harvested after euthanasia and the implanted needle was removed

carefully. The femur was then wrapped in gauze and fitted into the sample tube (Ø 38 mm) and scanned with micro-CT (μCT40, Scanco Medical, Brttisellen, Switzerland) according to our established protocol[179]. The scan range was 5 mm (250 slides), the resolution 16 μm per voxel and 1024 × 1024 pixels, and the scanned area was the mid-shaft line to below 5 mm. ROI was selected from 2D images with a standardized threshold (>220) as mineralized tissue according to the tuning before 3D reconstruction of mineralized tissue was performed according to our established protocol[179] using a low pass Gaussian filter (Sigma = 1.2, Support = 2). Quantitative analysis of the 2D images of the 250 slides was performed. The morphometric parameters that evaluated were all newly formed bone tissue volume (TV), bone volume with high density (BV), and normalized BV with TV (BV/TV) before moment of inertia (p-MOI) analysis was performed.

**Histology and histomorphometric analysis**

Rats were subcutaneously injected with fluorochromes calcein green (5 mg/kg, Sigma Aldrich) 14 days before euthanasia and xylenol orange (90 mg/kg, Sigma Aldrich) 7 days before euthanasia. After micro-CT scanning, some femoral samples were decalcified and others were embedded in methylmethacrylate (MMA) without decalcification and cut by saw microtome (Leica SP1600, Wetzlar, Germany) into sections 200 μm in thickness. For 200-μm section histology, sequential fluorescence labeling was used to study the dynamics of bone remodeling during bone remolding according to our established protocol[179]. The sections were ground, polished to 100 μm, and observed under a fluorescence microscope (Leica Q500MC). L5 (calcein green) and Cy5 (xylenol orange) filters were used to visualize the area of new bone labeled with the fluorochromes. Samples decalcified in 9% formalin acid for 4 to 6 weeks were embedded in paraffin after dehydration in a series of ethanol and xylene

solutions. Thin (6-μm thick) sections were cut and hematoxylin and eosin (H&E) and safranin O staining was performed for evaluation of the newly formed bone morphology under light microscope (Zeiss Aixoplan with Spot RT digital camera, Oberkochen, Germany). Goldner's trichrome staining was performed for the new osteoid in red and the old osteoid in blue. Immunochemical and immunofluorescence staining was performed for detection of neuropeptide CGRP.

**ELISA detection of CGRP**

After the rat femur had been harvested and cut along the middle shaft (length of 1 cm), the cut sticks (~200–300 μl) were placed into ceramic morta and ground into mud. After collecting bony mud into 15 mL plastic tubes, 1 ml of pre-cool lysis buffer with 1M hydrochloric acid was injected into the tube and placed in an ice bath. After 1 h of oscillation and homogenization, the collected bone tissue lysis buffer was placed in a 1.5 ml tube and centrifuged at 12,000×g for 30 m. The supernatant was collected for BCA protein quantitative analysis and 200 μl of supernatant from each specimen was used to perform CGRP quantitative detection by ELISA according to the ELISA kit protocol (elabscience, WuHan, China). The ELISA result was rectified by the protein concentration of each specimen.

**Dorsal root ganglion isolation and CGRP staining**

The right lumber 4 level dorsal root ganglia were isolated using a previously established procedure.[180] After overdose with 2.5% sodium phenobarbital i.p (1.0 ml/400 g), the back fur of the rat was wet by liberal spraying with 0.01% hibitane. Using a surgical knife, a large transverse cut was made in the skin in the middle of the back. The skin was held with the thumb and forefinger of one hand on the caudal side of the cut while the other hand pinched the skin on the rostral side of the cut. The skin

was pulled in the opposite direction to remove all back skin and expose the thoracic and lumbar spinal regions to prevent hair from contaminating the dissection. Laminectomy was performed to remove the vertebral canal roof and expose DRGs and the spinal cord. Using scissors to make an incision in the mid-back region and expose the spinal cord, the dorsal edge of the cut vertebra and overlying muscle were grasped using forceps. The tissue was lifted slightly and one tip of the scissors slid into the vertebral canal. The dorsal root (located between the DRGs and spinal cord) was grasped with forceps, the entire spinal nerve (immediately distal to the ganglion) cut with scissors, and any connective tissue attached to the DRGs was removed. After locating the largest L4 DRG, the DRG was cut and removed. After gently dragging the dorsal root and pulling the DRG into the vertebral canal, the nerves and connective tissue were carefully clipped to remove the DRG to minimize the amount of nerve connected to the ganglia. The DRG was placed in 10 ml PBS with 10% PNS and without $Ca^{2+}$/$Mg^{2+}$ into a tube on ice and marked as the Mg group and the needle group, respectively. After fixation in 4% formalin solution for 24 h, the DRGs were soaked in a 30% sucrose solution for 1 week until the ganglia sank to the bottom. Cryo-sections 10-μm thick were sectioned and CGRP immunofluorescence staining was performed.

## 2.3 Results

### 2.3.1 The periosteum is critical in Mg-induced new bone formation

The femurs with Mg implants experienced substantial new bone formation at week 2, with growth reaching a peak at week 8. The new bone was formed mainly at the periosteum region, making the cortical bone appear thicker than that of the control group. At the medullary region, bone remodeling occurred too rapidly to form mineralized mature bone, so only small cavities scattered along the Mg pin could be observed. These low-density cavities almost disappeared at week 16, when the bone grew more dense and thick (Figure 2.3.1).

After the femoral periosteum had been stripped, new bone formation at weeks 2, 8, 16 was significantly reduced. However, new bone regeneration could be observed in some regions due to the residue of the periosteum tissue that had not been totally stripped responding to the Mg ions. Review of X-rays photos confirmed that Mg implantation leading to new bone formation is greatly restrained by periosteum stripping (Figure 2.3.1).

Using XtremeCT (SCANCO Medical AG, Fabrikweg, Brüttisellen, Switzerland), cross-sectional images of the mid-shaft of the same femur with and without periosteum after Mg implantation were obtained. Review of the images confirmed that Mg-induced new bone formation decreases after femoral periosteum stripping. This finding indicated that week 2 was an appropriate time point at which to explore Mg's osteogenic effect and its mechanism (Figure 2.3.2). Review of clear femur cross-sectional images obtained at week 2 using micro-CT clearly indicated that the periosteum plays an important role in Mg's osteogenic effect. Compared to the bone in the control femurs, the newly formed bone in the Mg-implanted femurs appeared to have a thick halo around the outside cortical bone. In the periosteum-stripped group,

the newly formed bone was significantly diminished at the lunar halo region, with the newly formed bone in the region of the periosteum disappearing at the periosteum-stripped region. However, a piece of newly formed bone could be observed at the right upper side because the periosteum had been retained at this region, directly confirming that the periosteum plays a direct and vital role in Mg-induced new bone formation (Figure 2.3.3).

Review of H&E staining at week 2 after surgery revealed that the newly formed bone and the old cortical bone had very clear cutting lines. The old bone of the inner side had similar morphology with the control cortical bone, and the osteon unions were continuous. At the outer side, newly formed cortical bone was formed with porous osteoid tissue constituted by many newly formed bone islands and numerous cells. This observation indicated the existence of a rapid-reforming process and periosteum-associated vessel branching into the newly formed bone region through many canals, and confirmed that the newly formed bone grows from the outer side to the inner side and that the periosteum is the origin of newly formed bone. Review of the fluorescent staining results showed that rapid and mass osteoid formation had occurred in the Mg-implanted sample. (Figure 2.3.4, A).

In the Safranin O staining images, no red was observed in either both the control or Mg-implanted samples, indicating that no cartilage tissue had formed during the new bone-forming process. In the Mg-implanted sample, the newly formed bone was not stained by red, demonstrating that Mg-induced newly formed bone does not undergo endochondral ossification and may undergo intramembranous ossification. This result led us to consider that MSC osteogenic differentiation but not chondrogenic differentiation is affected by CGRP and Mg ions. The Goldner's trichrome staining results showed that red-stained newly formed osteoid was distributed at the cortical

region of the femur and the presence of many vessel-like canals in the newly formed cortical bone region in the Mg-treated samples. The canals were well connected with the periosteum and many cells had aggregated in the canal cavity, confirming that the periosteum was the key issue tissue contributing to significant new bone formation after Mg implantation in the rat femoral canal (Figure 2.3.4, B).

As bone periosteum is rich with sensory nerve endings that can release neuropeptide CGRP, we analyzed neuropeptide CGRP to study the role of the periosteum in Mg-induced new bone formation. Review of CGRP immunoflourescence staining images revealed that CGRP peptide was scattered in the cortical bone and periosteum. In the Mg-implanted sample, significant CGRP staining appeared on the newly formed bone, especially in the peripheral region of the cortical bone. This result indicated that the periosteum dominantly oriented Mg's osteogenic effect and that CGRP is an important factor directly involved in the Mg osteogenic process (Figure 2.3.5).

Quantitative analysis of CGRP content by ELISA showed that there was twice the CGRP content in the Mg-implanted samples compared to the control samples at week 2 after surgery, confirming that neuropeptide CGRP is a pivotal factor in Mg-induced new bone formation (Figure 2.3.6). Reveal of DRG immunofluorescence staining images revealed that CGRP synthesis was significantly enhanced in the Mg-implanted groups, which could explain why Mg-implanted femur bone contains far more CGRP than needle-implanted femur bone (Figure 2.3.7).

### 2.3.2 Neuropeptide CGRP is pivotal in Mg-induced new bone formation

Review of both the X-ray and micro-CT images revealed that after overdosing with capsaicin administration, Mg-induced new bone formation was significantly reduced. In X-ray images of the Mg-implanted femur, the newly formed bone mainly appeared

at the distal femur region, especially from the mid-shaft to the distal femur. Because the bone remodeling had occurred so rapidly, the newly formed bone appeared looser and full of porous cavities. In the control femur with needle implantation, the femoral cortical bone morphology had undergone no obvious changes after overdose with capsaicin. This result was due to the brief duration (3 days) of capsaicin treatment and innervation (2 weeks), which did not significantly modify femur bone mineral density or structure (Figure 2.3.8).

Review of micro-CT cross-sectional images revealed that periosteum stripping had significantly reduced new bone formation while capsaicin and CGRPR administration either had restricted effect on reducing new bone formation. (Figure 2.3.9). Quantitative analysis by micro-CT showed that capsaicin administration significantly reduced Mg-induced TV by 35% and CGRPR antagonist administration reduced TV by 25%. This indicates that the neuropeptides of sensory nerves are dedicated to Mg-induced new bone formation and that CGRP is an important neuronal factor in this process. The newly formed bone was observed to be closely coupled with the level of neuropeptide expression (Figure 2.3.10).

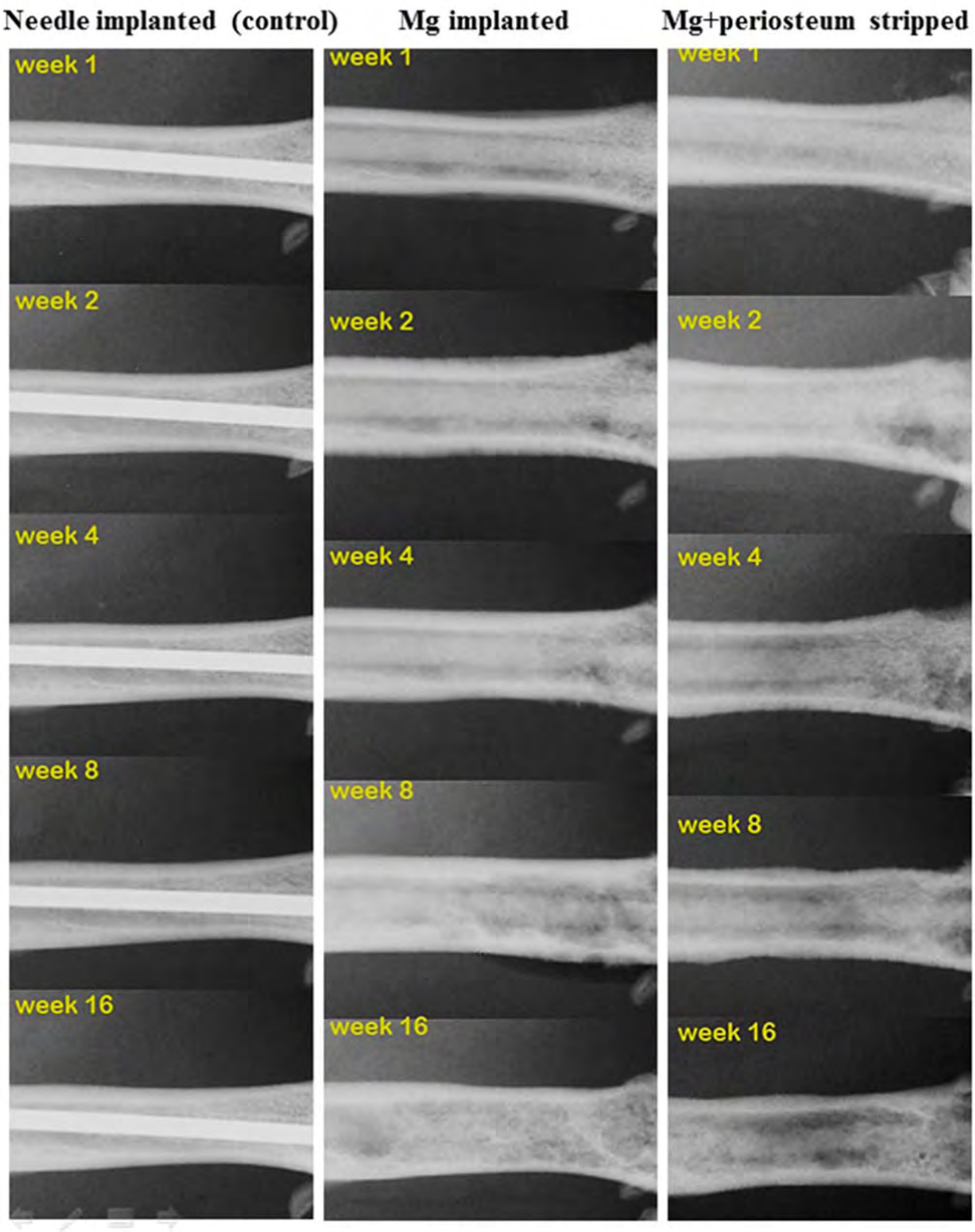


**Figure 2.3.1.** After implantation, X-ray was performed at weeks 2, 8, and 16. Review of the images showed that the femur with needle implantation experienced no visual changes in bone reformation from weeks 2 to 16. The left series of images are of femur with needle implantation, the middle series of femur implanted with Mg rods, and the right series of femur stripped off the periosteum and then implanted with Mg rods.

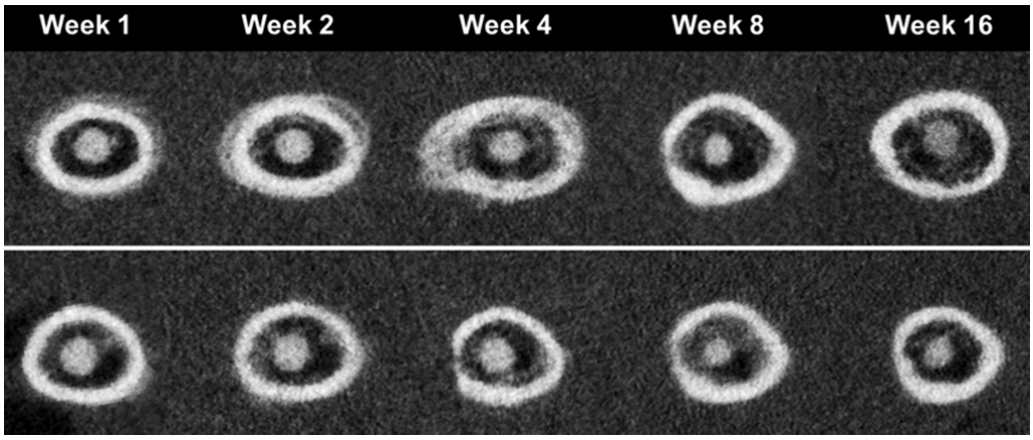


**Figure 2.3.2.** Xtreme CT images showing that Mg significantly affected new bone formation at week 2 after implantation. Cross sections were evaluated at the region marked by the white-line marked area at the femur. The time points for evaluation were weeks 1, 2, 4, 8, and 16.

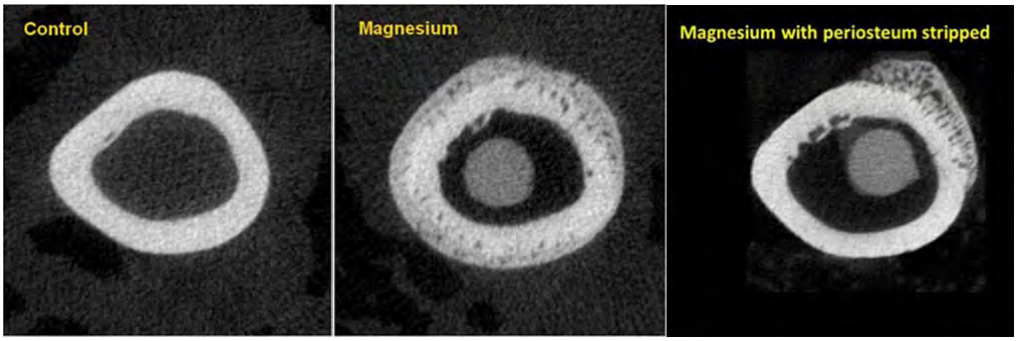


**Figure 2.3.3.** Images of the control femur section with intact periosteum and needle implantation (A); the middle femur section with Mg implantation with intact periosteum (B); and the right femur section with Mg implantation and periosteum stripping (C).

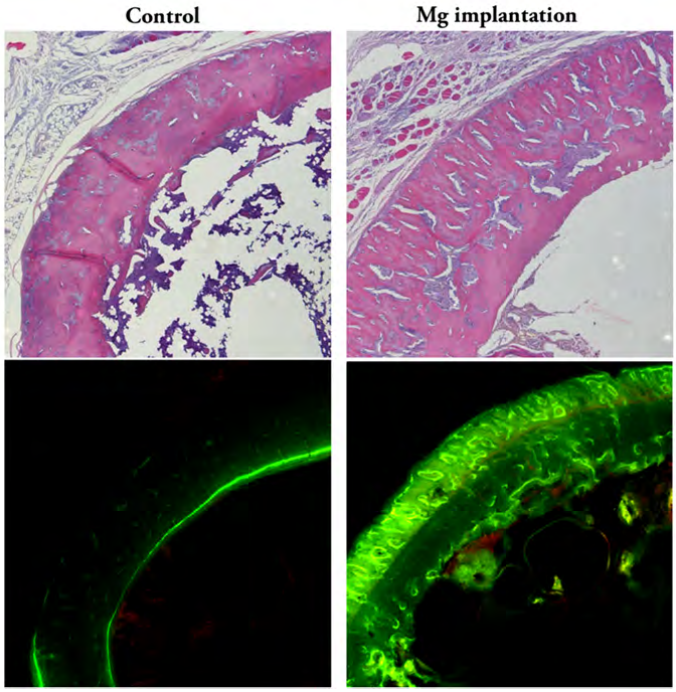


**Figure 2.3.4. (A)** From top to bottom, results of analysis by H&E staining (10×) and fluorescent staining (10×) at week 2 after surgery.

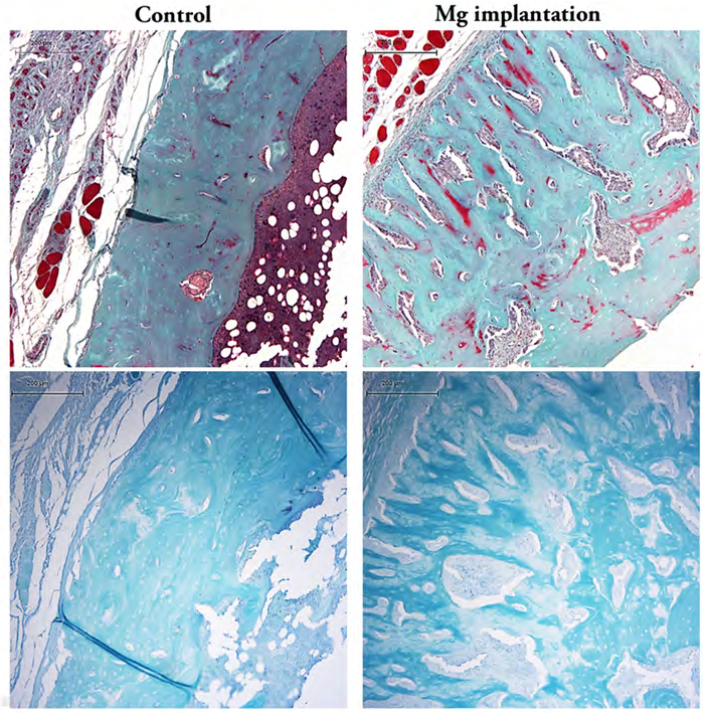


**Figure 2.3.4. (B)** From top to bottom, images of femur cross sections analyzed by Safranin O (20×) and Goldner's trichrome staining (20×) week 2 after surgery. Images on the left are of needle-implanted femurs and images on the right are of Mg-implanted femurs.

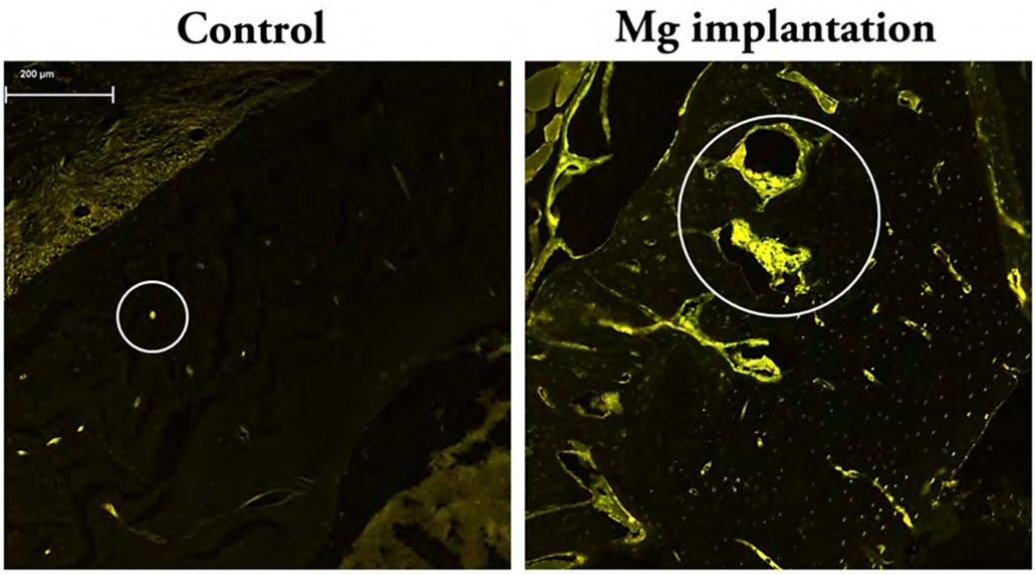


**Figure 2.3.5.** Images of CGRP (light golden spot) of femur cross sections stained using the immunofluorescent method (20×). . Images on the left are of needle-implanted femurs that underwent low CGRP staining (A) and images on the right are of Mg-implanted femurs that underwent dense CGRP staining (B).

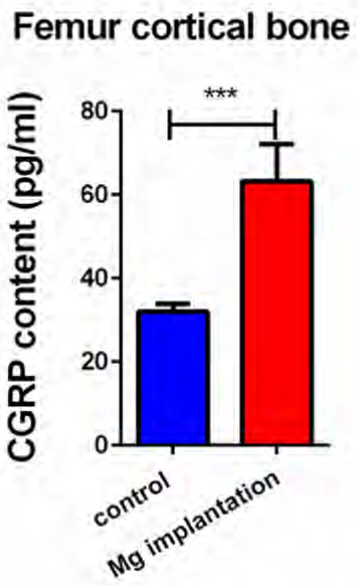


**Figure 2.3.6.** ELISA analysis of CGRP content in cortical bone of needle- and Mg-implanted femurs at week 2 after implantation. Statistical data are reported as mean ± one standard deviation (SD). The paired Student's t-test was performed to evaluate the statistical significance of the differences between each Mg-treated group and needle-treated group using Graphpad Prism 5.0 software. *P<0.05, **p<0.01, and ***p< 0.001; n=3.

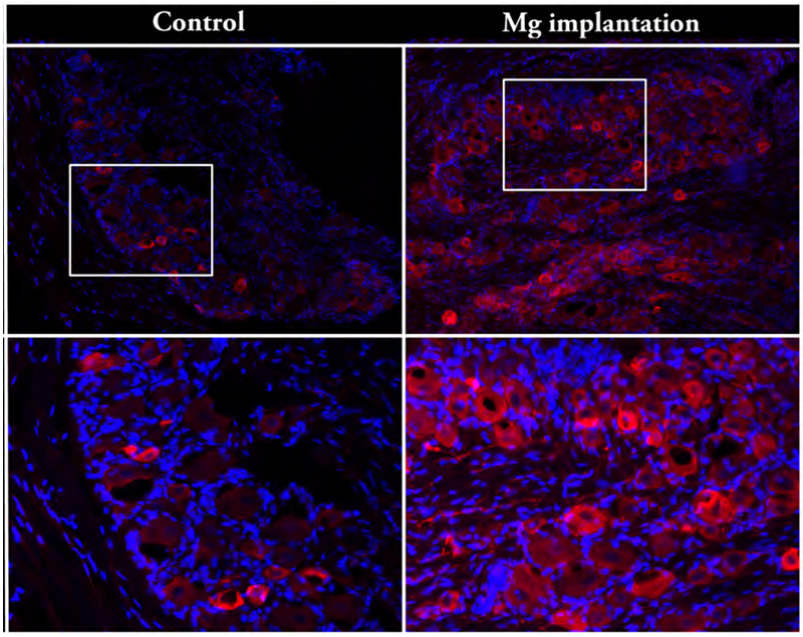


**Figure 2.3.7.** Results of immunofluorescence staining to detect CGRP content in the right L4 dorsal root ganglion isolated from needle-implanted rats (left) and Mg-implanted rates (right). The magnification of the top image was 20× of that of the bottom was 40×. Red marks the CGRP and blue marks the DAPI-stained cell nucleus.

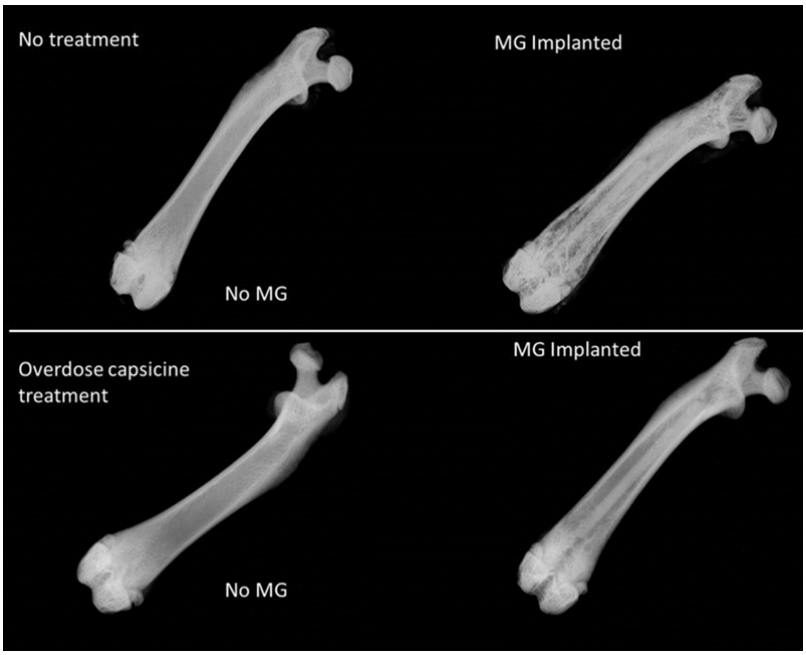


**Figure 2.3.8.** X-ray images of the rat femur. Top images show the femur without capsaicin treatment, the left femur without Mg implantation, and the right femur with Mg implantation. Bottom images show the femur with capsaicin treatment, the left femur without Mg implantation, and right femur with Mg implantation.

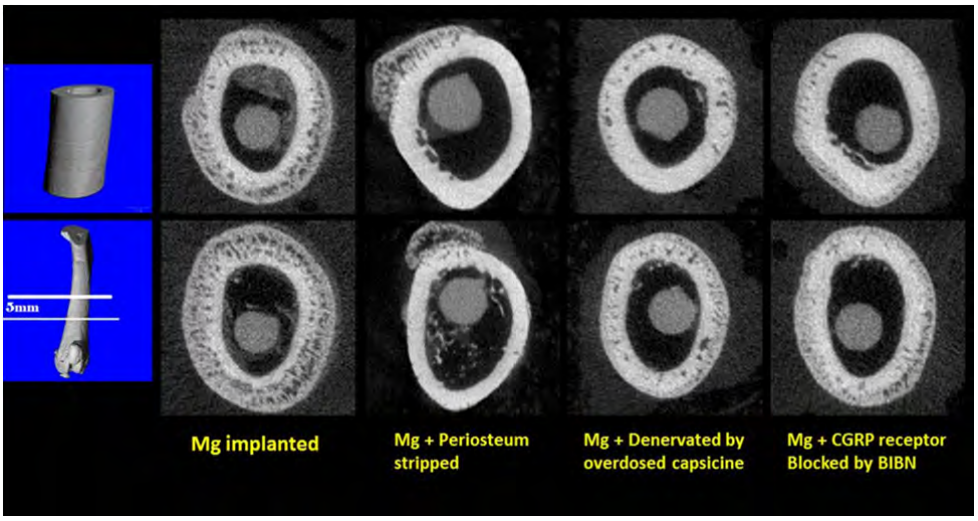


**Figure 2.3.9.** Representative mid-shaft cross-sectional images taken by micro-CT at week 2 of rat femurs implanted with Mg, with Mg with the periosteum stripped, with Mg with capsaicin administration, and with Mg with BIBN4096bs injection.

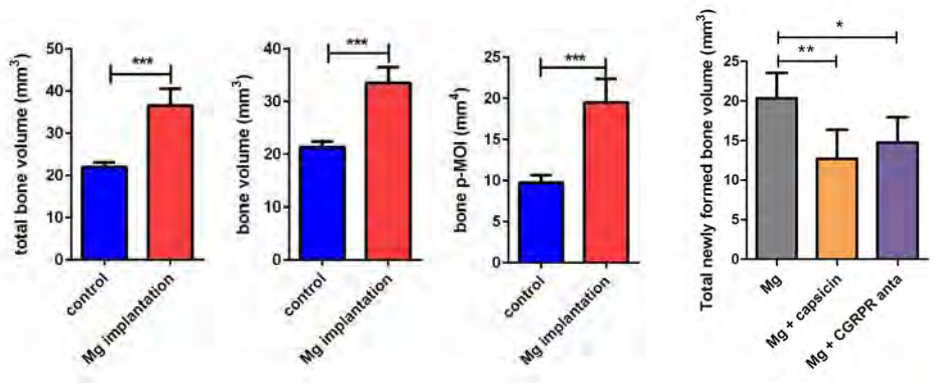


**Figure 2.3.10.** Total femur bone volume (TV), high density bone volume (BV), and ρ moment of inertia (ρMOI) of needle- and Mg-implanted rats (n=6 per group; top image). TV of femur without treatment, with capsaicin treatment, and with CGRPR antagonist treatment after Mg implantation measured by micro-CT (n=6 per group; bottom image). All statistical data are shown as the mean ± one standard deviation (SD). The paired Student's t-test was performed to evaluate the statistical significance of the differences between the means in all groups using Graphpad Prism 5.0 software. *P<0.05, **p<0.01, and ***p< 0.001.

## 2.4 Discussion

### Osteogenic effect of Mg

Biodegradable materials, such as biodegradable metals and polymers, have been attracting the interest of clinicians for many years. Compared to polymers, metals have greater mechanical strength and produce less debris and products provoking inflammatory reactions in the body[181]. In cardiovascular and osteosynthesis applications, iron (Fe) and Mg both are good choices. Whereas steel degradation occurs very slowly *in vivo*, that of Mg and its alloys occurs rapidly in physiological media[28]. Mg also possesses good biocompatibility and its Young's modulus is very close to that of natural bone, which makes it particularly interesting for osteosynthesis applications.

One hundred years ago, the periosteum reaction after Mg implantation was observed by Verbrugge, but was considered a purely inflammation phenomenon[11]. Witte observed a high mineral apposition rate and increased bone mass around the Mg alloy rod after intramedullary implantation of Mg alloys into rat femur, leading him to speculate that high Mg ion concentration could activate bone cells[28]. However he did not explore the mechanism of Mg's "activation" to the bone. Later studies proved that Mg alloys, such as MgZnCa and MgSr alloys, promoted new bone formation at the periosteum region after implantation into the rodent femoral canal[22,182]. While some researchers examined bone and Mg implant interface ossification change and cell adhesive behavior in the Mg coating biomaterial[182-185], they did not examine any other phenomena.

In our study, we observed a large quantity of mineralized bone (Figure 2.3.4) and newly formed osteoid distributed mainly at the peripheral region of the femur in the Mg-implanted sample. Safranin O staining showed that the newly formed bone after

Mg implantation was not the result of endochondral ossification, indicating that it may be due to intramembranous ossification, which is the main source of flat bones, such as the skull, occipital bones, mandible, and maxilla, with condensation of mesenchymal tissue. Intramembranous ossification was why the new bone formation was so rapid (1 week after Mg implantation) and produced vessel-like canals, fibrous tissue, and many types of cells (Figure 2.3.4). Figure 2.3.10 shows the results of Mg-induced new bone formation analyzed by micro-CT in terms of TV, BV, and ρ-MOI.

**Sensory neuropeptides in periosteum are critical in the bone-formation process**

We found that newly formed bone appeared at peripheral region after Mg implantation, indicating the involvement of several active players in the peripheral region involved in Mg's biological effect. After Mg implantation, new bone formation appeared at week 1, reached a peak at week 8, and plateaued at week 16. Hydrogen and hydroxyl during Mg degradation were less important factors in our study, in accordance with previous studies showing the significant promoting effect of Mg ions on cell adhesion and migration without providing underlying mechanism.

To prove Mg's new bone-promoting effect was oriented by the periosteum, we stripped the femur periosteum after implantation of Mg into the femur canal. We found that the growth of newly formed bone significantly decreased at the periosteum region, indicating that newly formed bone grows from the periosteum rather than the cortical bone and bone marrow after Mg implantation, and that newly formed bone only appeared at the periosteum-intact region, likely due to Mg ion stimulation of the periosteum. New bone formation requires recruitment and osteogenic differentiation of stem cells (osteogenic precursor cells) with the participation of cell differentiation factors and a nutritional supply (vessel branching)[186,187]. All these factors could be provided by the periosteum, including PDSCs and circulating pluripotential stem cells

from blood vessels, numerous neuropeptides released from sensory and sympathetic nerve endings, and cytokines synthesized by blood capillary endothelium. We thus chose to analyze PDSCs, BMSCs, and neuropeptide CGRP as the key osteogenic regulators to examine the hypothesis that Mg ions from degradation of the implanted Mg pin stimulated sensory nerve endings in the periosteum and abundantly released CGRP. We found that neuropeptide CGRP induced pluripotential stem cells (PDSCs and BMSCs) to differentiate into osteoblasts, leading to new bone formation.

To prove our hypothesis, we designed two experiments to denervate the femur by high-dose capsaicin and to antagonize CGRP's effect by BIBN4096bs injection. Capsaicin is an ingredient in red peppers that activates the transient receptor potential cation channel 1 (TRPV1), which is located at capsaicin-sensitive afferent neurons containing CGRP[177]. Capsaicin exerts a long-term blocking action by increasing cellular Ca and Na influx into mammalian sensory neurons. In adult rats, 100 mg/kg of subcutaneously injected capsaicin could damage up to 17% of small-diameter sensory neurons in the dorsal root ganglia[188]. In our study, 175 mg/kg of subcutaneous capsaicin injection at the L3-5 level significantly destroyed the rat femoral sensory nerve, decreased sensory neuropeptide CGRP release in the femur periosteum, reduced the trabecular volume of the proximal tibia, and increased TRAP 5b level in plasma, but had no effect on bone formation at week 5 after injection[177]. These findings indicate that capsaicin does not influence the osteogenic precursor cell directly, and may thus independently affect the sensory nerve's role in Mg's osteogenic effect. At week 2 after surgery, the Mg osteogenic effect was notable. Micro-CT scanning revealed no significant differences between the capsaicin-treated rat femur and normal rat femur regarding total bone volume. The decrease in newly formed bone in the capsaicin-treated group after Mg implantation thus demonstrated

that the sensory nerve plays a vital role in Mg-induced new bone formation. The results of X-ray imaging and micro-CT scanning (Figure 2.3.8-10) showed significantly reduced new bone formation in the capsaicin-treated femur after Mg implantation, specifically an approximate 35% decrease in new bone formation after capsaicin injection. We found that Mg-induced new bone formation largely depends on secretion of the sensory nerve fibers, which are predominately CGRP-positive peptidergic C-fibers, indicating that Mg-induced new bone formation could be partly reduced by blocking CGRPR in the periosteum.

CGRP has been proven to promote osteogenic differentiation in BMSCs, inhibit osteoclast formation *in vitro*, and partially inhibit bone loss *in vivo* in OVX rats[189-191]. However, knocking out the calcitonin gene (*Calca* -/-) in mice enhances bone mass[192]. These phenomena may be due to a compensating mechanism we have not yet identified, as calcitonin is considered an osteoclast inhibitor and α-CGRP an osteoanabolic peptide. Theoretically, the knock-out phenotype should be used to examine bone mass loss. However, we did not use αCGRP knock-out mice as the Mg-implantation model because the bone loss in the αCGRP-deficient model may have confounded with Mg-induced new bone formation. We thus chose a CGRPR antagonist BIBN4096bs model to verify the effect of neuropeptides on Mg-induced new bone formation (there is another CGRPR antagonist called $CGRP_{8-37}$ that easily degrades[193]). BIBN4096bs is an extremely potent binding compound located at primate CGRP receptors. In a monkey model, 30 μg/kg of BIBN4096bs was found to inhibit CGRP's effect on facial blood flow[194]. When we locally injected 30 μg/kg of BIBN4096bs at the rat right femur to block CGRPR in periosteum cells, it resulted in an approximately 25% reduction in new bone growth after Mg implantation, indicating that CGRP is an important (but not the only) factor in the Mg-induced

osteogenic process and that sensory neuropeptide CGRP is the direct factor in Mg-induced new bone formation.

**Conclusion**

The results discussed in chapter 2 support our hypothesis that sensory nerves in the periosteum play a key role in the Mg-induced osteogenic effect and that sensory neuropeptide CGRP released from the periosteum nerve endings plays a pivotal role in new bone formation. Chapter 3 evaluates the direct effect of neuropeptide CGRP and Mg ions on PDSCs and BMSCs *in vitro*.

# Chapter 3

**CGRP** and **Mg ions**

both

**Promote osteogenic differentiation**

**On stem cells**

***in vitro***

## 3.1 Introduction

Early in the 1500s, Charles Estainne first drew the nerve fibers innervated in the bone on a wood cut panel. De Castro confirmed bone innervation by showing nerve fibers along with blood vessels in bone in 1925[89,90]. Now researchers assert that the bone marrow, mineralized bone, and periosteum all receive both peptide-rich unmyelinated and myelinated sensory nerve fibers including A-β, A-δ and C types. Periosteum is perceived to have denser innervation (99% of total bone nerves) than bone marrow and cortical bone[94]. In GC Corral's study, it was found that above 80% of the unmyelinated/thinly myelinated sensory nerve fibers in bone periosteum express CGRP[195]. There were many types of neuropeptides, including CGRP, substance P, Neuropeptide Y, and glutomines of sensory nerve origin, that played diverse and important roles in bone homeostasis. CGRP as a prominently distributing neuropeptide in the bone sensory nerve fibers has been found to function as an anabolic regulator to osteoblasts.

In chapter 2, it was observed that the massive accretion of CGRP was stained in the newly formed cortical bone region after Mg implantation in femur diaphysis, and cortical bone CGRP content in Mg implanted femur was two times more than the control. This indicated CGRP was an important regulator in Mg induced new bone formation.

Several studies had revealed that adhesive behavior, morphological characteristics, and differentiation destiny of osteoblasts, BMSCs, and fibroblast cells were significantly affected on Mg implant surfaces[182-185]. However, this was just considered the surface topography effect on cells, but not to refer to the Mg ion itself.

In this chapter, we evaluated the effect of CGRP and Mg ions on stem cell proliferation, migration, and differentiation *in vitro*.

## 3.2 Materials & Methods

PDSCs and BMSCs were isolated from the femora of 3 month-old female S/D rats and were characterized by the expression of stem cell surface markers, colony forming ability, and multi-differentiation behavior. The evaluation methods for CGRP and Mg ions included MTT assay, cell migration assay, and osteogenic differentiation assay. All the experiments were conducted at least three times. Unpaired student-t test was used in statistical analysis.

### 3.2.1 Isolation and culture of rat PDSCs and BMSCs

Three month-old female S/D rats were used in this study and the experiments were approved by the CUHK animal research ethics committee (Ref. No. 13/003/MIS-5) (Appendix I). The procedures for the isolation of PDSCs have been established by other researchers[179]. In brief, after being overdosed with 2.5% sodium phenobarbital i.p (1.0ml/400g), the rat thigh was incised and exposed to the femur. Muscle tissue above the periosteum was carefully removed, and periosteum from the midshaft to the distal femur was collected. The collected periosteum tissue was washed and stored in a 4°C antibiotic containing sterile saline. After the tissue was cut into pieces, we put them into a 37°C type I collagenase containing (1mg/ml) DMEM medium supplemented with 10% fetal bovine serum (FBS), 10U/ml penicillin, 100μg/ml streptomycin and 2mM L-glutamine (complete basal culture medium) (all from Invitrogen corporation, Carlsbad, CA, US). The periosteum tissue was digested in a warm incubator for 8 hours. The digestion medium was passed through a strainer mesh measuring 70μm diameters. The filtrated medium was centrifuged (800g, 5 minutes) to isolate PDSCs and the PDSCs were plated at an optimal low cell density

($10^5$ cells /$cm^2$) in a humidified atmosphere at 37°C, 5% $CO_2$ to form colonies. At day 2, after initial plating, the PDSCs were washed twice with PBS to remove non-adherent cells. At days 7-10, they were trypsinized and mixed together as passage 0 (P0).

The PDSCs were subcultured after reaching 80-90% confluence. The medium was changed every three days. Cells at passage 3-5 were used for all the experiments since we found there was increase in cellular senescence and a loss of multi-lineage differentiation potential of the PDSCs with passaging.

For the isolation of BMSCs, 3 month-old S/D female rat femora were removed and dissected free of muscle. These femora were rinsed in sterilized saline before being cut into half. The cut surface was placed facing the bottom of the centrifuge tube; then the tube was centrifuged at 800g for 15 minutes. The bone debris was removed and the bone marrow tissues were washed with PBS. The mononuclear cells were isolated by gradient centrifugation (800g, 5 minutes) and re-suspended in a culture medium containing α-MEM, 10% FBS (Invitrogen corporation, Carlsbad, CA, US). These mononuclear cells were plated at a cell density of $10^5$ cells /$cm^2$ for the isolation of stem cells and cultured in a humidified atmosphere at 37°C, 5% $CO_2$ to form colonies. On day 7 after the initial plating, the dishes were washed twice with PBS to remove non-adherent cells. At day 14, they were trypsinized and mixed together as passage 0 (P0). MSCs at passage 3-5 were used in the experiments.

### 3.2.2 Fluorescence staining for the stem cell markers

PDSCs and BMSCs were seeded on the glass slides with $1\times10^5$ density and cultured for 24 hours, making sure that the cells firmly adhered on the slides. After being blocked by 5% BCA solution for one hour, the monoclonal rabbit anti-rat primary

antibodies of CD 44, CD 90, and CD 105 (ABcam, Cambridge, MA) were incubated with the cells a concentration of 1:500 at 4ºC overnight. Washed in PBS three times, a secondary goat anti-rabbit fluorescence antibody at 1:1000 was applied on the slides for one hour. After being washed in PBS three times and stained with DAPI for 10 minutes, the stained cells and slides were mounted and subjected to fluorescence detection under a fluorescent microscope (Leica Q500MC, Leica, Germany).

### 3.2.3 Cell Proliferation Assay

PDSCs and BMSCs at passage 3-5 were plated at $4\times10^3$ cells/$cm^2$ in a 96-well plate and incubated in a 37°C, 5% $CO_2$ incubator. Cell proliferation was assessed using MTT assay (Sigma Aldrich, St. Louis, MO, USA) at days 1, 3, and 5. MTT (5mg/ml) 10ul was added into the plate hole (100ul medium) and incubated for 2-4 hours, then added 100ul SDS10% overnight to dissolve the Formaza. Absorbance at 570 nm was measured and reported. The Mg ion concentration was set as 1mM (control), 2mM, 5mM, 10 mM, and 20 mM. CGRP concentrations were $10^{-16}$M, $10^{-14}$M, $10^{-12}$M, $10^{-10}$M, and $10^{-8}$ M.

### 3.2.4 Cell migration assay

Cell migration assay was performed using Boyden's chamber, a two-chamber system in 24-well plate. The upper and lower chambers were separated by a collagen coated poroid (pore diameter was 8μm) polycarbonate membrane. Stem cells (PDSCs and BMSCs) (20000) in 200μl α-MEM containing 1% FBS were loaded into the upper well. The lower well was filled with 600 μl of $MgCl_2$ (10 mM) and CGRP ($10^{-8}$ M) in α-MEM (1% FBS). The chambers were then incubated at 37°C at 5% $CO_2$ for 24 hours. The stem cells migrated across the membrane and stuck to the underside of it.

After the incubation, the polycarbonate membrane was washed. The upper membrane was gently wiped off the cells using a cotton swab. The membrane was then cut down from the chamber, keeping the bottom of the membrane up and fixing it with 70% ethanol for 10 minutes. Then the membrane was stained with 4′,6-diamidino-2-phenylindole (DAPI), a blue-fluorescent DNA stain (excited by the violet 405 nm laser line) for nuclear probing. Cell migration was quantified by counting the stained nucleus number on the membrane's lower surface. This represented the number of migrated cells. Five visual fields (upper, lower, left, right, and middle site) were chosen for every membrane. All the cell numbers from five visual fields were counted before and after the experiments. Statistics were performed to compare the migration status of the stem cells' Mg ions and CGRP conditions. Fluorescent images were collected for visual comparison.

**3.2.5 qRT-PCR assay for osteogenic markers**

PDSCs were plated at $4\times10^3$ cells/cm$^2$ in 12-well plates and cultured in basal culture medium until the cells reached 90% confluence. This was then changed to a osteogenic medium, which was a basal complete medium (α-MEM) supplemented with 1nM dexamethasone, 50μM ascorbic acid, and 20mM b-glycerolphosphate (all from Sigma-Aldrich, St Louis, MO). Mg ion concentrations were 5mM and 10mM and CGRP concentrations were $10^{-12}$M, $10^{-10}$M, and $10^{-8}$M.

At day 14, PDSCs were harvested and homogenized for RNA extraction with RNeasy mini kit (Qiagen, Germany) in triplicate. mRNA was reverse transcribed to the cDNA by the First Strand cDNA kit (Takara, DaLian, PR, China). 2μl total cDNA from each sample were amplified in a 10μl reaction mix (384 hole plates) containing SYBR Green qPCR SuperMix-UDG and specific primers for *OPN*, *OCN*, *Runx2*, *Alp*, *Bmp2*,

*col-1*, and *b-actin* using the ABI StepOne Plus system (all from Applied Biosystems, CA, USA). Cycling condition was as follows: denaturation at 95°C for 10 minutes, 40 cycles at 95°C for 20 seconds, at an optimal annealing temperature for 30 seconds, 72°C for 30 seconds, and finally at 60–95°C with a heating rate of 0.1°C/second. The expression of the target gene was normalized to that of *b-actin* and relative gene expression was calculated using the $2^{-\Delta CT}$ formula. The mRNA expression of osteogenic markers such as *Alp*, *col-1*, *Runx2*, *Bmp2*, osteopontin (*Spp1*), and osteocalcin (*Bglap*) were assessed. (Table 3.1)

**Table 3.1 Osteogenic primer sequences and condition for qRT-PCR**

| **Gene** | **Gene name** | **Primer nucleotide sequence** | **Product size (bp)** | **Annealing temperature** |
|---|---|---|---|---|
| β-actin | *β-actin* | 5'-ATCGTGGGCCGCCCTAGGCA-3' (Forward)<br>5'-TGGCCTTAGGGTTCAGAGGGG-3' (Reverse) | 243 bp | 52 °C |
| Collagen 1A2 | *Col1A2* | 5'-CATCGGTGGTACTAAC-3' (Forward)<br>5'-CTGGATCATATTGCACA-3' (Reverse) | 238 bp | 50 °C |
| ALP | *ALP* | 5'-TCCGTGGGTCGGATTCCT-3' (Forward)<br>5'-GCCGGCCCAAGAGAGAA-3' (Reverse) | 85 bp | 58 °C |
| Collagen 2 A 1 | *COL2A1* | 5'-ATGACAATCTGGCTCCCAACACTGC-3'(forward)<br>5'-GACCGGCCCTATGTCCACACCGAAT-3' (reverse)<br><br>5'-CCGGACTGTGAGGTTAGGAT-3' (Forward) *<br>5'-AACCCAAAGGACCCAAATAC-3' (Reverse) * | 364 bp<br><br>101 bp | 55 °C<br><br>58 °C |
| Runx2 | *Runx2* | 5'-CCGATGGGACCGTGGTT-3' (Forward)<br>5'-CAGCAGAGGCATTTCGTAGCT-3' (Reverse) | 74 bp | 60 °C |
| BMP-2 | *BMP-2* | 5'-TAGTGACTTTTGGCCACGACG-3' | 81 bp | 58 °C |

| | | | | |
|---|---|---|---|---|
| | | (Forward)<br>5'-GCTTCCGCTGTTTGTGTTTG-3'<br>(Reverse) | | |
| Osteopontin | *Spp1* | 5'-<br>TCCAAGGAGTATAAGCAGCGGGCCA-<br>3' (Forward)<br>5'-<br>CTCTTAGGGTCTAGGACTAGCTTCT-<br>3' (Reverse) | 199 bp | 55 $^{o}$C |
| Osteocalcin | *Bglap* | 5'-GAGCTGCCCTGCACTGGGTG-3'<br>(Forward)<br>5'-TGGCCCCAGACCTCTTCCCG-3'<br>(Reverse) | 263 bp | 60 $^{o}$C |

### 3.2.6 Alizarin red and ALP staining assay

BMSCs were plated at $4\times10^3$ cells/cm$^2$ in a 12-well plate and cultured in basal complete culture medium until the cells reached 90% confluence. We then incubated BMSCs in osteogenic medium, a basal complete medium (α-MEM), supplemented with 1nM dexamethasone, 50μM ascorbic acid, and 20mM b-glycerolphosphate (all from Sigma-Aldrich, St Louis, MO). At day 14, these cells were washed with PBS and fixed with 70% ethanol; 15 minutes later, the ethanol was aspired and stained with 0.5% Alizarin red (pH 4.1, Sigma, St. Louis, MO). Thirty minutes later, the plate was washed with distill water three times and dried in the warm room. Then, we used HP Scanjet G3110 Photo Scanner to get photos of the stained 12-well plate.

For ALP staining, at day 14, the BMSCs were washed with PBS and fixed with 70% ethanol; after 15 min, an ALP reaction solution (3% sodiumβ-glycerophosphate 5ml, 2% $MgSO_4$ 1ml, 2% $CaCl_2$ 10ml, 2% pentobarbital sodium and ddH2O 10ml) was injected into the wells at 1ml/well, and we incubated the well overnight in a 37 °C warm room. Then we aspired the ALP reaction solution and washed it with distill water three times, dropped in 1 ml 2.6% cobalt chloride, and allowed the reaction to continue for 30 minutes. Then this was washed with distilled water three times and 1% ammonium sulfide color was dropped into it. We used the HP Scanjet G3110 Photo

Scanner to get the photos of the stained 12-well plate.

### 3.2.7 Colony forming and osteogenic differentiating ability of PDSCs at passage 1

PDSCs were isolated from the femoral periosteum of a normal rat (without implantation), a rat with an implanted needle, and a rat with an Mg pin implanted. All the rats were 3 month old S/D females. The needle and Mg pin implantation period was 2 weeks, as before. The isolated PDSCs were grouped into three the categories of normal, needle, and Mg. For colony formation assay, all the PDSCs at the P1 stage were seeded on to six well-plates with 100 cells per well and cultured for 10 days. Then, 2ml crystal violet (1%, *w/v*) was used to stain the cell colony, which was scanned with the HP Scanjet G3110 Photo Scanner. For PDSCs' osteogenic differentiation assay, PDSCs from all three groups at the P1 stage were seeded on to six-well plates with 20,000 cells per well. After the cells grew confluent, we changed to an osteogenic medium (1nM dexamethasone, 50μM ascorbic acid, and 20mM b-glycerolphosphate) and incubated them for 21 days (adding a fresh medium exchange every 3 days), after which Alizarin red staining was carried out as described above.

### 3.2.8 qRT-PCR assay for adipogenic markers

The PDSCs were plated at $4\times10^3$ cells/cm$^2$ in a 12-well plate and cultured in a basal complete culture medium until the cells reached 90% confluence. They were then incubated in an adipogenic medium, a basal complete medium (α-MEM) supplemented with 500nM dexamethasone, 0.5mM isobutylmethylxanthine, 50μM indomethacin, and 10μg/ml insulin (all from Sigma-Aldrich, St Louis, MO). At day 14, the mRNA expression of the adipogenic markers (*C/EBPα* and *PPARγ2* ) of PDSCs were assessed with qRT-PCR. The resulting Mg ion concentrations were

5mM and 10mM. Below are the parameters used in the experiment. (Table 3.2)

**Table 3.2 Adipogenic primer sequences and condition for qRT-PCR**

| **Gene** | **Gene name** | **Primer nucleotide sequence** | **Product size (bp)** | **Annealing temperature** |
|---|---|---|---|---|
| C/EBP α | *C/EBPα* | 5'-AAGGCCAAGAAGTCGGTGGA-3' (Forward) CAGTTCGCGGCTCAGCTGTT-3' (Reverse) | 189 bp | 55$^{o}$C |
| PPARγ2 | *PPARγ2* | 5'-CGGCGATCTTGACAGGAAAG-3' (Forward) CTTCCACGGATCGAAACTG-3' (Reverse) | 174 bp | 59$^{o}$C |

## 3.3 Result

### 3.3.1 PDSCs were critical in periosteal osteogenesis

We characterized MSCs (PDSCs and BMSCs) by staining stem cell markers such as CD44, CD90, and CD105 in immunofluorescence imaging (Figure 3.3.1). PDSCs and BMSCs had pluripotent differentiation ability proved by further osteogenic differentiation experimentation.

PDSCs were isolated from the femur periosteum of normal (without implantation) rats, rats implanted with needles, and rats implanted with Mg pins. Stem cell colony forming and osteogenic capability were assayed (Figure 3.3.2). The results of PDCSs isolated from Mg pin implanted femur periosteum revealed significant colony forming and osteogenic differentiating ability at the P1 stage. PDSCs from the normal and needle implantation group showed a similar but far weaker colony formation and osteogenic differentiation ability. This feature of PDSCs faded away after the PDSCs passed to the second generation, indicating that PDSCs showed remarkable self-renewing and osteogenic differentiation ability after Mg was implanted. Mg directly induced new bone formation.

### 3.3.2 Effects of CGRP on MSCs' proliferation, migration, and differentiation

MSCs, including PDSCs and BMSCs used in this part of study, were all at passage 3-5. In the cell proliferation assay, the MTT results showed that CGRP had no significant effect on the proliferation of PDSCs' at concentrations from $10^{-16}$ to $10^{-10}$ M; at a concentration of $10^{-8}$ M, however, CGRP had slight but significant inhibiting effects on the PDSCs. With regard to the BMSCs, CGRP had promoting effect on cell proliferation from $10^{-16}$ to $10^{-12}$ M. The MTT results indicated that CGRP had little effect on the proliferation of PDCSs and BMSCs. (Figure 3.3.3 A, B)

Since the serum concentrations of CGRP were below 10 pM[196], concentrations of CGRP from $10^{-12}$ to $10^{-8}$ M were used to determine its osteogenic effect. In our qRT-PCR assay, CGRP significantly promoted the synthesis of *ALP* mRNA, *OCN*, and *OPN* in PDSCs at week 2 (Figure 3.3.4). The results showed that CGRP significantly enhanced ALP expression to the BMSCs and formed calcium nodules (Figure 3.3.5). Based on these results, we found CGRP at $10^{-10}$ to $10^{-8}$ M, showing its strong osteogenic effect on stem cell differentiation.

In our cell migration assay, CGRP significantly attracted the migration of BMSCs through a mesh membrane with a pore size of 8μm. However, CGRP had no effect on PDSCs' migration, indicating that new bone formation after Mg implantation might require BMSC participation (Figure 3.3.6).

### 3.3.3 Effect of Mg ions on MSCs' proliferation, migration and differentiation

The effects of Mg ions ($MgCl_2$) on PDSCs and BMSCs were evaluated by MTT assay. In our results, Mg ions dramatically suppressed PDSC and BMSC proliferation when its concentrations were above 10mM (20-50mM). Below 10mM (including 10mM), Mg ions had no obvious effect on either PDSCs or BMSCs (Figure 3.3.7 A, B), indicating that Mg ions themselves did not promote cell proliferation.

In our study, Mg ions promoted osteogenic rather than adipogenic differentiation to the PDSCs and BMSCs (Figure 3.3.8 A, B). The qRT-PCR results showed that *ALP*, *COL-1*, *OCN*, and *OPN* mRNA were all highly expressed in PDSCs cultured with $MgCl_2$ at concentrations of 8mM. *BMP-2* mRNA expression, however, was not affected by $MgCl_2$, which indicated that the effect of Mg ions' osteogenic on PDCSs may not occur through the *BMP-2* pathway. In our qRT-PCR analysis for Mg ions' adipogenic effect on PDSCs and BMSCs, neither C/EBPα nor PPARγ2 were

significantly regulated with $MgCl_2$ (5mM and 10mM) treatment. This indicated that Mg ions had no effect on stem cell adipogenic differentiation. In our alizarin red and ALP staining assay, it was found that $MgCl_2$ also had significant osteogenic effects on BMSCs at 5 mM and 10 mM. (Figure 3.3.9 A, B)

In the cell migration assay, Mg ions significantly attracted the migration of BMSCs through the mesh membrane with a pore size of 8μm. However, Mg ions had no effect on the PDSCs' migration. (Figure 3.3.10)

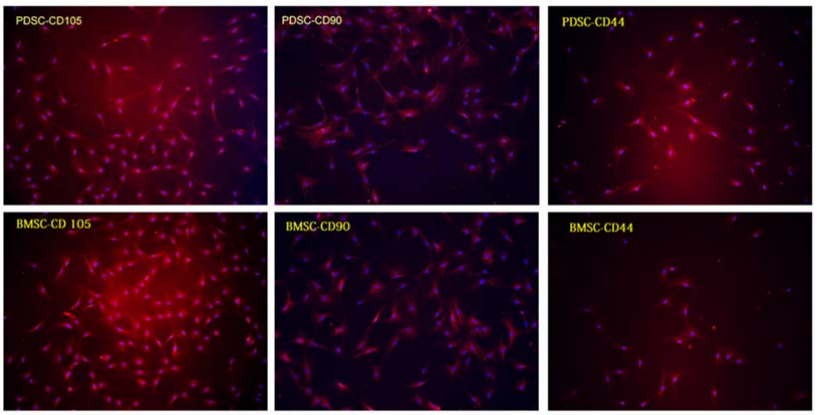


**Figure 3.3.1.** Immunofluorescence staining of stem cell markers: CD44, CD90, and CD105 for PDSCs (above) and BMSCs (below), 400×. Red colors were markers and blue colors were DAPI stained nucleus. The majority of marker-stained cells were pluripotent stem cells.

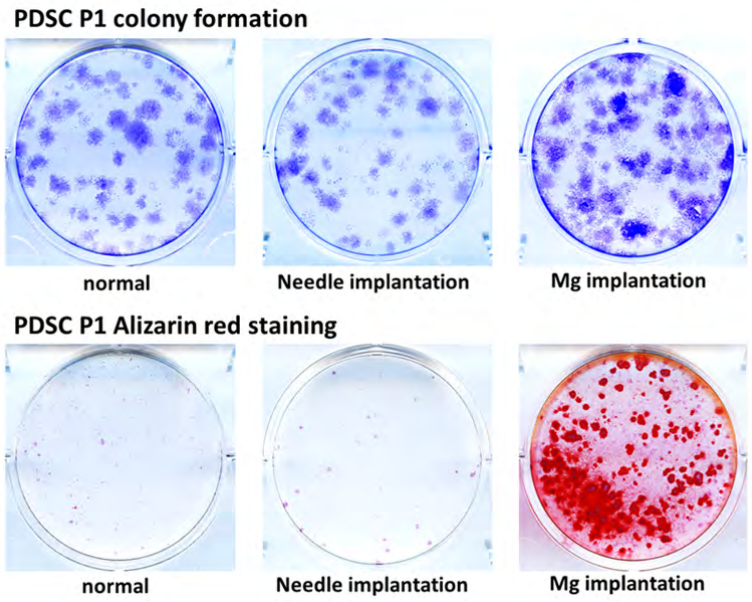


**Figure 3.3.2.** Colony formation (above, crystal violet staining) and osteogenic differentiation (below, alizarin red staining) of PDCSs (passage 1) were tested. The left picture is PDSCs from rat femur without implantation, the middle picture is from femurs with stainless needle implantation, and the right picture is from femurs with Mg implantation.

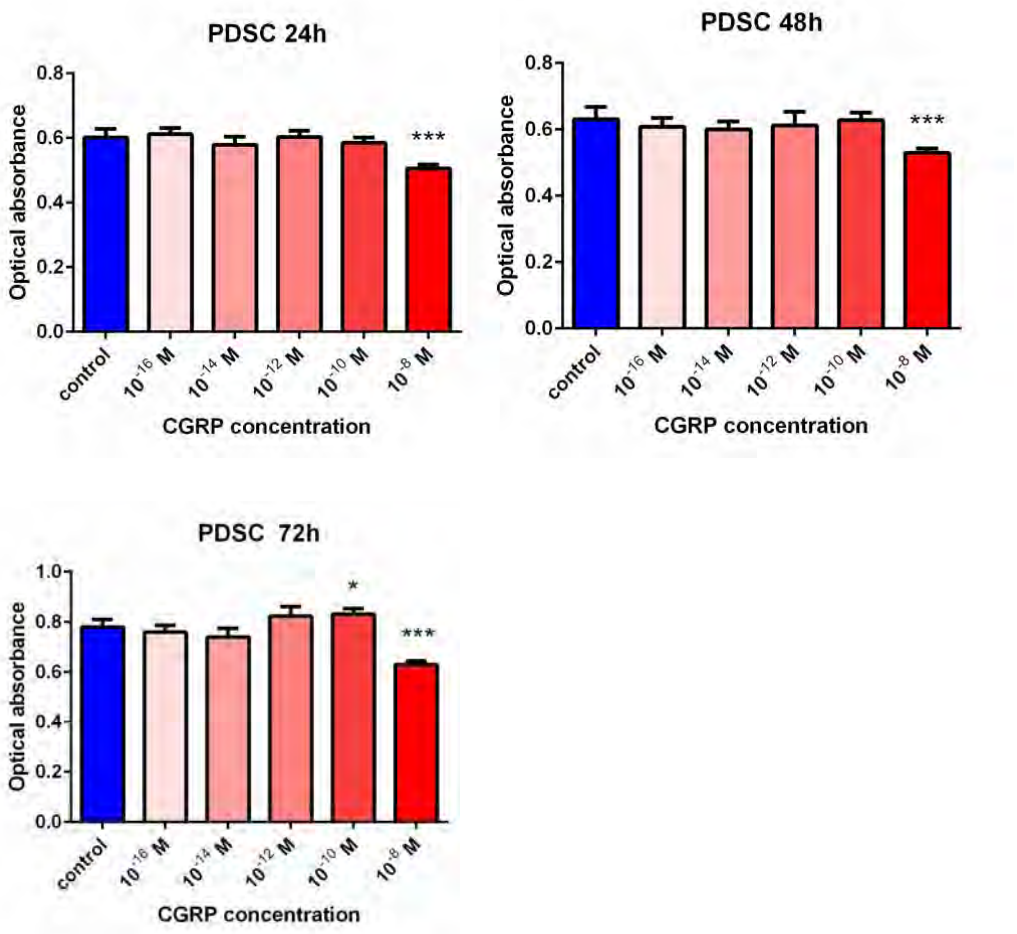


**Figure 3.3.3. A.** MTT assay for CGRP to PDSCs at three time points. All statistical data were shown as a mean of ± one standard deviation (SD). One-way ANOVA was applied to evaluate the statistical significance of the differences between each CGRP concentration and the control means (using Graphpad Prism 5.0 software). Significant differences were defined as *P<0.05, **p<0.01, and ***p< 0.001.

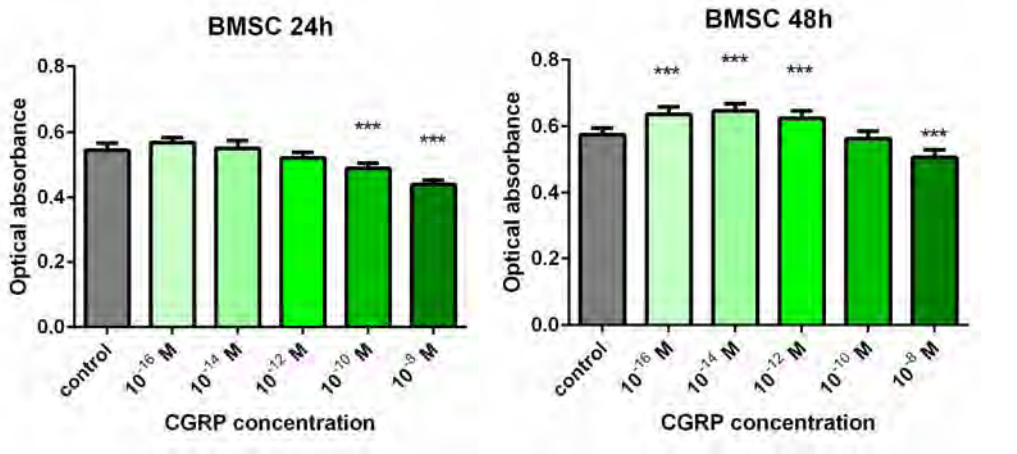

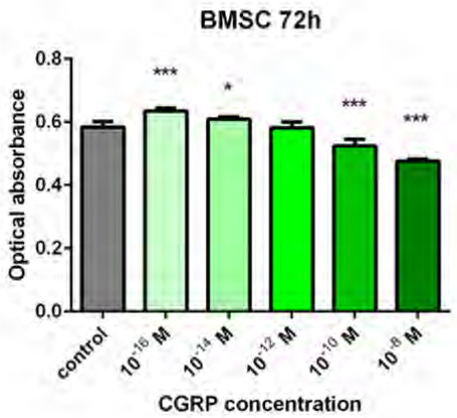


**Figure 3.3.3. B.** MTT assay for CGRP to BMSCs at three time points. All statistical data were shown as a mean ± one standard deviation (SD). A one-way ANOVA was applied to evaluate the statistical significance of the differences between each CGRP concentration and the control means (using Graphpad Prism 5.0 software). Significant differences were defined as *:$p<0.05$, **$p<0.01$, and ***$p< 0.001$.

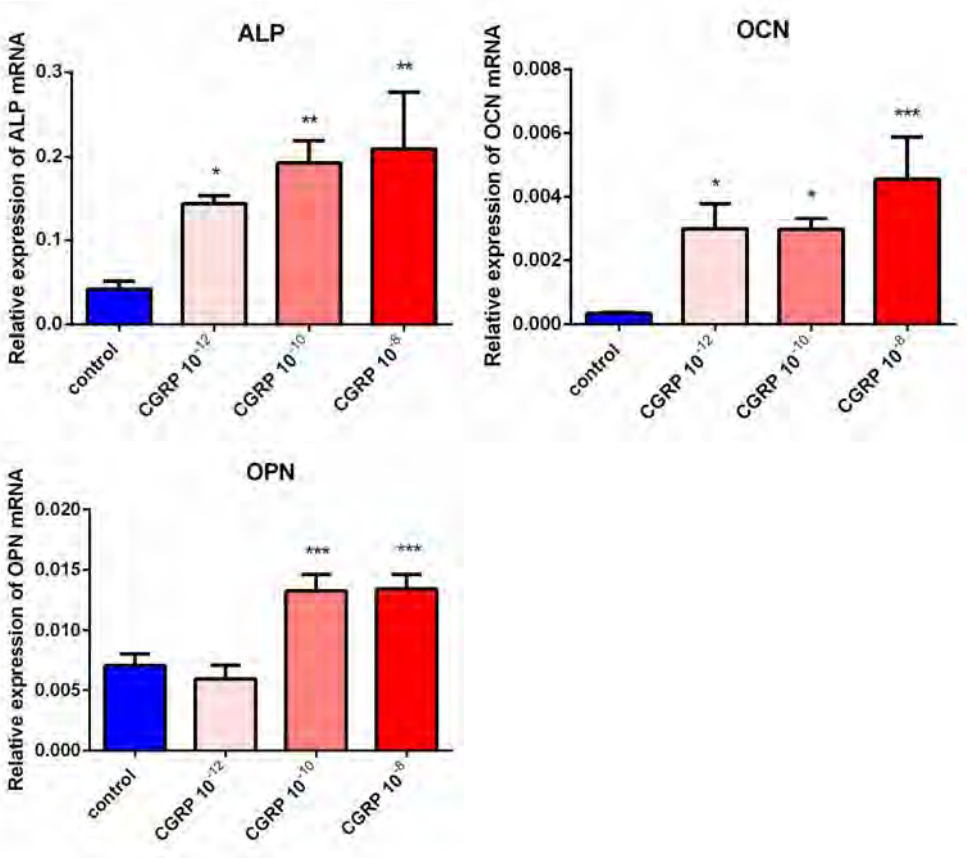


**Figure 3.3.4.** qRT-PCR results of PDSCs incubated with CGRP at week 2. ALP, OCN, and OPN mRNA expression under CGRP treatment (from $10^{-12}$ to $10^{-8}$ M) were all significantly up regulated. ALP expression increased 3 to 4 times higher than the

control when CGRP increased to $10^{-8}$ M. OCN expression was highly regulated to almost 10 times the control when CGRP was at 10-8 M. OPN expression was also highly up-regulated after CGRP treatment in $10^{-12}$ and $10^{-8}$ M concentrations. All statistical data were shown as the mean ± one standard deviation (SD). A Paired Student's t-test was applied to evaluate the statistical significance of the differences between each CGRP concentration and the control means (using Graphpad Prism 5.0 software). Significant differences were defined as *P<0.05, and **p<0.01, and ***p< 0.001.

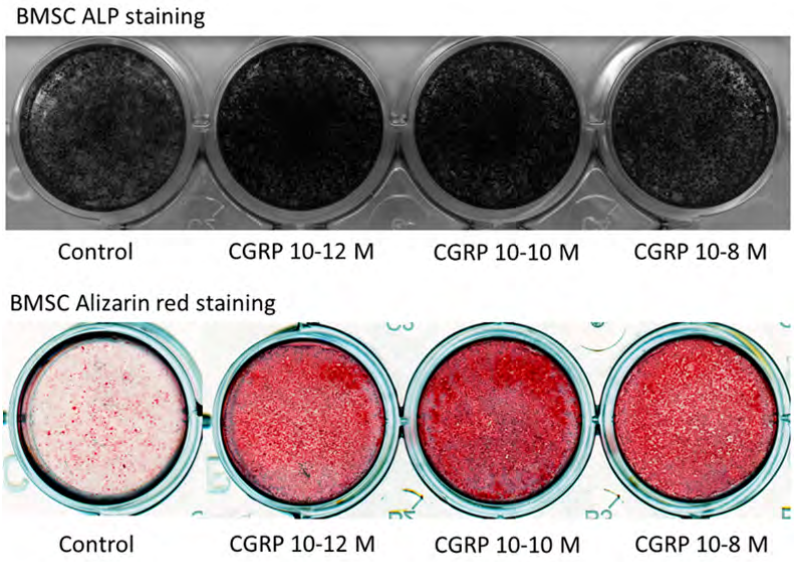


**Figure 3.3.5.** Osteogenic effect of CGRP on BMSCs assayed by ALP staining (above) and alizarin red staining (below) at week 2. CGRP concentration was from $10^{-12}$ to $10^{-8}$ M.

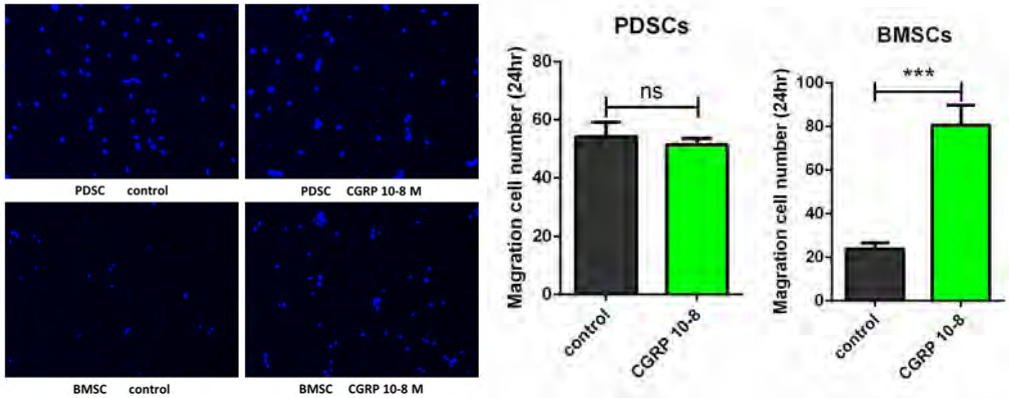

**Figure 3.3.6.** Cell migration assay for CGRP's effect on the migration of both PDSCs and BMSCs in 24 hours. Blue spots represent the DAPI stained cell nucleus. A student's t-test was performed between the control and CGRP treated group. Significant differences were defined as *P<0.05, **p<0.01, ***p< 0.001, and p>0.05.

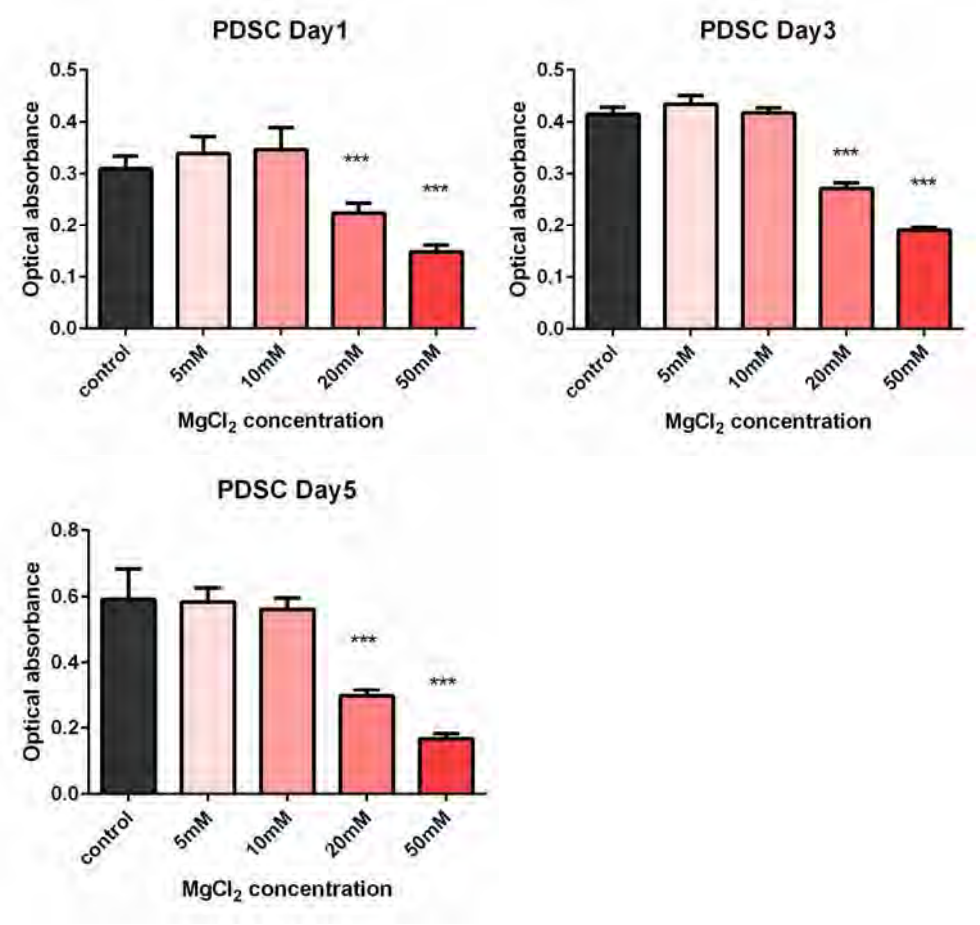


**Figure 3.3.7. A.** MTT assay for $MgCl_2$ to PDSCs at three time points. All statistical data were showed as the mean ± one standard deviation (SD). A one-way ANOVA was applied to evaluate the statistical significance of the differences between each CGRP concentration and the control means (using Graphpad Prism 5.0 software). Significant differences were defined as *P<0.05, **p<0.01, and ***p< 0.001.

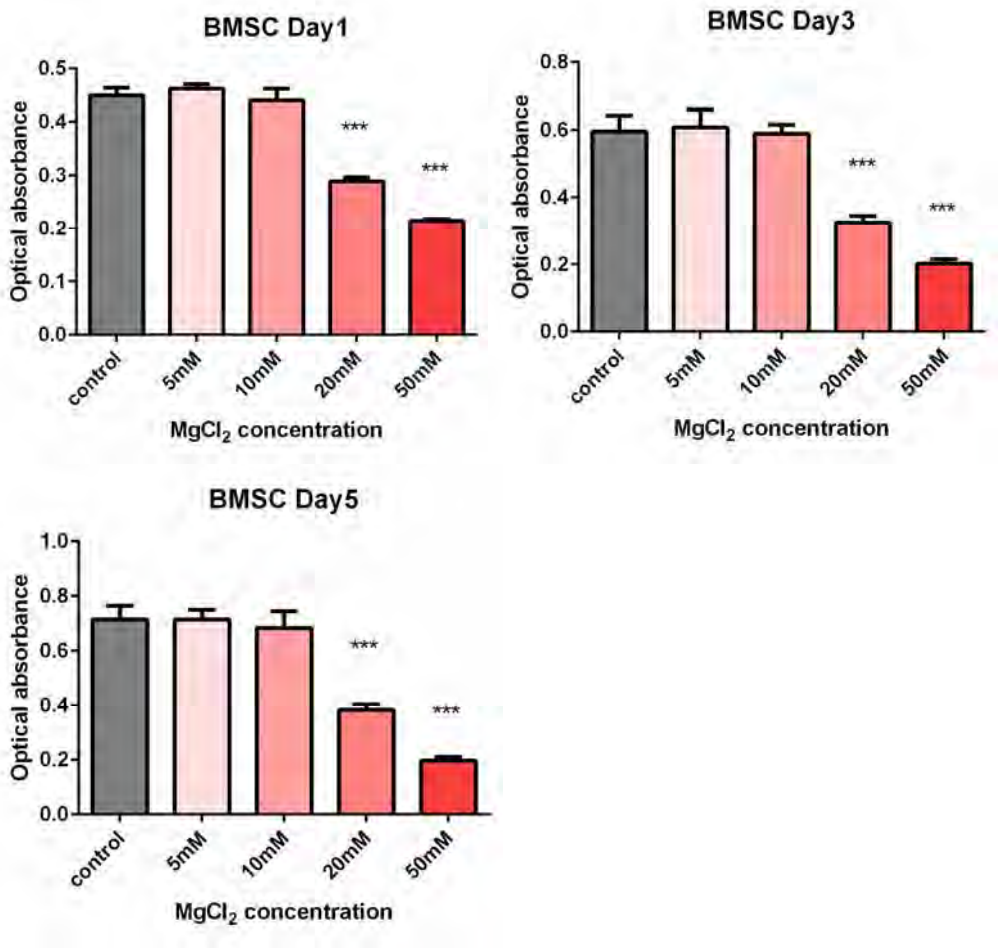


**Figure 3.3.7. B.** MTT assay for $MgCl_2$ to BMSCs at three time points. All statistical data were shown as the mean ± one standard deviation (SD). One-way ANOVA was applied to evaluate the statistical significance of the differences between each CGRP concentration and control means (using Graphpad Prism 5.0 software). Significant differences were defined as: *P<0.05 and **p<0.01 and ***p< 0.001.)

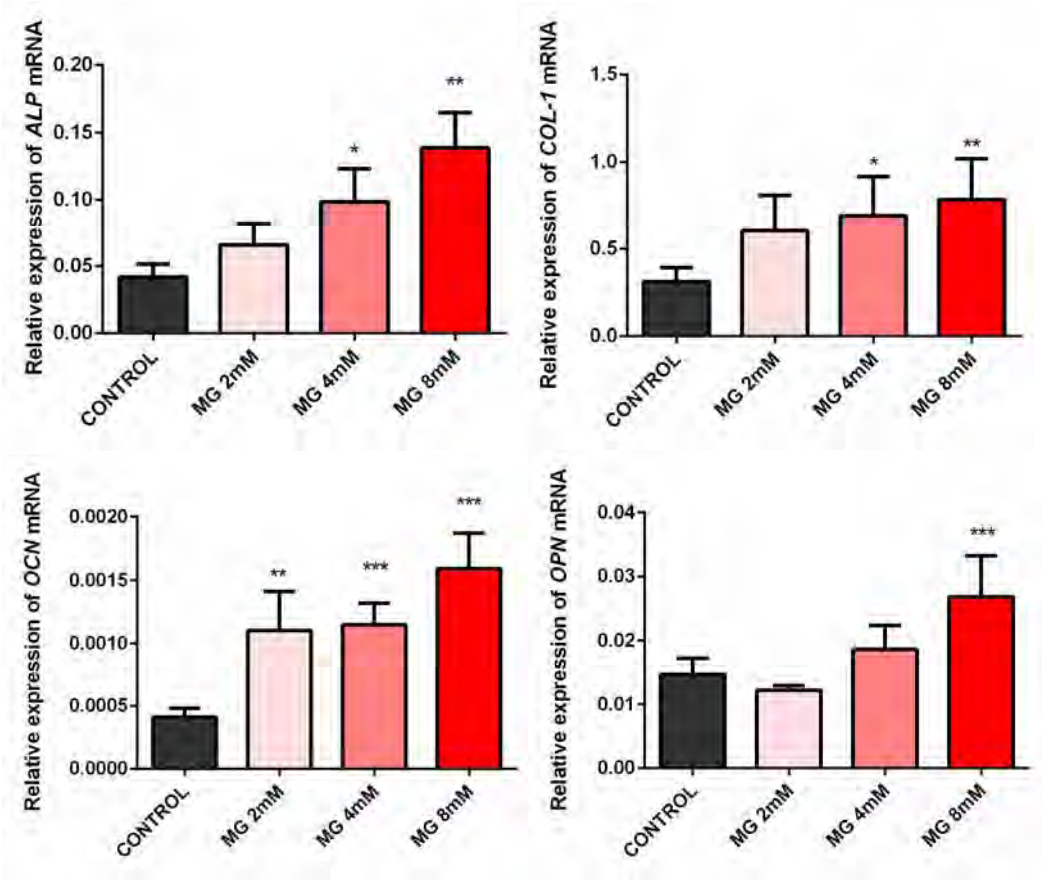


**Figure 3.3.8.A.** qRT-PCR osteogenic results of PDSCs incubated with $MgCl_2$ at week 2. ALP, COL-1, OCN, and OPN mRNA expression under $MgCl_2$ treatment (from 2 to 8 mM) were all significantly up regulated. All statistical data were shown as the mean ± one standard deviation (SD). A Paired Student's t-test was applied to evaluate the statistical significance of the differences between each $MgCl_2$ concentration and the control means (using Graphpad Prism 5.0 software). Significant differences were defined as *P<0.05, and **p<0.01, and ***p< 0.001)

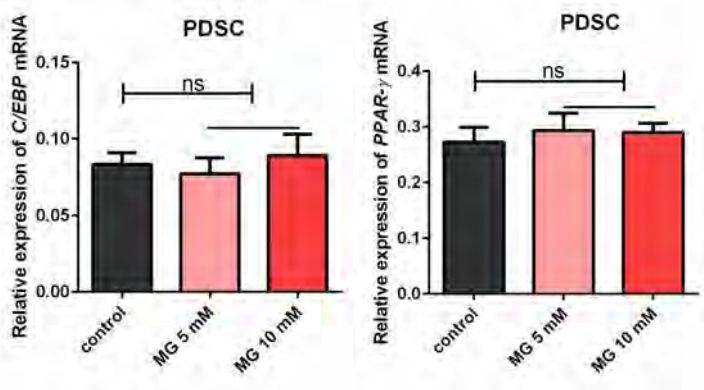


**Figure 3.3.8.B.** qRT-PCR adipogenic results of PDSCs incubated with $MgCl_2$ at

week2. C/EBPα and PPARγ2 mRNA expression under $MgCl_2$ treatment (from 5 to 10 mM) were not affected. All statistical data were shown as the mean ± one standard deviation (SD). A one-way ANOVA was applied to evaluate the statistical significance of the differences between each $MgCl_2$ concentration and the control means (using Graphpad Prism 5.0 software). Significant differences were defined as ns: P>0.05.

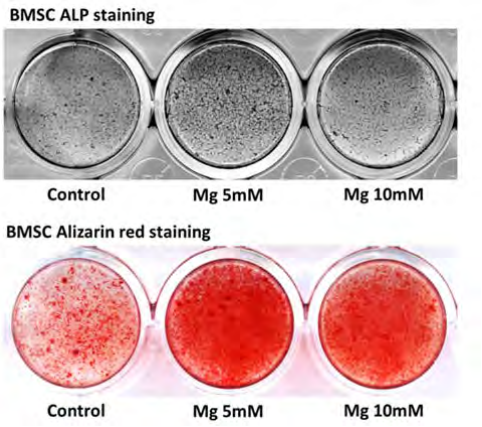


**Figure 3.3.9.A.** Osteogenic effect of Mg ions on BMSCs assayed by ALP staining (above) and alizarin red staining (below) at week 2. $MgCl_2$ concentration was from 5 to 10 mM.

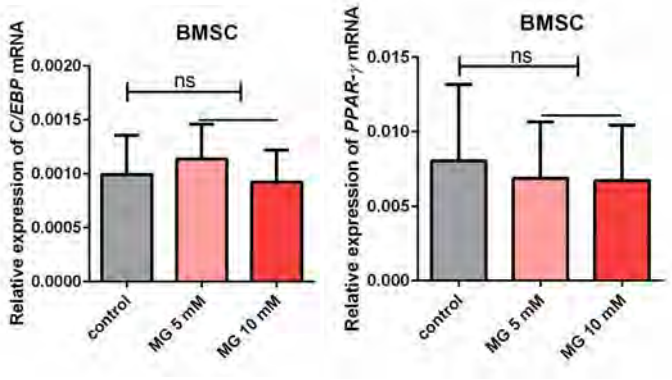


**Figure 3.3.9.B.** qRT-PCR adipogenic results of BMSCs incubated with $MgCl_2$ at week2. C/EBPα and PPARγ2 mRNA expression under $MgCl_2$ treatment (from 5 to 10 mM) were not affected. All statistical data were shown as the mean ± one standard deviation (SD). A one-way ANOVA was applied to evaluate the statistical significance of the differences between each $MgCl_2$ concentration and the control means (using Graphpad Prism 5.0 software). Significant differences were defined as ns: P>0.05.

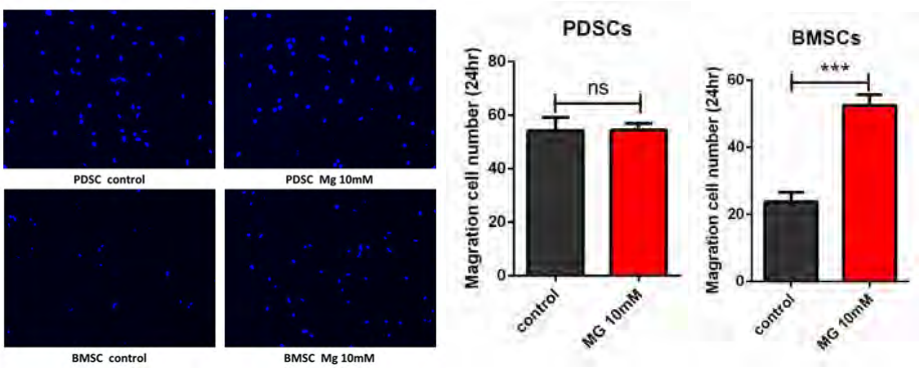


**Figure 3.3.10.** Cell migration assay for Mg ions' effect both on migration of PDSCs and BMSCs in 24 hours. Blue spots were DAPI stained cell nucleus. Student's t-test was performed between control and $MgCl_2$ treated group. Significant differences were defined as *P<0.05 and **p<0.01 and ***p< 0.001. ns:p>0.05.

## 3.4 Discussion

### PDSCs and BMSCs

PDSCs were derived from periosteum. It generally belongs to MSCs, which can be isolated from various mesenchymal tissues such as bone marrow, periosteum, tendons, synovium, skeletal muscle and adipose tissue[197,198]. MSCs were assumed to have similar features: they are self-renewing, multi-directional in differentiation, and immuno-privileged[199]. However, there were differences in every aspect of the cell behaviors, from proliferation to differentiation. For example, among many MSCs, a synovium derived stem cells possessed the strongest self-renewal ability; bone marrow and periosteum-derived stem cells had similar but less self-renewal ability; and muscle derived stem cells along with adipose derived stem cells had the lowest self-renewal ability[197]. In terms of multi-directional differentiation behavior, synovium derived stem cells possessed the best ability in all the chondrogenesis, osteogenesis, and adipogenesis processes[197]. Bone marrow and periosteum stem cells, meanwhile, behaved with less ability than synovium derived stem cells. Muscle and adipose derived stem cells had the worse three-phase differentiation behavior. However, the latter had a significant ability in adipogenesis, just as synovium derived stem cells[197]. The results indicated that MSCs from different tissue had discriminating behavior in cell proliferation and differentiation.

For the isolation of PDSCs and BMSCs, we used stem cell commonly expressed epitope markers. There are many types of cell markers, including CD34, CD45, CD79, CD19, and CD117, which were positive for hematopoietic cells, as well as CD31 and VEGFR2, which were positive for endothelial cells. Stem cell positive markers—including CD10, CD54 (intercellular adhesion molecule 1), CD166 (activated leukocyte cell adhesion molecule), CD106, CD147 (neuroregulin), NGFR, STRO-1

(vascular cell adhesion molecule 1), CD44, CD90, and CD105—were all characteristic stem cell surface markers[200-202]. The epitope profile of the MSCs was determined by their own cell behaviors, including self-renewing, multi-potent behaviors as well as the stem cell markers described above. Here, we chose three stem cell positive surface markers (CD44, CD90, and CD105) to ensure that the rat femur cells we isolated were in fact stem cells. These three kinds of markers were highly expressed (70%-100%) in all tissue derived MSCs[197]. In our study, the majority of MSCs isolated from rat femur periosteum and bone marrow were expressed with CD44, CD90, and CD105. We considered the cells derived from periosteum and bone marrow to be PDSCs and BMSCs, respectively. (Figure 3.3.1)

**Neuropeptide CGRP's osteogenic effect on MSCs**

CGRP was a 37 amino acid peptide encoded by gene *Calca* that expressed a bone metabolism peptide calcitonin different from the calcitonin that underwent mRNA splicing and proteolytic processing in the C cells at the thyroid. CGRP was produced by alternatively splicing in neurons at the central and peripheral nervous system[203-205]. CGRP has been implicated in many physiologic processes, such as peripheral vasodilation, cardiac acceleration, perception of temperature, and itching[206,207]. Moreover, CGRP was found to be an osteoanabolic factor by stimulating cyclic adenosine monophosphate (cAMP) production in osteoblast and inhibiting osteoblast apoptosis with β-catenin stabilization[208-210]. In Wang Liping's study, mouse BMSCs, osteoblasts, and osteoclasts were all treated with CGRP with concentration of $10^{-14}$ to$10^{-8}$ M. Cell proliferation, osteogenic differentiation and TRAP staining were evaluated. Liping's research found that CGRP with concentration of $10^{-10}$ to $10^{-8}$ M significantly promoted proliferation (about 36%) and up-regulated osteoblastic gene expression in BMSCs. It also inhibited NF-κB ligand (RANKL) activation of NF-κB

in osteoclasts, down-regulated osteoclastic genes like TRAP and cathepsin K, and decreased the number of $TRAP^+$ cells[211]. However, there has been no study to evaluate the effect on CGRPs on PDSCs.

Since we knew that MSCs of different tissue origin had distinct cell behaviors, including proliferation, cell migration, and differentiation, our results showed that CGRP probably affected PDSCs and BMSCs in different ways. CGRP had no proliferate promoting effect on PDSCs within 72 hours, even though its concentration increased to $10^{-10}$ M, while at a high concentration of $10^{-8}$ M, CGRP had a slight inhibitory effect on PDCS proliferation. CGRP had significant promoting effect on BMSC proliferation at concentrations below $10^{-10}$ M. This result contradicted Wang LP's findings, which indicated that only CGRP with $10^{-10}$ M promoted mouse BMSC proliferation (about 36%)[211]. Our result was based on rat MSC and MTT assay; in Wang's study, mouse BMSCs and BrdU incorporation assay were used, and that is the probable cause of the difference in our results. In our study, CGRP at high concentrations ($10^{-8}$ M) were considered to have suppressive effects on the proliferation of PDSCs and BMSCs. This slight suppressive effect on stem cell proliferation has not been previously discussed. We hypothesized that it might be due to CGRP's strong osteogenic effect at a $10^{-8}$ M concentration and we knew that the stem cell differentiation process was closely related to cell cytoskeletal motor reformation and motions. Stem cells could feel the elasticity of the substrate they anchored on: the soft matrix mimic brain was neurogenic, the stiffer muscle-like matrix was myogenic, and the comparatively rigid substrate was osteogenic[212]. After inhibiting non-muscle myosin II in native MSCs, their elasticity-directed lineage specificity was blocked without strongly disturbing the other aspects of cell shape and function[212-214].

Since focal adhesion and migration provided the MSCs with the necessary force through transmitting pathways for us to perceive the microenvironment through actin-myosin contractions, we used migration assay to assess CGRP's reprogramming effect on stem cells. CGRP's concentration in the cell migration assay was $10^{-8}$ M. At this high concentration, CGRP showed a significant promoting effect on migration in BMSCs (about 4 times that of the control) rather than PDSCs. The 8μm diameter of the mesh holes through which MSCs migrated was wide enough for both PDSCs and BMSCs to pass through, so the different responses of the two stem cells to CGRP should not have been due to the membrane of the migrating assay, but was probably due to their own reaction to CGRP. In the migration assay, we seeded 20000 cells into the upper well (the membrane area of the well was 0.25 $cm^2$), so the cell density was 80k/$cm^2$. In Eyckman's study, hPDSCs were more prone to express adipogenic or chondrogenic markers at a high seeding density (85 k/$cm^2$) than a low seeding density (5 k/$cm^2$) and hBMSCs had a more significant osteogenic effect at a high seeding density (85 k/$cm^2$) than a low seeding density (5 k/$cm^2$). They also proved that discouraged osteogenic and enhanced differentiation resulted from blocking the cytoskeletal contractility by adding Rho kinase inhibitor Y27632 in hPDSCs[215]. This finding suggested to us that the cytoskeletal contractility of PDSCs may be restricted in a high cell density condition, and its reactivity to CGRP was refrained. Alizarin red staining and ALP staining proved that CGRP had a significant osteogenic promoting effect on BMSCs at all the concentrations, from $10^{-12}$ to $10^{-10}$ to $10^{-8}$ M. CGRP's osteogenic effect was most prominent in concentrations of $10^{-10}$ M. This result was consistent with the findings by Wang LP[211]. With regard to PDSCs, CGRP also had an osteogenic promoting effect, as well as BMSCs. It was noted that CGRP enhanced ALP, OCN, and OPN mRNA expression in PDSCs with dose dependent performance.

The most remarkable osteogenic effect was at concentrations of $10^{-8}$ M. It was interesting that sensory nerve fibers were densely distributed in periosteum and that CGRP was highly expressed in the newly formed cortical bone around the periosteum site after Mg implantation. Therefore, we deduced that BMSCs were probably attracted away from bone marrow to the peripheral region of the cortical bone by CGRP and differentiated into osteoblasts to form new bone.

**Mg ion's osteogenic effect on MSCs**

With regard to Mg ions' effect on PDSCs and BMSCs, our results showed that Mg ions had no effect on cell proliferation in two stem cells over 3 days. At high concentrations of 20 and 50mM, Mg ions significantly suppressed the stem cells' proliferation and viability. In the cell migration assay, Mg ions (10mM) significantly enhanced BMSCs' migration (more than two times that of the control) and had no effect on PDSCs. The results indicated that Mg ions had no effect on stem cell self-renewal, but they had a direct effect on stem cell migration, probably through activating the stem cell's cytoskeletal motors arrangements and adhesive related molecular dynamics. The Mg ion combined with CGRP did not show significant synergistic effect on BMSCs' migration behavior. This indicated that the mechanism for the migration promoting effects of CGRP and Mg ions on BMSCs might be distinct. Mg ion's direct effect on BMSC migration also predicted that it may show some effect on reprogramming in stem cells. Actually, our results proved that Mg ions significantly promoted osteogenic differentiation by enhancing almost all the osteomarkers expression in PDSCs, including ALP, OCN, OPN, and COL-1, except for BMP-2. We chose 2mM, 4mM, and 8mM for Mg ion concentrations to prevent the Mg ion's cell viability inhibiting effect under high concentrations (above 10mM).

The previous studies also found Mg's direct effect on MSCs proliferation, growth and

differentiation; some of them confirmed cytotoxicity under high Mg ion concentrations, but most of them concerned the stem cells' performance on the Mg metal surface[216-218]. It was concluded that the high pH condition caused by Mg degradation had no significant harmful effects on stem cell growth and proliferation. However, cell adhesion behavior and osteoblast activities were enhanced in the Mg implant surface or Mg treated material. Nonetheless, most of them did not treat the cells directly with Mg ions. Rather, they concerned mostly the materials' biological performance and not the direct effect of Mg ions on bone cells. In Nguyen, TY's study, it was found that human embryonic stem cells (hESCs) retained pluripotency by the expression of OCT4, SSEA3, and SOX2 in all tested Mg ion dosages, from 0.4 mM to 4 mM[216]. In our study, Mg ions with concentrations ranging from 5 mM to 10 mM already had significant osteogenic effects on BMSCs. The difference may be due to the different cell lines used. We also found that Mg ions had no effect on stem cells' adipogenic differentiation either with PDSCs or BMSCs. This result raised a very interesting question: Why did Mg ions specially promote stem cells differentiation in the osteogenic direction but not the adipogenic direction? Did this phenomenon closely correlated with Mg influx through the intracellular transmembrane ion channel? This question formed the foundation for our work described in next chapter.

**Conclusion**

From the results of this part of study, we concluded that the neuropeptide CGRP had a significant osteogenic effect on both PDSCs and BMSCs, proving our hypothesis that CGRP release after Mg implantation played a pivotal role in new bone formation. Mg's osteogenic effect was mainly controlled by its neural activity. Meanwhile, we also found that the Mg ion itself promoted MSCs' differentiation in the osteogenic direction.

# **Chapter** 4

## Effect of Mg ions
on
## DRG neuron
and
## Cell membrane Mg ion channels
***In vitro***

## 4.1 Introduction

From the study described in chapter 3, we proved that neuropeptides (such as CGRP) were dedicated to new bone formation by directly promoting osteogenic differentiation in PDSCs and BMSCs. How, though, did the Mg ions affect neurons *in vitro*? That was the question we try to explicitly answer in this chapter. As the release of neuropeptides from presynaptic membranes engaged exo-endocytosis processes, the transmission of synaptic vesicles to the axonal terminal would likely be key. Although evidence for the hypothesis of synaptic vesicles transmission in the nerve ending still had not been established by a well-accepted model, it was clear that synaptic vesicles exocytosis and endocytosis occurred at the same time when the neuron got stimulated. There was an exo–endo cycling pool of vesicles and a reserve pool of vesicles in the axon terminal. When stimulation was applied to the neuron, the synaptic vesicles would be released from the exo–endo cycling pool; meanwhile, other vesicles were endocytosed during stimulation and flew into the reserve pool.

The purpose of our study was to determine whether synaptic vesicles containing neuropeptides (CGRP) would be accumulated in the axon terminal after Mg treatment in the neuron. Since the sensory nerve endings of the femur periosteum were axon terminals extended from the lumber 3-5 level DRG neuron, we explored this question with a single DRG neuron reacting assay *in vitro*. After using florescent dye FM1-43, which can be encapsulated in synaptic vesicles, the synaptic vesicles could be observed as numerous green spots in the neuron body under fluorescent microscopy, and their formation and transmission in a single DRG neuron could be pictured in a live recording. We observed the remarkable stimulation of Mg ions resulting in the synaptic vesicles replenishing (synaptic elasticity) in the axon terminal of the DRG neuron. That was the basic precondition for the mass release of the neuropeptide CGRP under Mg implantation.

As to whether the mechanism of Mg ions directly promoted the stem cell's osteogenic differentiation, we confirmed that Mg ions entered into the cytoplasm first. Then, we ascertained that the Mg channel mainly charged cellular Mg ion influx. There have been several Mg ion channels on the cell membrane reported to prefer Mg flux, including TRPM6 7 and MagT1 in eukaryocytes[219]. TRPM6 was mainly expressed at the epithelia cells of kidney, colon, and lung tissue. TRPM7 was synthesized ubiquitously in all the tissue. It had the homologue structure of, and functioned synergistically with, TRPM6 and TRPM6. So, TRPM 6 and 7 may be principally involved in the Mg ions' resorption and reabsorption at the kidney and colon epithelia. The MagT1 channel has been reported as an important Mg ion channel at the eukaryocyte membrane, but a study of its physiological function and property has been lacking. We postulated that one channel might be the critical ion channel in Mg ions' influx in MSCs.

To explore Mg ion influx into MSCs and DRG neurons, we used an epifluorescence microscope to get a real time recording of Mg ion flux. We used a florescent dye—Mg-Fura-2—to stain the Mg ions, and several cells were monitored under the epifluorescence microscope to record the Mg ion accumulation in the stem cell cytoplasm. We found that the MagT1 channel was mainly responsible for cell Mg influx, which could be blocked by its nitrodipine in the MSCs and DRG neuron.

## 4.2 Materials & Methods

### 4.2.1 DRG neuron isolation and culture

Before our DRG dissection and isolation, culture dishes were coated with laminin (Life Technologies) and Poly-D-lysine hydrobromide (Life Technologies). Six well plates containing round glass slices with a diameter of 2.5cm were soaked in PBS with laminin (20ng/ml) and Poly-D-lysine hydrobromide (50ng/ml) for 4 hours in a $37^{o}$ C incubator for standby application.

Outbred 6–8 week old female SD rats (weighing 100 to 150 grams) were used in this study. The dissociated primary sensory neurons were approved by CUHK's animal research ethics committee (Ref. No. 13/003/MIS-5) (Appendix I). The procedures for the isolation of the dorsal root ganglia neurons had been established by other researchers and are described in chapter 2. Rar lumber 3-5 level dorsal root ganglia were separated and transferred to 10 ml PBS with 10% PNS and without Ca++/Mg++ placed in a tube on ice. The PBS were carefully removed without disturbing the DRG and incubated in papain solution for 10 min in a $37^{o}$ C water bath. The tube was spun for 1 minute at a low speed (less than 200g) to pellet the ganglia and the papain solution was carefully removed. Type I collagenase (1mg/ml) solution was put into collection tube and the tube was gently flicked to stir the ganglia, which were incubated for 60 minutes in a $37^{o}$ C water bath. The tube was then spun for 1 min at a low speed (400g) to pellet the ganglia, which were carefully removed from the collagenase solution. A 0.25% trypsin solution was transferred into the tube and incubated in a $37^{o}$ C water bath for 30 minutes. We then blew the tissue to fragment it and transferred the digested medium through a filter with a mesh size of 45μm, spun the tube for 5 minutes at a high speed (800g), and carefully removed the trypsin solution. The isolated neurons were incubated in F12 medium with 10% FBS, 1%

penicillin/streptomycin, a neural growth factor (NGF) (20ng/ml), 5-fluorodeoxyuridine ($10^{-5}$M), and uridine ($10^{-5}$M) (Sigma. USA). 100 µl of DRG neuron suspension (approximately 5000–10000 cells) was added into each of 6 well plates containing glass slides coated with laminin and Poly-D-Lysin. After the DRG neuron was attached to the glass slides for 4 hours of incubation, the medium above was aspired and changed to a fresh F12 medium with 10% FBS, 1% penicillin/streptomycin, 20ng/ml NGF, $10^{-5}$ M fluorodeoxyuridine, and $10^{-5}$ M uridine. We then incubated it for 72 hours and let the DRG neuron grow.

### 4.2.2 Synaptic replasticity under Mg treatment

DRG neurons were seeded on 25 mm diameter glass coverslips in 6 well-plates for 1 week with F12 medium. The medium was not changed during the incubation period. After the DRG neuron grew steady and functioned normally, we used fluorescent dye FM1-43 (N-(3-triethylammoniumpropyl)-4-(4-(dibutylamino)styryl) pyridinium dibromide) (Biotium, Inc. Hayward, CA 94545, USA) to stain the synaptic vesicles in the neuron body.

FM dyes are a series of fluorescent molecules widely used to detect cell vesicle fusion trafficking and exocytosis endocytosis in various systems. FM1-43 and its derivatives were styryl dyes that harbor a cation charged water-soluble polar head group and a lipid-soluble hydrophobic tail. Between its head and tail was a central region that determined their fluorescent properties. FM1–43 was basically not a fluorescent, as it is in an aqueous soluble group. However, this increased its quantum yield more than 40-fold when its lipid soluble group bounded to liposomes, just as with the membrane of synaptic vesicles. The lipid-soluble tail of the FM dyes bound to the outer membrane leaflet of the neural axonal ending and was encapsuled into synaptic

vesicles during endocytosis. This membrane enrolling association was reversible. The dye could be used to study vesicles formation, fusion, and exocytosis. We applied FM1–43 to study the formation and transmission of synaptic vesicles at the DRG neuron axon terminal under Mg treatment *in vitro*. During high potassium depolarization, FM1-43 bound to the membrane and was internalized into synaptic vesicles through bulk endocytosis. Then, the F1-43 stained synaptic vesicles were visualized under a confocal microscope and their formation and migration were recorded live. The triggered laser wavelength was 488nm and the emission wavelength was 600nm for FM1-43 under confocal microscopy[220-222].

The experiment included the following three steps:

**1). FM1-43 loading and labeling:** First, we dissolved FM1-43 powders in distilled water to stock the solution with a concentration of 4mM. We then put the solution in a dark environment to avoid light sensitive degradation. We then prepared HL-3 KCl solution (free of $CaCl_2$ and $MgCl_2$) as follows: 25mM NaCl, 90mM KCl, 10mM $NaHCO_3$, 5mM HEPES (4-2-hydroxyethyl)-1-piperazineethanesulfonic acid), 30 mM sucrose, 5 mM threalose, at a pH of 7.2. We added 1μL FM1-43 stock solution to 1ml HL-3 KCl solution with Ca (containing 1.5mM CaCl, with a final concentration of FM1-43 was 4μM) and prepared an FM1-43 labeling solution. DRG neurons were then incubated in a FM1-43 labeling solution for 5 minutes. Once the labeling solution was added, exocytosis and endocytosis at the axon terminal were induced with calcium-triggered depolarization. FM1-43 labeling ensued in 5 minutes.

**2). Stopping stimulation:** Following 5 minutes stimulation, FM1-43 labeling solution was removed and the neurons were washed three times over a total of 5 minutes with a generous amount of HL-3 solution free of Ca and Mg to remove the FM1-43 dye that was not internalized. It is important to not drop the solution on the top of neuron,

but to gently pipette the solution on the side of neuron cell to avoid direct interference.

**3). Mg treatment and recording:** After washing, we chose a single DRG neuron with classical axon terminal to review under confocal microscopy. The designated neuron with green florescence-stained synaptic vesicles was recorded by florescence imaging before the Mg treatment. Then, an $MgCl_2$ stock solution (1M) was pipetted into the medium, making the Mg concentration rise to 1mM. After 5 minutes of incubation, the same neuron was recorded using a florescence image. The Mg concentration was adjusted to 2mM and incubated for 5minutes, and the same neuron was recorded. Likewise, the designated neuron was recorded in a medium with Mg concentrations of 4mM and 8mM. The florescence image recorded synaptic vesicles replenishing in neuron body and the axon terminal along with the augmenting of the Mg ion concentrations. A Zeiss 510 confocal microscope and a Zeiss digital camera (Axiocam MRm) were both used in our experiment for image acquisition. N-Methyl-D-glucamin (NMDG+) (Sigma. USA) was used as the negative control in the experiment. N-Methyl-D-glucamin (NMDG+), an organic monovalent cation with a much larger size (approximately 7.3 A in mean diameter) than $K^+$ (2.66 A in diameter), was thought to be a blocker of the Kv channels by competitively inhibiting the entrance of potassium ions.

### 4.2.3 Cell Mg influx detection

DRG neurons were seed on the 25 mm diameter glass coverslips in six well-plates and incubated for 24 hours. We made sure the cells firmly adhered to the slides and were totally spread, which was critical for real time detection under the fluorescence camera when treated with a high concentration $MgCl_2$. Several individual cells were chosen for detection.

MSCs were seed on the 25 mm diameter glass coverslips in six well-plates with a density of 5000 per $cm^2$ and incubated for 24 hours. We ensured the cells firmly adhered to the slides and totally spread. The single and individual cells were delineated and recorded.

Cells grown on 25 mm diameter glass coverslips were washed 3 times with an Mg-free Margo solution to remove the culture medium. Then, they were incubated in the Mg-free Margo solution and supplemented with 2μM Mg-Fura-2 and 1μM Pluornic F-127 for 30 minutes at $37^{o}$ C incubator. After that, the cells were washed twice and kept in the Mg-Fura-2-free Mg-free Margo solution for another 30 minutes at room temperature in the dark. At the start of the experiment, cover slips were transferred to a mini-chamber and maintained in the Mg-free Margo solution. $MgCl_2$ (1mM, 2mM, and 10mM) was added after the baseline was stable.

**For channel screening:** After $MgCl_2$ (10mM) was added, till the baseline grew stable nitrendipine (50μM) was applied to block the MagT1 channel; ruthenium red (50μM) and 2-Aminoethyl diphenyl borinate (2-APB) (100μM) separately blocked TRPM6 and TRPM7. The same amount of DMSO (a solvent of three blockers) was applied as to the negative control. For the pH value effect on Mg influx, the pH value of Mg-free Margo was adjusted to 6.5, 7.5, or 8.5 with HCl or NaOH, respectively. Then the Mg influx in MSCs was recorded under a different pH medium.

Measurements were taken on an epifluorescence microscope (Nikon Eclipse Ti, Japan) equipped with a CCD camera (Spot Xplorer, USA) and a Fluor 20X objective lens (0.75 NA) (Nikon, Japan) controlled by the MetaFluor software (Universal Imaging). An Xenon lamp (Hamamatsu, Japan) was used to provide a dual excitation at 340 and 380 nm, and emissions were collected at 510 nm.

*Chemicals:* Mg-Fura-2 (Molecular Probe, USA), Pluronic F-127 (Molecular Probe,

USA), $MgCL_2$ (Sigma, USA), 2-Aminoethyl diphenyl borinate (2-APB) (Sigma, USA), and Nitrendipine (Sigma, USA)

Total eight rats were used to isolate DRG neuron. All the experiments were conducted at least three times. Paired and unpaired student-t test was used in statistical analysis.

## 4.3 Results

### 4.3.1 Mg ions promoted synaptic replasticity in DRG neurons

DRG neurons from the L3-L5 lumber level were isolated from rats. CGRP was stained and shown as red dots spreading over whole cell body in a single neuron by an immunofluorescent method. Synaptic vesicles with encapsuling neuropeptides (ex. CGRP) in large dense-core vesicles were stained with FM1-43 dye in green light granules[223]. A single DRG neuron morphology was revealed. (Figure 4.3.1) The synaptic vesicles (green spots) and CGRP peptide (red granules) were shown in the fluorescent image. (Figure 4.3.1)

Before Mg ion treatment, the green light was mainly located at the neuron body. Few vesicles were distributed at the axon terminals. After Mg ion treatment, the green spots grew dense in the axon terminals, which indicated that the synaptic vesicles were aggregated in the axon terminal under high Mg conditions. NMDG treatment, as our negative control, resulted in no obvious aggregation of synaptic vesicles in the neuron axon terminals. According to the results using fluorescent staining of the synaptic vesicles, we concluded that physiology concentration of Mg ions (about 1mM) and a high concentration (2mM) each significantly promoted the replenishing of the synaptic vesicles in the axon terminals. It is probable that Mg ions fluxed into the neuron and promoted synaptic vesicles transmitting from the neuron body to the axon terminals in very short interval (5minutes). The aggregation of synaptic vesicles in the axon terminal created the precondition for mass neuropeptide CGRP release after depolarization to neuron. That might be the background of the high CGRP content in the Mg implanted femur cortical bone tissue. (Figure 4.3.2 A, B)

### 4.3.2 Mg entered neuron through channel MagT1

Was the Mg ions' effect of synaptic replasticity and vesicle transportation the result of Mg ion influx in neuron? We did real time intracellular Mg detection in the DRG

neuron under fluorescent microscopy to find out. The fluorescence dye Mg-Fura-2 had a monomer emission wavelength of 380nm, its $Mg^{2+}$- Mg-Fura-2 compound possessed an emission wavelength of 340nm, and its fluorescence ratio 340/380nm represented the intracellular Mg ion signal. The curve lines and quantitative analysis indicated that inner neuron Mg was significantly increased when the culture was changed from an Mg free medium to an Mg medium (1mM and 2mM) (Figure 4.3.3.A). Meanwhile, cellular Ca content was correspondingly reduced (Figure 4.3.3.B). This result indicated that a neural $(Mg^{2+})_{in}$ increase under Mg treatment may be the major factor contributing to synaptic replasticity and vesicle migration to axon terminals. There were three important ion channels for Mg ion transportation across the cell membrane in eukaryocytes: TRPM6, TRPM7, and MagT1[219,224]. We chose three kinds of chemicals: ruthenium red, 2-Aminoethyl diphenyl borinate (2-APB), and nitrendipine, respectively blocking TRPM6, TRPM7 and MagT1[62,225,226]. Real time intracellular Mg detection curves did not show a significant $(Mg^{2+})_{in}$ decrease in the treatment of these three kinds of blockers because the solvent DMSO could trigger ($Mg^{2+}$) an influx in the DRG neuron. The quantitative results indicated that only nitrendipine significantly inhibited ($Mg^{2+}$) influx by 55% in the DRG neuron; the other two blockers had no significant effect on $(Mg^{2+})_{in}$ reduction. This result indicated that MagT1 was a chief channel for ($Mg^{2+}$) influx in the DRG neuron under Mg treatment: it was critical for Mg ions' replenishing effect on the synaptic vesicles and in promoting their transportation. (Figure 4.3.3 A, B, C)

### 4.3.3 Mg influx in MSCs under different pH circumstances

We hypothesized that Mg ions' osteogenic effect on MSCs resulted from Mg ion influx into the MSCs. So we detected Mg ions' influx to PDCSs and BMSCs under acid (pH 6.5), neutral (pH 7.5), and basic alkaline (pH8.5) cultural conditions.

From the colored signal curves, we knew that the cellular Mg ion signal quickly, in tens of seconds, reached a high level after high concentration (10mM $MgCl_2$) Mg treatment and then was stable at a plateau in 3 minutes at all three pH conditions. This phenomenon of high $(Mg^{2+})_{ex}$ triggering high $(Mg^{2+})_{in}$ was most significant in neutral conditions (pH 7.5). $(Mg^{2+})_{in}$ and increased after high $(Mg^{2+})_{ex}$ at three cultural conditions, as shown in the diagrams in Figure 4.3.4. Both the peak amount and the plateau amount of $(Mg^{2+})_{in}$ $(Mg^{2+})_{in}$ increased more significantly in neutral conditions than in acid or alkaline conditions. In the colored curve graphs, the high $(Mg^{2+})_{in}$ plateau significantly declined after 50μM nitrendipine administration in several seconds. This nitrendipine dominated $(Mg^{2+})_{in}$ decline was significant in neutral conditions. The diagrams in Figure 4.3.4 show that nitrendipine can slightly but significantly lower high $(Mg^{2+})_{ex}$ induced peaks and plateaus $(Mg^{2+})_{in}$ with an increase in pH 7.5 conditions. Although the nitrendipine's blocking effect was significant in the acid condition, its performance seemed to go the opposite side when the pH value turned to 8.5.

As shown in the colored curve graphs and diagrams, we confirmed that when high $(Mg^{2+})_{ex}$ led Mg ions to enter into the PDCSs and BMSCs, this gave rise to the increased $(Mg^{2+})_{in}$. This increased $(Mg^{2+})_{in}$ caused by high $(Mg^{2+})_{ex}$ was significantly inhibited, however, by nitrendipine. As nitrendipine was a specific antagonist to the cell membrane Mg ion channel MagT1, we concluded that high $(Mg^{2+})_{ex}$ brought the Mg ions to enter into the MSCs through the cell membrane Mg specific ion channel MagT1. MagT1 channel's activity might be greatly affected by the pH value of the cell culture. (Figure 4.3.4-6)

Mg ion influx was not blocked by 2-APB or ruthenium red (data did not show here).

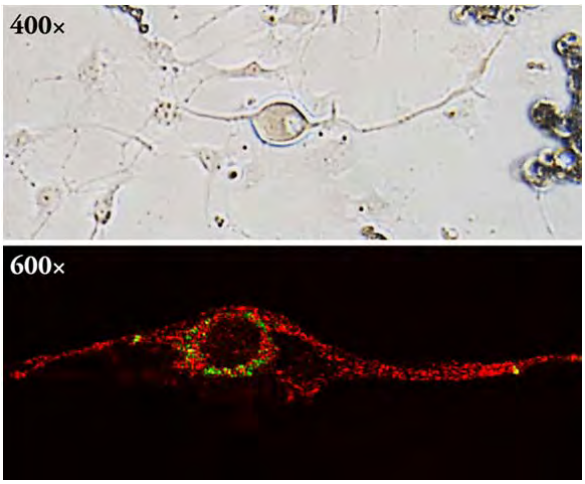


**Figure 4.3.1.** Single DRG neuron under light microscopy (above, 400×) and confocal microscopy (below, 600×). Green light spots are FM1-43 stained synaptic vesicles. Red light dots are immunofluorescently stained CGRP peptide.

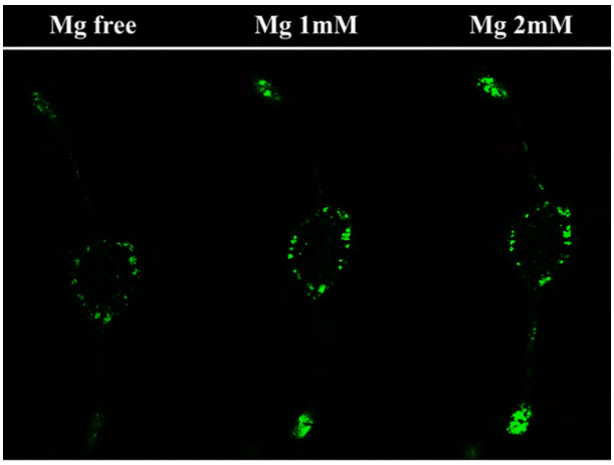


**Figure 4.3.2.A.** Single DRG neuron and its synaptic vesicles (green light spots) were pictured under confocal microscopy (600×). From the Mg free medium to the Mg medium (1mM and 2mM), neuron synaptic vesicles were replenished (replasticity) and migrated to the axon terminals.

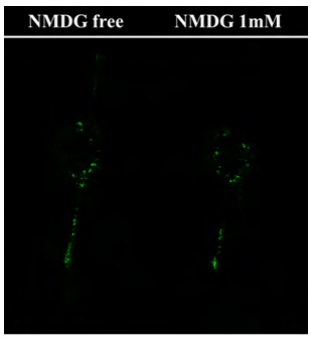

**Figure 4.3.2.B.** A single DRG neuron and its synaptic vesicles (green light spots) were pictured under confocal microscopy (600×). N-Methyl-D-glucamin (NMDG+) treatment was a negative control to Mg.

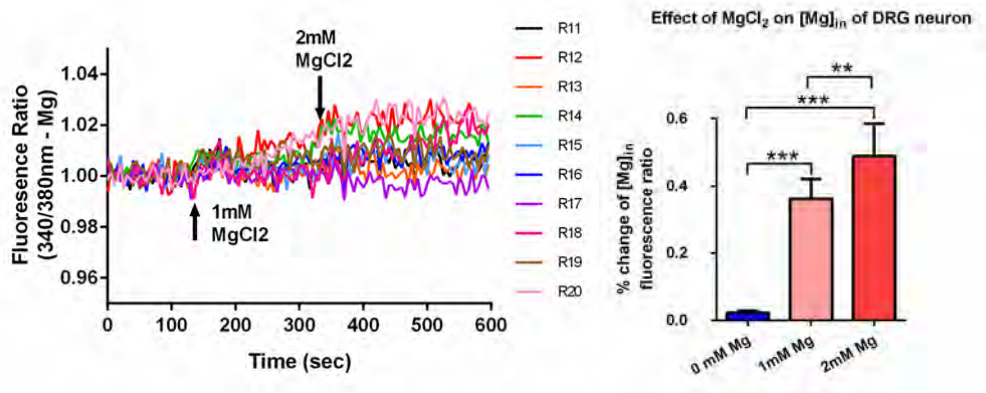


**Figure 4.3.3.A.** Real time cellular Mg ion flux curves of fluorescence ratio representing Mg entered into the DRG neurons were recorded after Mg increase. % change of fluorescence ratio to $(Mg^{2+})_{in}$ was analyzed after the Mg medium concentration was increased to 1 and 2 mM. All values were given as the mean ± S/D. A two-way ANOVA was performed between groups and significant differences were defined as: *p<0.05, **p<0.01, and ***p< 0.001.

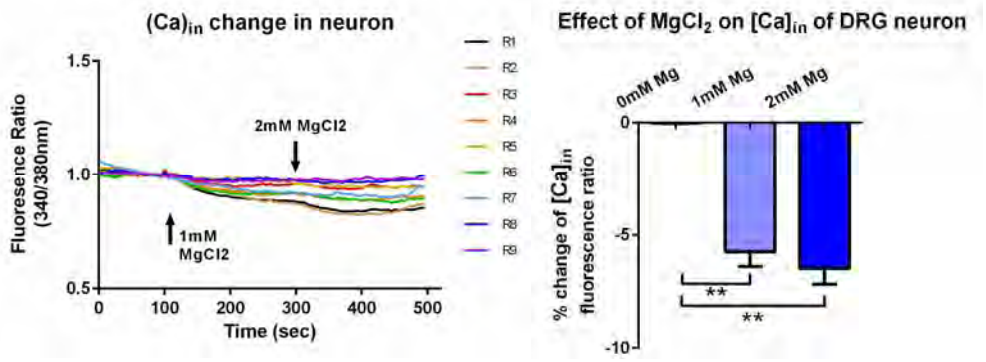


**Figure 4.3.3.B.** Real time cellular Ca ion flux curves of a fluorescence ratio representing Ca entered into DRG neurons were recorded after an Mg increase. The % change of fluorescence ratio to $(Ca^{2+})_{in}$ was analyzed after the medium Mg concentration was increased to 1 and 2 mM. All values were given as the mean ± S/D. A two-way ANOVA was performed between groups and significant differences were defined as *p<0.05, **p<0.01, and ***p< 0.001.

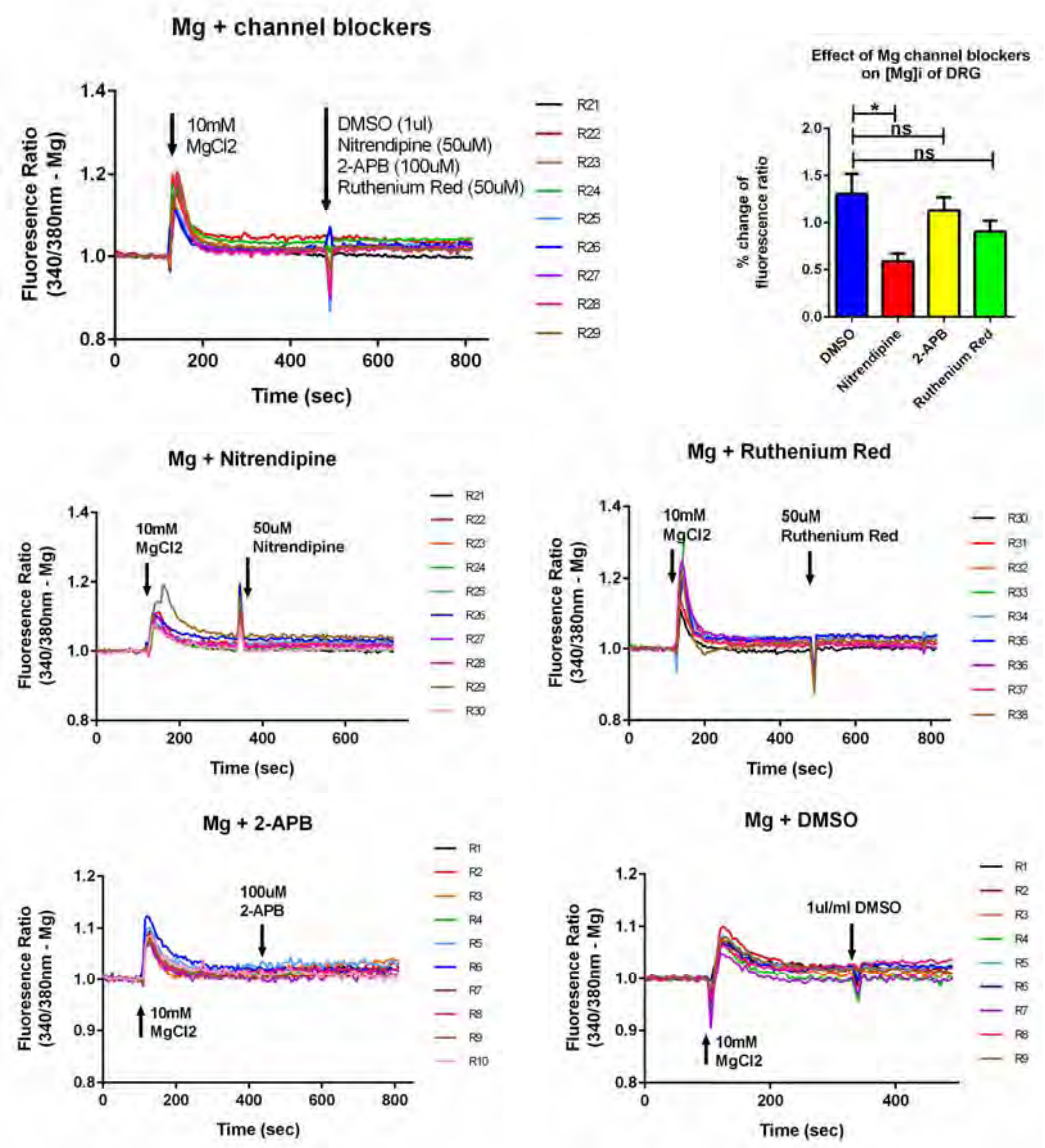


**Figure 4.3.3.C.** Real time cellular Mg ion flux curves of fluorescence ratio were recorded after the administration of channel blockers ruthenium red, 2-APB, and nitrendipine in a 10 mM $MgCl_2$ medium in DRG neuron. The % change of fluorescence ratio to $(Mg^{2+})_{in}$ was analyzed after three blockers administration, with DMSO as the solvent of the three chemicals as the control. All values were given as the mean ± S/D. A two-way ANOVA was performed between the groups and significant differences were defined as: *p<0.05, **p<0.01, and ***p< 0.001.

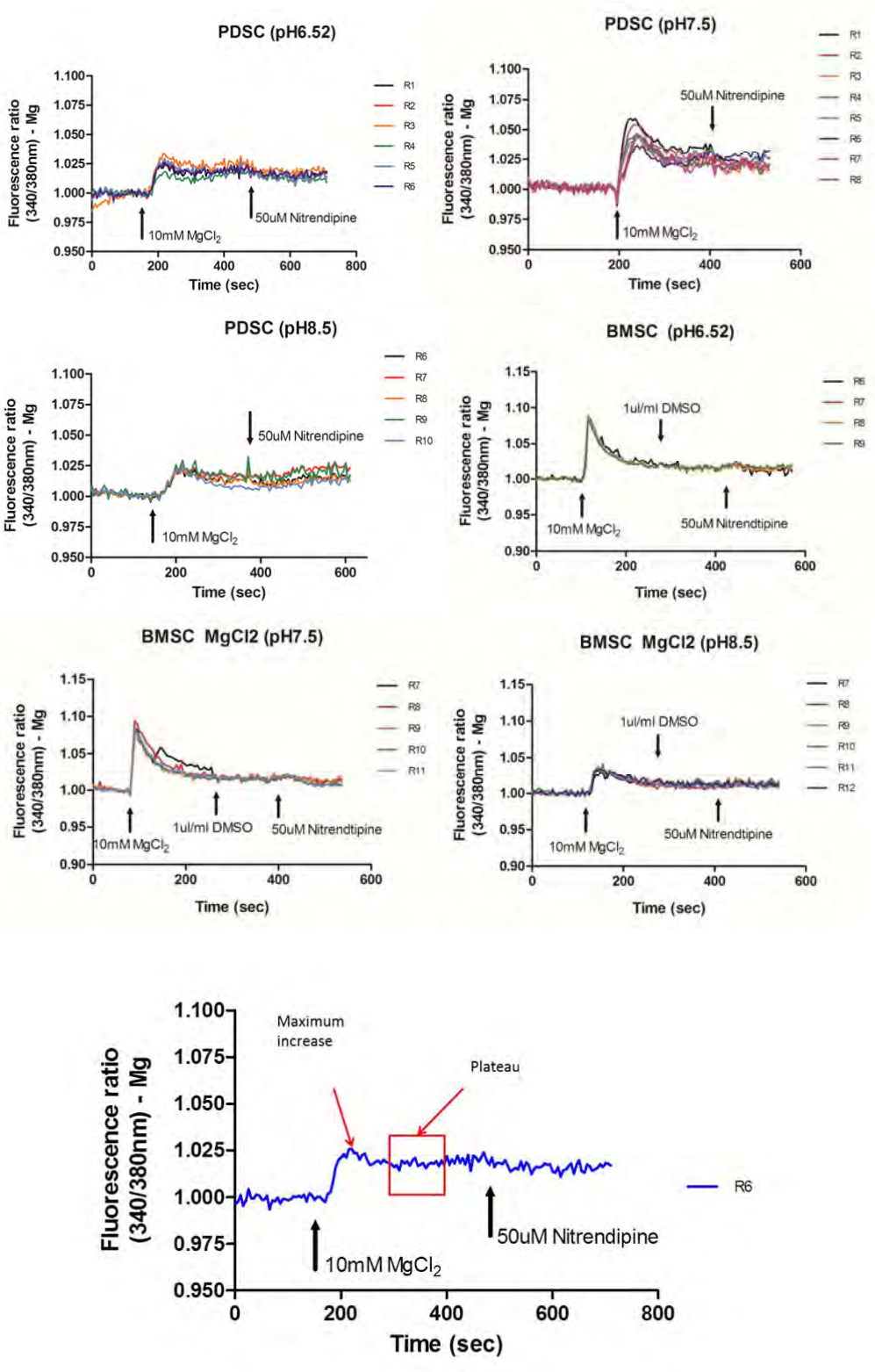


**Figure 4.3.4.** Real time cellular Mg ion flux curves of fluorescence ratio representing Mg entered into MSCs was recorded after Mg was increase. The maximum increase and plateau of cellular Mg was indicated as a red arrow.

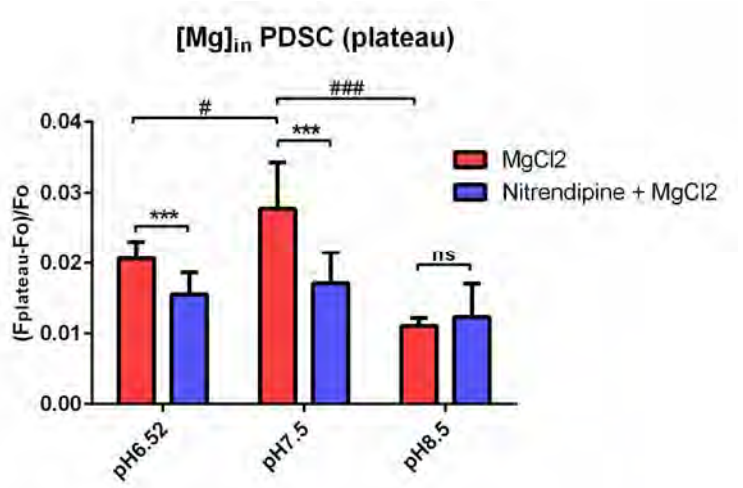


**Figure 4.3.5.** The % change of fluorescence ratio to $(Mg^{2+})_{in}$ in PDSCs was analyzed after we administered the channel blocker nitrendipine in three pH value conditions. All values were given as the mean ± S/D. A two-way ANOVA was performed between groups, and significant differences were defined as *p<0.05, **p<0.01, and ***p< 0.001, #p:< 0.05, ## p:< 0.01 and ### :p< 0.001 versus the control. ns:p>0.05.

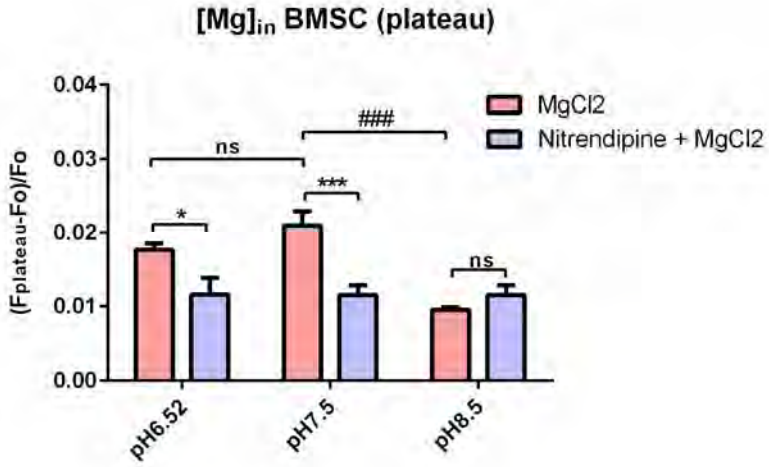


**Figure 4.3.6.** The % change of the fluorescence ratio to $(Mg^{2+})_{in}$ in BMSCs was analyzed after we administered the channel blocker nitrendipine in three pH value conditions. All values were given as the mean ± S/D. A two-way ANOVA was performed between groups, and significant differences were defined as: *p<0.05, **p<0.01, and ***p< 0.001, #:p< 0.05, ## p:< 0.01 and ### p< 0.001 versus the control. ns:p>0.05.

## 4.4 Discussion

### Mg ions promoted synaptic replasticity

The Neuron synaptic vesicles exo/endocytosis were considered to be controlled by myosin family of motor proteins. The inhibition of non-muscle myosin IIb could retard synaptic vesicles transmission after evoking potential in the hippocampus neuron. This suggested that non-muscle myosin IIb, myosin IV, and Va,b had their own respective effects: non-muscle myosin IIb was critical in actin filament contraction and crosslinking on actin cytoskeleton dynamics; myosin IV was responsible for the tethering of organelle and the transport of uncoated endocytic vesicles (UEVs); and myosin Va,b were responsible for organelle anchoring and motility, filament organization of endoplasmic reticulum (ER), and recycling Endosomes (REs)[227,228]. These myosin family proteins played a pivotal role in mediating actin cytoskeletal rearrangement and cargo transport. These molecular and structure dynamic activities, which occurred in neural synapses, directly determined synaptic plasticity regulation. In 2004, Guosong Liu et al. found that the plasticity of presynaptic terminals in the hippocampus neuron could be enhanced by selectively blocking $(Ca^{2+})_{in}$ their influx through channel NMDAR (N-methyl-D-aspartate receptor). A blocking effect also could be fulfilled through high extracellular $Mg^{2+}$ supplement ($Mg^{2+}$ concentration increased to 1.2 and 2 mM). High Mg treatment led to a reduced $(Ca^{2+})_{in}$ influx and an up-regulated NMDAR function, particularly an increase in the proportion associated with NR2B subunits. The enhanced NMDAR signaling under high Mg treatment triggered the activation of p-CREB transcription factor, which led to a unique gene expression that promoted neuron cell survival and synaptic plasticity[229,230]. It was found that the hippocampus neuron maintained its morphology and granule density at a high level of $(Mg^{2+})_{ex}$, and the stained synaptic

vesicles (FM1-43 puncta) increased 2.1 more than the control in the neuron body after 30 minutes high Mg treatment. The total presynaptic strength increased 5.5 fold and the synapses retained their plasticity for several weeks when $(Mg^{2+})_{ex}$ was elevated to 1.2 mM and 2 mM[229]. However, in Guosong Liu's study, hippocampus neuron plasticity was defined as the number of visually stained synaptic vesicles (they applied dye FM1-43 to stain the synaptic vesicles) after a theta-burst stimulation (TBS), which caused a depolarization to the neuron and triggered the neurotransmitters' release from the vesicles at the active zone on the pre-synaptic membrane.

The release of neurotransmitters underwent two postulated models of the synaptic vesicle exo/endocytosis process: a kiss-and-run pattern (about 40%) and a full vesicle collapse fusion (about 60%)[231]. Soon after and during depolarization and exocytosis, endocytosis was processed at the presynaptic membrane. The neuron replasticity, including endocytosis and synaptic vesicle reloading, was such a process. So, the increased FM1-43 florescence signal in the neuron body following excitation indicated enhanced replasticity after high Mg treatment in Guosong Liu's study. However, that study just detected the synaptic vesicles' signal at part of the neuron site; it did not show the whole picture of vesicle distribution in a neuron.

In our experiment, a single DRG neuron was pictured and the green light synaptic vesicles were distributed from the body to the axon. The synaptic vesicle signal distributed along the whole neuron body was easily detected for their transmitting direction and location. Our images gave more information than GuoSong Liu's results. In our experiment, after first loading FM1-43 by high potassium and growing it to a steady state, we treated the DRG neuron with a medium free of $Ca^{2+}$, which ensured that the neuron was not activated. After Mg treatment, we noticed that the number of

green puncta significantly increased in the neuron and aggregated to the axon terminal. This phenomenon was clearly different from Liu's observation. In that study, vesicle signaling increased at the neuron body, which indicated that the synaptic vesicles were reloading and reflourishing. In our study, in addition to replenishing the vesicle signal, the vesicles signal showed a clear directional transportation in the axon terminals. We proved that synaptic vesicles were replenished in the neuron body. Meanwhile, they directionally migrated to the distal axon terminal in a high Mg condition. This was the first time that we observed that high Mg treatment not only promoted DRG neuron replasticity, also observed by other people in the hippocampus neuron, but also directionally accelerated synaptic vesicle transmission from the neuron body to the axon terminal.

This observation could explain the increase of neuropeptides (CGRP) in the newly formed cortical bone tissue after Mg pin implantation in the femur canal. Nonetheless, the mechanism for vesicle transmission along the axon was not yet elucidated. This may be due to the NMDAR activity after the Mg ions blocked the influx of $(Ca^{2+})_{in}$, but this pathway was probably indirect sideways. The vesicle migration was directly carried by the myosin motor system, and reloading and migration of the synaptic vesicles must be dependent on some factor that directly charged or otherwise interacted with non-muscle myosin molecules.

In our study, Mg influx to the neuron was observed under a high $(Mg)_{ex}$ medium; meanwhile, $(Ca)_{in}$ was reduced with an $(Mg)_{in}$ increase. This reduction of $(Ca)_{in}$ was in accordance with Liu's study; however, an $(Mg)_{in}$ increase has not been noted by other researchers. This $(Mg)_{in}$ increase was a direct factor in the synaptic vesicles' reloading and migration. There were $Mg^{2+}$ bonding sites in every cytoplasmic molecule, even those in the myosin motor family. In particular, $Mg^{2+}$-activated

vacuole-like ATPase was found to be the first-stage controller of clathrin-mediated vesicle formation[232]. There have also been some reports indicating that $(Mg)_{in}$ was critical to the assembling and motor action of cyto-motor molecules [233,234]. The direct interaction between $Mg^{2+,}$ vacuole-like ATPase, and the myosin molecule has the power to promote the reloading and migration of synaptic vesicles along the myosin system. Our future study will focus on the Mg's effect on vacuole-like ATPase and myosin activity.

**Cell membrane Mg channels in Mg influx**

In eukaryocytes, cell membrane Mg channels are a broad range of transmembrane proteins with similar structures and amino sequences. They were generally encoded as *SLC41A1*, *SLC41A2*, *Mrs2*, *ACDP2*, *Paracellin-1*, *Claudin 16*, *TUSC3*, *MagT1*, *TRPM6*, and *TRPM7* genes, which have same role in prokaryotic cells[235,236]. Among these Mg ion transports, TRPM6, 7 and MagT1 were the most important channels in the Mg ion metabolism of vertebrate organisms [62,84,224,237]. However, TRPM6 was considered to be mainly expressed at the epithelia cell membrane in the kidneys, intestines, and lungs. TRPM7 was ubiquitously expressed in all the tissue, and it was proved to act with TRPM6 to form a TRPM6/TRPM7 heteo-oligomerization and create Mg transmembrane conduction in a distal convoluted tubule[238]. Channel MagT1 was also expressed in all the tissues and was considered responsible for mammalian cell $Mg^{2+}$ uptake[224,237]. There was still some controversy around the $Mg^{2+}$ metabolism of TRPM7 in mammalian cells. Lillia showed TRPM7's essential role for $Mg^{2+}$ homeostasis in mammals, while Jin found that the deletion of TRPM7 could disrupt embryonic development and thymopoiesis in mice without altering $Mg^{2+}$ homeostasis in T cells[84,239].

In our study, Mg channel TRPM6, TRPM 7, and MagT1 blockers were applied to real

time cellular $Mg^{2+}$ detection. The TRPM6 blocker was ruthenium red; the TRPM7 blocker was 2-APB; and the MagT1 channel blocker was nitrendipine[225,226]. Our results showed that TRPM6 and 7 blocking with ruthenium red and 2-APB did not perturb Mg ions' intracellular transportation under high Mg condition either in MSCs or DRG neurons while the influx of Mg ions in stem cells and neurons could be significantly reduced by blocking MagT1. This indicated that MagT1 was the most important channel for cellular Mg ion metabolism, especially when extracellular Mg concentration was increased.

Mg ions' osteogenic effect on MSCs was probably caused by a MagT1 mediating $(Mg)_{in}$ increase. This deduction had already been proven in our previous studies. After we knocked down the expression of MagT1 in MSCs, Mg's osteogenic effect on MSCs was significantly reduced. In fact, overexpression of MagT1 in MSCs led to a significant enhancement of Mg's effect on MSCs osteogenic differentiation. However, there were still important questions waiting for us to explore: 1) Did MagT1 itself act in stem cell differentiation?; 2) If Mg ion rather than MagT1 acts as the direct factor in stem cell differentiation, what is the substrate downstream? We will explore this fascinating enigma in future studies.

**Conclusion**

Mg ions entered into stem cells and neurons through cell membrane Mg channel MagT1. Previously considered another cell membrane, Mg channel TRPM6 and TRPM7 were not the chief channels for cellular Mg ion influx. Increased $(Mg)_{in}$ could promote synaptic vesicle replenishing and transportation in the DRG neuron. It also probably promoted the stem cells' osteogenic differentiation.

# Chapter 5

## Pure Metal Mg
## Accelerated bone fracture healing
## In OVX rats

## 5.1 Introduction

This project was based on our finding that Mg metal induced new bone formation in the femur periosteum region after intramedullarily implanting it into the rat femur. This phenomenon indicated that Mg metals may be applied to accelerate fracture healing, especially in the fracture healing of osteoporosis bones.

We knew that Mg ions were actively absorbed into the intestine epithelial tissue and reabsorbed in the nephron distal convoluted tubule, and that almost 60% of the body Mg was reserved in the bone, with less than 1% of body Mg existing as serum free ions in circulation. After menopause in women, estrogen declines. This serum estrogen decline leads to the consequence that Mg channel TRPM6 has reduced expression in the epithelia cells at the intestine and nephron sites. Estrogen can integrate with the repressor of estrogen receptor activity (REA), a protein suppressed TRPM6' expression in the epithelial cells of the nephron and intestine. This makes estrogen competitively inhibit REA's suppression effect on TRPM6 synthesis in nephron epithelial cells so that estrogen down regulation can weaken the absorption of Mg ions into the kidneys and intestines of menopausal women, which may lead to a serum Mg decline and hypomagnesemia. When Mg absorption and reabsorption from the reserve pool of body Mg occurs, bone Mg releases into circulation to help serum Mg maintain its physiological concentration range and retain the body's Mg equilibrium. This makes bones the first organs to experience a negative balance during a whole body Mg deficiency. Furthermore, many researches have noticed that sensory neuropeptide CGRP significantly reduced peripheral circulation in aging rats with hypertension[240,241]. These findings make Mg metal a fascinating candidate to be used for the bone fracture repair of OVX osteoporotic rats.

In this chapter, we evaluated pure Mg metal's effect on the enhancement of

osteoporotic bone fracture healing. An OVX rat closed fracture model was established. Considering the low mechanical strength and high biodegrading rate of Mg metal, using pure Mg metal to fix the rat femur bone fracture was not practical—the Mg pin was broken at week 3 after being fixed to mice femur bone fractures—so we chose a stainless steel needle as the strength bearing holder to fix the fracture. We opened a window at the middle of the needle as an Mg releasing vent designed to fit the fracture site. This was a novel design for a needle pin used for the intramedullary repair of a bone fracture. An Mg metal pin with a diameter less than the needle's inner diameter was inserted into the hollow needle. Mg ions, during degradation, would be released from the vent and exercise their effectiveness on new bone formation at the fracture site. That was the basic concept of this study.

After surgery, X-ray photography and micro-CT were performed at weeks 2, 4, 8, and 12. The Mg promotion of new bone formation achieved a peak at week 4, and callus TV and BV at the fracture site in our micro-CT analysis were consistent with our X-ray results. At the end of week 12, our micro-CT results showed that callus BV and TV at the fracture site had no differences between the Mg treated group and the control group; however, callus BMD in the Mg treated group was significantly higher than that of the control group. Mechanical testing indicated that Mg treated fractured femurs bore a higher ultimate load than the control. This pilot study laid a foundation for us to explore Mg's clinical application to the orthopedic field in the future.

## 5.2 Materials & Methods

### 5.2.1 Intramedullary nail designing

Using the 3-dimension software SolidWorks (Waltham, Massachusetts, USA), we designed three kinds of hollowed needle with vents opened at the middle. The manufactured nail was based on a spinal needle purchased from Terumo. The spinal needle (18G×90mm, Terumo, USA) had a length of 90mm, an outer diameter of 1.27mm, and an inner diameter of 0.9mm. It was made of stainless steel, which maintained a high enough mechanical ability to fix the fractured bone in rats. The vent in the middle site of needle had three kinds of designs: 1) A unilateral window with a depth of 1/2 the needle's outer diameter; 2) a unilateral window with a depth of 1/3 the needle's outer diameter; and 3) a total of 18 regular interlacing holes with a diameter of 0.5mm distributed in lengths of 1cm crisscrossing the needle's surface. The vent/window design was created with mechanical cutting on a numerical control machine tool. The vent hole design was created with electric sparks burned in vertical directions at the transverse section at equal distances of 0.5mm by a machining company (Free Crafts Man Tec.) in ShenZhen. (Figure 5.2.1)

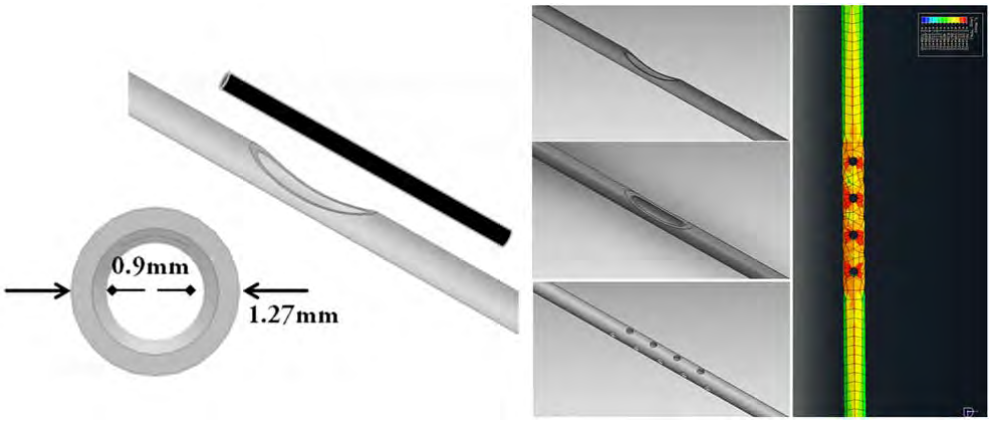


**Figure 5.2.1.** 3 dimensional drawing of needles with diverse vent patterns in SolidWorks by Tian Li. The needle, with length of 90mm and outer diameter of 1.27mm and inner diameter of 0.9mm, could encapsule the Mg pin (with a diameter of 0.5mm) (**above**). The vent in the middle of the needle had three kinds of designs: 1)

A Unilateral window with a depth of 1/2 needle's outer diameter; 2) A unilateral window with a depth of 1/3 the needle's outer diameter; 3) Regular interlacing holes with diameters of 0.5mm crisscrossing the needle surface (with a total 18 holes distributed in lengths of 5mm). (**below**)

Finite elemental analysis (FEA) was applied to select the optimal needle design with the best mechanical performance. A 10-node tetrahedron element, SOLID 92, was chosen to mesh the needle in ANSYS (ANSYS, Inc., Canonsburgh, PA, USA). The size of the mesh element was 0.05mm. The mechanical properties of the needle were input to software to set the basic parameters; the stainless steel modulus was 210 GPa and the poison ratio was 0.3. In the FEA analysis, four-point bending was set to evaluate the bending strength of the needle with the diverse mid-vent design. Two supporting places with widths of 2cm were found at the middle site of the vent. Loads of 40 N were applied at two points above with widths of 1cm. The parallel vertical force of 20N at each loading point was applied downwardly to the vent site of the needle. Following this FEA simulating evaluation, we selected the most appropriate needle design—i.e., the one with greatest strength to sustain pressure and enough opening in the window area to releasing Mg ions. (Figure 5.2.2)

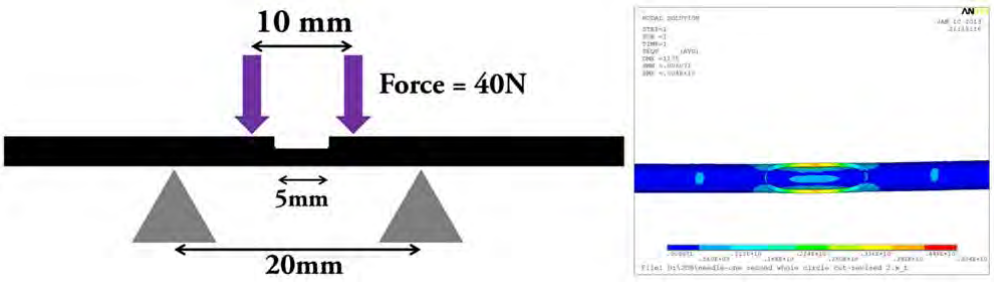


**Figure 5.2.2.** A designed intramedullary nail did the mechanical testing in our Finite Elemental Analysis (FEA). Pictured **above** is the mechanical simulation testing. Pictured **below** is the report of the testing in FEA: at the middle and bilateral sites of the vent, the sites with the warm color bore more stress and the sites with a cold color bore less stress.

The manufactured intramedullary nail is shown below. The needle tail was curved as a hook to hold the fracture bone tightly. The length of the hooked needle was a match to the femur of the rat, and the vent was fit to the fracture line. Mg pins with equal lengths of 20mm and equal diameters of 0.5mm were made as cylinder shapes with uniform weights and inserted into the hollow needle during surgery. (Figure 5.2.3)

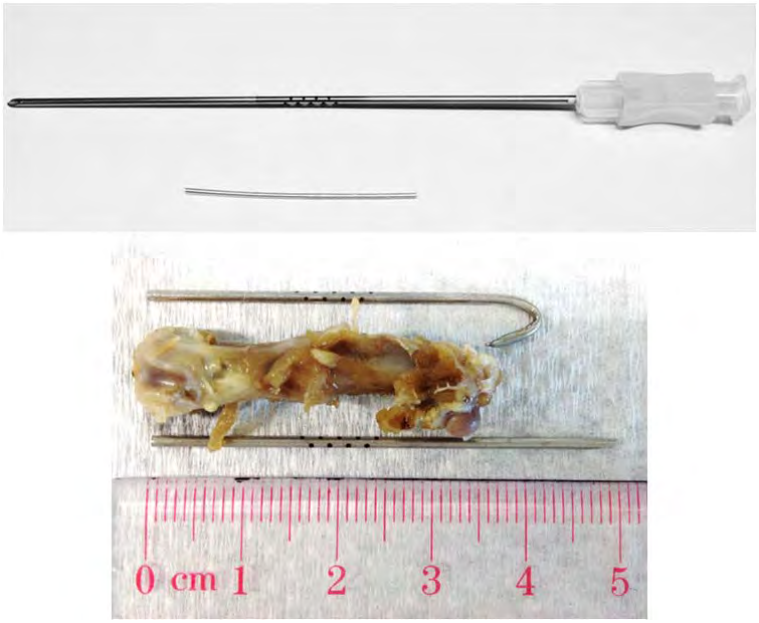


**Figure 5.2.3.** Manufactured needle with drilled holes and pure Mg pins (above). A manufactured intramedullary nail was used to fix the femur fracture in the OVX rat. The needle was strong enough to fix the fracture bone, and the vent that facilitated Mg ion release was designed to fit the fracture line.

***In vitro* Mg degradation analysis**

An Mg cylinder-shaped pin with a length of 20mm and diameter of 0.5mm was inserted into the nail and the two tips sealed; then it was immersed into 6ml DMEM (10% FBS). The medium volume was chosen according to the following equation: medium volume=0.2×area of the immersed material's surface ($mm^2$) (American

Society for Testing and Materials, ASTM, Practice A 262). We extracted a 500ul immersion medium at hour 6, day 1, day 3, week 1, week 2, month 1, and month 2 after the Mg pin and the nail were immersed into the medium. 6 ml of the medium were added after every extraction. We diluted the extraction medium to 50ml and detected the Mg ion concentrations with an Inductively Coupled Plasma (ICP)-Optical Emission Spectrometer (ICP-OES, Varian Vista-Pro, Australia). Emission intensities in the ICP-OES signals were measured at 279.553 nm for Mg. (Figure 5.2.4)

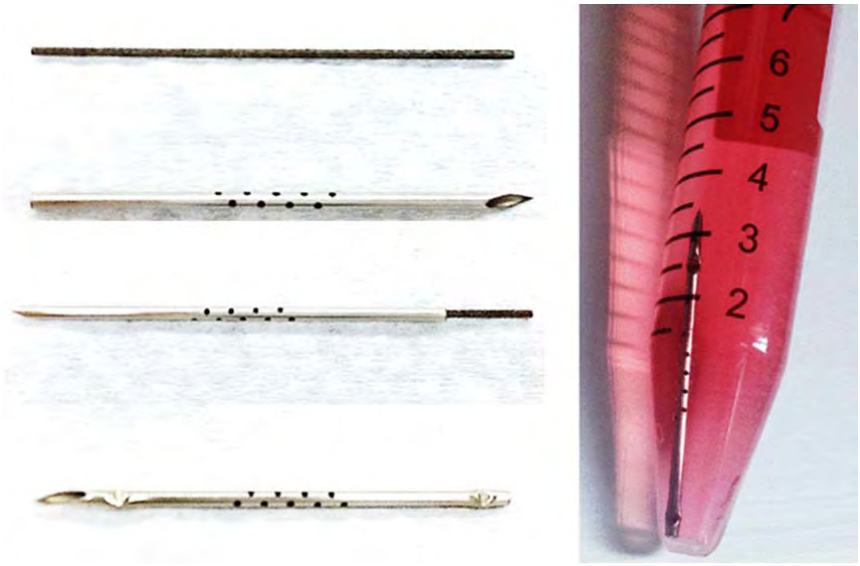


**Figure 5.2.4.** The black Mg pin was inserted into the designed nail and the tips were clamped to prevent Mg ion degradation and release through the tip holes. Then, the nail containing the Mg pin was immersed into the medium to evaluate the degradation of the Mg pin in it.

### 5.2.2 Experimental design of fracture healing

88 female S/D rats were obtained from the Laboratory Animal Services Center in CUHK. The Animal Experimental Ethics Committee at CUHK approved our experimental protocols (Ref. No. 13/003/MIS-5) (Appendix I). All rats got ovariectomy (OVX) at 6 months of age and were maintained for 3 months to develop osteoporosis[242]. A closed fracture on the right femur was created according to our established protocol[242]. Buprenorphine (0.03mg/kg, Temgesic, Schering-Plough, NJ,

USA) was given pre- and postoperatively for analgesics. All rats were allowed free cage movement, access to a standard rat diet, and tap water.

OVX Rats were randomly divided into two groups (n=6 rats/Group/time point): A steel nail with Mg insertion (SNMI) implanted group and a steel nail only (SN) group. Each group was further subdivided into weeks 2, 4, 8, and 12 time points. Lateral X-rays were taken weekly (with 5 second exposure times and a tube voltage of 35 kVp) in order to monitor the fracture healing status of the callus formation and its bridging. Calcein green (5 mg/kg sc. Sigma, Deisenhofen, Germany) was injected 2 weeks before euthanasia and xylenol orange (90 mg/kg sc. Sigma, Deisenhofen, Germany) was injected 1 week before euthanasia at all time-points. At the end of every time point, the rats were euthanized with an overdose of sodium pentobarbital and the fractured femora were harvested. (table 5.1)

**OVX rat model establishment**

A general anaesthesia (Ketamine (75 mg/kg) and Xylazine (10 mg/kg) mixture was given to the rats. After the rats were anaesthetized, the hair on both sides was shaven from the lower ribs to the top of the thighs. The dimension of the shaved area was approximately 4×4 cm. The shaved skin region was then sterilized with 0.5% Hibitane in 70% ethanol. The rats were positioned laterally and an incision the length of 8mm was made between the lowest rib and the top of the thigh. The exposed abdominal wall was dissected with a pair of scissors and an incision of 1cm was made. After this dissection of the lateral abdominal wall, the ovary was exposed in the abdominal cavity and explored. Then the ovary, along with part of the oviduct, concomitant vessels, and some visceral fat, was ligated (5-0 sutures, Mersilk, Ethicon Ltd., Belgium) and resected. The abdominal wall and the skin were sutured in layers

with an interrupted suture (4-0 sutures). After the removal of the ovary was completed on one side, the rat was turned to the other side and these surgical procedures were repeated. Buprenorphine (0.03 mg/kg, subcutaneous injection (sc), Temgesic, Schering-Plough, NJ, USA) was given as an analgesia after both ovaries were removed.

**Fracture creation and treatment**

After OVX was performed on the six-month-old rats, they were kept for three months to develop osteoporosis before a closed femoral fracture was created on the right femur of the rats[242]. In detail, under general anesthesia with ketamine and xylazine, the hair on the right limb was shaved and prepared with aseptic techniques (0.5% Hibitane in 70% ethanol). An incision the length of 10mm was made in the middle side of the limb and a 2mm incision was made to the patella (parapatellar incision). The femoral condyle was exposed through dissection of the joint capsule of the knee. The patella was laterally dislocated and the inter-condylar notch was exposed. The inter-condylar notch was used as an entry point for reaming, which was performed with an 18G needle until it was inserted through the entry point into the medullary canal. After the 18G needle perforated the proximal femur, the rat was positioned on a customized 3-point-bending apparatus, which was also used in our previous studies[242].

A transverse fracture was created in the mid-shaft (diaphysis) of the right femur by dropping a metal blade (about 500 grams) from a height of 35cm. The fracture was confirmed with antero-posterior and lateral radiographs. Then, a thin guiding puncture pin with diameter of 0.7mm and length of 80mm was intra-passed through the 18G needle until it penetrated the skin. Using a pincer, we then firmly fixed the thin pin and pulled the 18G needle out of the femur canal. After that, we refixed our designed

nail (needle-based) to the fractured bone through the guiding pin. When the guiding pin was pulled out, the Mg pin was inserted into the canal of the nail for treatment after insertion in vivo. The length of our designed nail was 45mm to match the 40mm length of the femur. The additional 5mm end was bent as a hook to prevent distal femur movement. Buprenorphine (0.03 mg/kg sc. Temgesic, Schering-Plough, NJ, USA) was given 15 min pre-operation and one-day post operation was allowed for analgesics.

| **Total 88** | **Group of SN (control)** | **Group of SNMI (Mg treated)** |
|---|---|---|
| **Week 2** | µCT scanning and X-ray radiography,<br>*decalcified sample histology and histomorphometric analysis (n=6)*<br>H&E staining for cell lines (osteoblast, osteoclast, chondrocyte, and osteocyte).<br>Safranin O staining for glycosaminoglycans in cartilage, hypertrophic chondrocytes. | µCT scanning and X-ray radiography,<br>*decalcified sample histology and histomorphometric analysis (n=6)*<br>H&E staining for cell lines (osteoblast, osteoclast, chondrocyte, and osteocyte).<br>Safranin O staining for glycosaminoglycans in cartilage, hypertrophic chondrocytes. |
| **Week 4** | µCT scanning,<br>*decalcified sample histology and histomorphometric analysis (n=6)*<br>H&E staining for cell lines (osteoblast, osteoclast, chondrocyte and osteocyte).<br>Safranin O staining for glycosaminoglycans in cartilage, hypertrophic chondrocytes.<br>*Fluorescence staining (n=6) for undecalcified samples.* | µCT scanning,<br>*decalcified sample histology and histomorphometric analysis (n=6)*<br>H&E staining for cell lines (osteoblast, osteoclast, chondrocyte and osteocyte).<br>Safranin O staining for glycosaminoglycans in cartilage, hypertrophic chondrocytes.<br>*Fluorescence staining (n=6) for undecalcified samples.* |
| | µCT scanning, | µCT scanning, |

| | | |
|---|---|---|
| **Week 8** | *decalcified sample histology and histomorphometric analysis (n=6)*<br><br>H&E staining for cell lines (osteoblast, osteoclast, chondrocyte and osteocyte).<br><br>Safranin O staining for glycosaminoglycans in cartilage, hypertrophic chondrocytes.<br><br>*Fluorescence staining (n=6) for undecalcified samples.* | *decalcified sample histology and histomorphometric analysis (n=6)*<br><br>H&E staining for cell lines (osteoblast, osteoclast, chondrocyte and osteocyte).<br><br>Safranin O staining for glycosaminoglycans in cartilage, hypertrophic chondrocytes.<br><br>*Fluorescence staining (n=6) for undecalcified samples.* |
| **Week 12** | µCT scanning,<br>*decalcified sample histology and histomorphometric analysis (n=6)*<br><br>H&E staining for cell lines (osteoblast, osteoclast, chondrocyte and osteocyte).<br><br>Safranin O staining for glycosaminoglycans in cartilage, hypertrophic chondrocytes.<br><br>*Mechanical test and fluorescence staining (n=8)* | µCT scanning,<br>*decalcified sample histology and histomorphometric analysis (n=6)*<br><br>H&E staining for cell lines (osteoblast, osteoclast, chondrocyte and osteocyte).<br><br>Safranin O staining for glycosaminoglycans in cartilage, hypertrophic chondrocytes.<br><br>*Mechanical test and fluorescence staining (n=8)* |

**Table 5.1.** We allotted 6 rats for decalcified and calcified analysis in each group and at each time point. At week 12, we allotted 8 samples for each group to do mechanical testing.

### 5.2.3 Radiography and histomorphometry analysis

**Radiographic Analysis**: The radiographs were analyzed according to our established protocol[242]. Radiographic healing was defined as the complete bridging of mineralized calluses, with callus width (CW) defined as the maximum width of the callus, and the callus area (CA) was equal to the size of its radiopaque area under X-ray photography. Both CW and CA were measured with lateral X-rays of each rat using Metamorph Image Analysis System (Universal Imaging Corporation,

Downingtown, PA, USA). Each callus measurement was repeated three times and averaged for statistical analysis.

**Micro-CT Analysis**: The fracture femur was harvested after euthanasia and the nail was carefully removed. Then the fracture femur was wrapped in wet gauze, fitted into the sample tube (Ø 38 mm), and scanned with micro-CT (μCT40, Scanco Medical, Brttisellen, Switzerland) according to our established protocol[242]. The scan range was set at 10 mm (650 slides) and the fracture line was set in the middle of this range. The resolution was set to 16 μm per voxel and 1024×1024 pixels. The region of interest (ROI) was selected from 2D images with a standardized threshold (>165) as a mineralized tissue. 3D reconstruction of the mineralized tissue was performed according to our established protocol. A low pass Gaussian filter (Sigma=1.2, Support=2) was used for 3D reconstruction. Different thresholds were to distinguish old cortical bone and low and high density mineralized tissue in the callus. Analyses of bones with low density (<165) and bones with high density (>165) were performed in order to distinguish newly formed bone from old cortical or laminar bone. Our quantitative analysis included all 650 2D image slides. The morphometric parameters evaluated were total bone tissue volume (TV), high-density bone volume (BV), the BV/TV ratio, callus TV density, callus BV density, and ρ-MOI. The average for each group was recorded.

**Biomechanical Testing:** 4-point bend testing was performed using an established protocol reported previously[242] with a mechanical testing machine (H25KS Hounsfield Test Equipment Ltd. Redhill, Surrey, UK). Only groups at week 12 were subjected to mechanical testing. The femora (n=8 for each group per time point) were placed 26 mm apart in an anterior-posterior direction on the lower supporting bars, and on the upper bars at 10 mm apart, flanking the fractured callus. A compression

load was applied at a rate of 5 mm/min until failure. The final load, energy, and stiffness were derived from the load–deformation curve built into the software software (QMAT Professional Material testing software. Hounsfield Test Equipment Ltd. Redhill, Surrey, UK). (Figure 5.2.5)

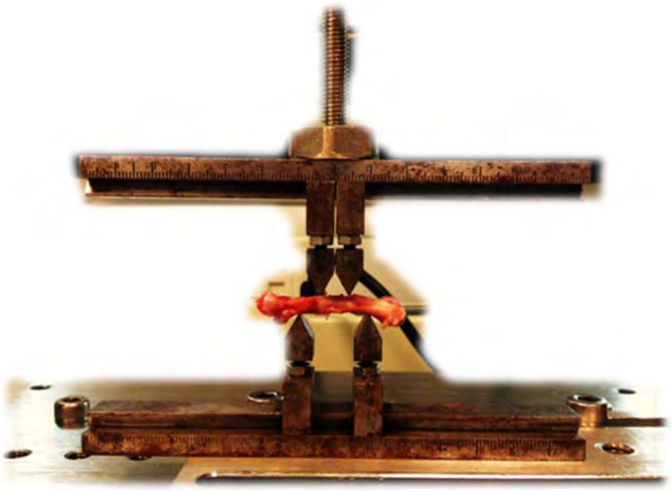

**Figure 5.2.5.** 4-point bending testing for fracture samples. The femur was placed with anterior-posterior direction on lower supporting bars at 26 mm apart, and the upper bars at 10 mm apart, flanking the fracture callus. A compression load was applied at a rate of 5 mm/min until failure.

**Histomorphometry analysis:** For our analysis of undecalcified histology, undecalcified samples were embedded into methylmethacrylate (MMA) and cut sagittally with a microtome saw (Leica SP1600, Leica, Germany) into sections with a thickness of 200 µm each. The sections were ground, polished to 100 µm, and observed under a fluorescence microscope (Leica Q500MC, Leica, Germany). Sequential fluorescence labeling according to our established protocol was used to study the dynamics of bone remodeling during fracture healing. L5 (calcein green) and CY5 (xylenol orange) filters were used to visualize the areas of new bone that were now labeled with the fluorochromes. For calculating the temporal change in new bone formation, the area 5mm proximal and 5mm distal to the fracture was chosen as the region of interest (ROI). The ratio of the area labeled with xylenol orange to that

labeled with calcein green was determined at the callus site using Image J (version 1.42q, NIH, USA). For decalcified histology, femora were fixed with buffered formalin (4%, overnight) and decalcified with 10% formic acid for 4 weeks. Then the samples underwent ethanol and xylene dehydration and were embedded into paraffin. 6μm thin sections were sliced and subjected to Hematoxylin and Eosin (H&E) and Safranin O staining for evaluation of the fracture calluses under a light microscope (Zeiss Aixoplan with Spot RT digital camera, Zeiss, German). The composition of the calluses was determined using Image J (version 1.42q, NIH, USA) for evaluation of the bone tissue area fraction, cartilage tissue area fraction, and fibrous tissue area fraction. A polarized light image was applied to analyze the collagen birefringence arrangement in the decalcified sections. Two polarized light filters were placed between the light path and viewing objective. For each tissue section, polarizing filters were rotated until the maximum birefringence was achieved as confirmed by the resulting 10× image capture.

## 5.3 Results

### 5.3.1 Design of intramedullary nail
### 3D drawing and FEA analysis

The vent in the middle site of the needle had three kinds of designs: 1) A unilateral window with a depth of 1/2 the needle's outer diameter; 2). a unilateral window with a depth of 1/3 the needle's outer diameter; and 3) regular interlacing holes with diameters of 0.5mm crisscrossing the needle's surface (with a total of 18 holes distributed in lengths of 1cm).

At first, we designed the unilateral windows as Mg ion releasing vents in the middle site of the needle with a depth of 1/2 the needle's outer diameter. The window was a semi-round cutting with a length of 5mm, an outer diameter of 1.27 mm, and an inner diameter of about 0.9 mm. The releasing area of the vent was about 4.5 square millimeters (Figure 5.2.1). This nail design was our initial attempt to fix the rat femur fracture, and its vent provided a large area to release Mg ions during degradation. Unexpectedly, the nail broke after four weeks of fixation in vivo (Figure 5.3.1). The inferior mechanical sustainability of the initial design was due to the stress concentration at the vent site, and the nail was also broken at the vent site. This inspired us to rethink the design pattern of the vent: basically, the stress at the vent site needed to be dispersed, so we designed two alternate nail drawings with different vent patterns in SolidWork. To keep the vent area wide enough for Mg ion release in vivo, the area of these alternate of vents was very close to that of the initial design. (Figure 5.2.1)

To select the optimal nail from our three designs, their stress bearing properties were evaluated in FEA. After a virtual load was applied in the software, the nail was deformed with a distinguished stress state at the vent site. Colors ranging from blue to

the red represented the growing stress at the vent site in the report images, with the warmer color showing more stress at the vent site. Our results indicated that the needle with regular interlacing holes (at a diameter of 0.5mm crisscrossing the needle's surface) had the least stress tension at the middle site, just as the intact needle did. Although the unilateral window with a depth 1/3 the needle's outer diameter significantly reduced the stress tension compared to the window with a depth 1/2 the outer diameter's design, its bearing was still very high compared with that of the intact needle. The results were grouped into middle site bearing strength and lateral site bearing strength and revealed that both middle and lateral site bearing were greatest with a needle that had a depth 1/2 the outer diameter's design; the needle with a depth 1/3 the outer diameter design was less but still high compared to the intact needle. The needle with regular interlacing holes (at a diameter of 0.5mm crisscrossing the needle's surface) showed almost no difference from the intact needle. This meant that the design with regular interlacing holes had the most advanced mechanical properties compared with the other two designs. (Figure 5.3.1)

**Degradation of Mg pin encapsuled in the nail *in vitro***

It was difficult to detect the amount of Mg ions released from the needle vent *in vivo*. However, we could evaluate Mg pin degradation in the medium *in vitro* to mimic its in *vivo* performance. An Mg pin was inserted into the needle canal and the two tips of the needle were sealed. This ensured that the Mg ions could only be released from the vent. The results indicated that the needle encapsulated Mg pin degraded as fast as the naked Mg pin *in vitro*, and there was no difference between them in the first month. At month 2, the needle encapsulated Mg pin soaked in the medium slightly increased the Mg concentration compared to the soaked medium containing naked Mg. This may have been due to the electrochemical reaction at the interface between the Mg

metal and the stainless steel needle. The Mg concentrations of the extracting medium with needle encapsulated Mg was 1.2 times the medium with naked Mg at month 2. This result indicated that the degradation of the Mg pin was not affected after it was encapsuled into the nail, proving that the designed intramedullary nail was suitable for carrying the Mg pin in the bone fracture fixation. (Figure 5.3.2)

### 5.3.2. Mg accelerated fracture healing in OVX rats
### X-ray photography results

A series of representative lateral X-ray radiographs of the same rat at weeks 0, 2, 4, 6, 8, and 12 were collected for comparison. Radiographs at these time points showed a faster healing process in the Mg treatment group than in the control. At week 2 post-surgery, the callus gaps in the Mg treatment group showed a smaller size than those in the control group. At week 4 post-surgery, the fracture was almost bridged by the mineralization of the callus in the Mg treatment group, with the minor appearance of callus gaps. In the control group, the callus gaps were retained at the fracture site. According to our X-ray radiography, the bone callus grew faster in the Mg treated group and the callus size was also bigger than those in the control femurs. (Figure 5.3.3)

Around the fracture site, an obvious radio-opaque external callus was observed from week 2 to week 8 after surgery in both groups. Early in week 2, the Mg treated fracture had a larger callus width and area than the control fracture. After week 2, the callus gap began to reach Radiographic healing, but not all the femurs reached the Radiographic healing. At week 4, 100% (12/12) of the control rat femurs showed no gap closure in our radiographic pictures. While the Mg treated rat femurs showed little non-healing rate, about 91.6% (11/12) of the Mg treated rats did not reach

radiographic healing. At week 8, 62.5% (5/8) of the Mg treated rats reached radiographic healing. The control group showed a 33.3% (3/9) radiographic healing rate at this time point. At week 12, almost all the Mg treated fracture femora reached radiographic healing (87% of 7/8), but the control group still had 4 femora that did not (55.5% of 5/9).

We also calculated callus width and callus area. The results indicated that Mg treated femurs had larger callus widths and areas than the control femurs. At week 2, the Mg treated group was 1.2 times larger in the callus area and its callus width was 1.1 times larger than the control group. At week 4, the callus area of the Mg treated group was 1.3 times higher than the control group, and the callus width was 1.2 times that of the control group. At weeks 6, 8, and 12, there was no significant difference in the callus area between the Mg treated group and the control group. There was no significant difference between the callus widths of the two groups at week 12. This showed that the callus area was growing from week 2 to week 6, and that it began to decrease from week 4 to week 12 in the control group, while the callus area of the Mg treated group reached its peak at week 4 and decreased by week 12. In X-ray radiography, there was almost no difference between the Mg treated group and the control group at the week 12. (Figure 5.3.4)

**Micro-CT results**

A Micro-CT scan at 5 mm midshaft above and down the fracture line was performed, and a series of 560 slices representing the 10 mm long fracture bone were included in our analysis. In Micro-CT scan, high-density bone was defined as that above a threshold of 165, which represented the old cortical and lamellar bone. A threshold below 165 was defined as lowly mineralized bone or newly formed bone. (Figure 5.3.5)

The total bone volume (TV) of the callus included all the scanned pixels covering the tissue above and below the threshold of 165. Bone volume (BV) indicated high-density bone tissue with pixels above the threshold 165. Mg treated fracture bones showed significantly high TV than the control group at week 4. At week 4, the TV of the Mg treated bone was 1.3 times that of the control group. At weeks 8 and 12, there no significant difference in the TV of the Mg treated group and the control group. We observed that the total volume of the calluses in the Mg treated group increased from week 2 to week 4, then the callus TV of the Mg treated group decreased at weeks 8 and 12. It sloped to the lowest point at week 12. However, the total volume of the calluses in control group grew from week 2 and reached a peak at week 4, leveling at weeks 8 and 12 without sloping until week 12.

We also compared the high-density bone volume of the calluses and found there was no significant difference in BV between the two groups at weeks 2, 8, and 12. At week 4, the highly mineralized bone volume of the calluses in the Mg treated group was 1.2 times that the control group, showing an almost 20% increase compared to the control group. This highly mineralized bone volume in the Mg treatment group was consistent with the total callus volume at weeks 2 and 4, but not at weeks 8 and 12. After it reached a peak at week 4, it decreased by weeks 8 and 12. In addition, the highly mineralized bone volume of the control group decreased from week 2 to weeks 4 and 8 and then increased by week 12. At week 12, the highly mineralized bone volume between the two groups had no significant differences at all.

BV/TV (the proportion of highly mineralized bone volume to total callus volume) corresponded to the above two parameters. The BV/TV of calluses in the Mg treated group was significantly lower (0.8 times in both weeks 2 and week 4) than in the control group. There was no significant difference in BV/TV between the two groups

at weeks 8 and 12. The BV/TV of the Mg treated group increased from weeks 2 to 4, reaching a peak at week 12. However, the BV/TV of the control group showed a slight decrease from week 2 to week 8, after which it began to grow and reached its peak at week 12. (Figure 5.3.6)

ρ-MOI (ρ moment of inertia, mm^4) determined the rigid body torque that was needed for the desired angular acceleration when it rotated along an axis. The bigger the ρ-MOI, the more inertia the rigid body had[243,244]. In our study, ρ-MOI was considered a parameter reflecting fracture bone rigidity. Since the bone shaft's mechanical properties partly depend on the shaft diameter and its mass, ρ-MOI was used to mirror the bending resistance of the shaft. According to our results, Mg treated fracture bone calluses had a higher ρ-MOI at week 4, showing an almost 50% increase (1.5 times) over that of the control fracture bones. This indicated that Mg treated fracture bones had better mechanical strength than the control fracture bone at week 4. However, there was no significant difference between two groups at weeks 2 and 8. While ρ-MOI was a theoretical parameter used for estimating the mechanical strength of the fractured bone shaft, the gold standard for measuring mechanical properties is still biomechanical testing. (Figure 5.3.7)

No significant difference in Callus BV density between the control group and the Mg treated group was shown at weeks 4 and 12. The Callus TV density of the Mg treated group was nearly 20% lower than that of the control group at week 4. However, the callus TV density of the Mg treated group was 1.1 times higher than that of the control group at week 12. This indicated the presence of more mineralized bone tissue in the Mg treated group than the control group. Also at week 12, biomechanical testing of the fractured bones showed that the ultimate load of the Mg treated fracture bone was about 30% higher than that of the control group, indicating that fracture

bones after Mg treatment had a better mechanical performance compared with the control group at week 12. (Figure 5.3.8)

**Histomorphometry analysis**

All the samples had callus formation, intramembranous ossification, and endochondral ossification in the fracture healing process. In our H&E staining images, more periosteal woven bone and intramembranous ossification were formed in the Mg treated bone than the control at week 2. Numeral hematogenous basophilic cells were aggregated in the cavities of the periosteal woven bone in the Mg treated fracture bone, indicating a stronger inflammatory response triggered in the Mg treated fracture bones than the control at week 2. Meanwhile, the presence of more periosteal woven bone in the Mg treated group indicated stronger intramembranous ossification in that group compared with the control. At week 4, the cartilaginous tissue began endochondral ossification and more wide cartilage tissue was observed in the Mg treated fracture bones. This indicated more active endochondral ossification in the Mg group than in the control group. At weeks 8 and 12, woven bone replaced the cartilage at the fracture callus gap. After that, the woven bone was replaced by lamellar bone and eventually began bridging with continuous osseous tissue in most of the fracture bones. At this stage, the Mg treated bone had more woven bone at the fracture site than the control group at week 8 and more uniform osseous bridging than the control group at week 12. (Figure 5.3.9)

In our Safranin O staining images, Safranin O positive red staining was observed at the fracture site of the bones at week 4 and 8. The Mg treated fracture bones showed a wider red staining area in callus tissue than in the control bone group, indicating more cartilage tissue with mature glycoprotein in the Mg treated bone. At week 8, red staining still was observed in the control bones at the fracture sites. However, this was

hardly observed in the Mg treated bone, indicating that the endochondral ossification process in the control group lagged behind that of the Mg group. (Figure 5.3.10)

New bone formation was evaluated using sequential labeling with fluorescent dyes in undecalcified bone sections. Representative fluorescent micrographs of the fracture bone sections showed xylenol (red) and calcein (green) labels at weeks 4, 8, and 12. We observed that newly formed bone at the fracture callus in control group grew from week 4 and reached a high volume at week 8, which then diminished by week 12. However, the Mg group showed a significant amount of newly formed bone at week 4, decreasing at weeks 8 and 12. By horizontal comparison, more new bone was formed in the Mg group than the control group at week 4. There was no significant difference in newly formed bone volume between the two groups at week 8. At week 12, however, the Mg group showed less fluorescent staining than the control group. This indicated a faster bone-remodeling rate in the Mg group than the control group. (Figure 5.3.11)

Circularly polarized light images of the Mg treated and control fracture calluses displayed regions with oriented collagen fibers, indicating lamellar bone organization. At week 2, the callus collagen arrangements in both the Mg group and control groups were disordered, as the polarized light image displayed a chaotic light filament. At week 4, both of the groups displayed regular collagen arrangements at the lateral side of their calluses due to the calcified woven bone growing at the lateral site while cartilage at the middle site of the calluses was not yet calcified. However, Mg the treated group showed more bright fibers at the callus site than the control group at week 4. This indicated that more maturely arranged collagen was produced in the Mg group than the control group. At week 8, endochondral ossification was almost finished. Both groups showed bright and regular light fibers at the callus region, but

more bright fibers were observed in the Mg treated group than the control group. At week 12, new bone was remodeled at the fracture site and transformed from woven to lamellar bone. Our image showed that more bright fibers and regular lamellar bone were observed in the Mg group than the control group, indicating better lamellar bone formation and mechanical properties in the Mg treated samples compared to the control samples at week 12. (Figure 5.3.12)

Our quantitative analysis of bony callus fractions and cartilaginous fractions were based on H&E and Safranin O staining images. Bony callus fraction indicated the ratio of bony area to total callus area; cartilaginous callus fraction indicated the ratio of cartilage area to total callus area. Bony fractions in both groups increased from week 2 to week 12. The Mg treated group showed significantly lower bony fraction than the control group at week 4 and higher bony fraction than the control group at weeks 8 and 12. However, cartilaginous callus fractions in the Mg treated group were higher than the control group at week 4 and lower than the control group at weeks 8 and 12. The cartilaginous callus fractions of the two groups both decreased from week 2 to week 12. (Figure. 5.3.13)

According to our fluorescent staining, the ratio of new bone formation at the callus site indicated the dynamics of callus bone formation. This was the ratio of the area labeled with xylenol orange to the area labeled with calcein green. The results showed that callus bone formation in the Mg treated group was most active at week 8 and decreased at week 12. However, callus bone formation in the control group increased by week 12, indicating a lagging bone formation process in the control group compared to the Mg treated group. (Figure. 5.3.14)

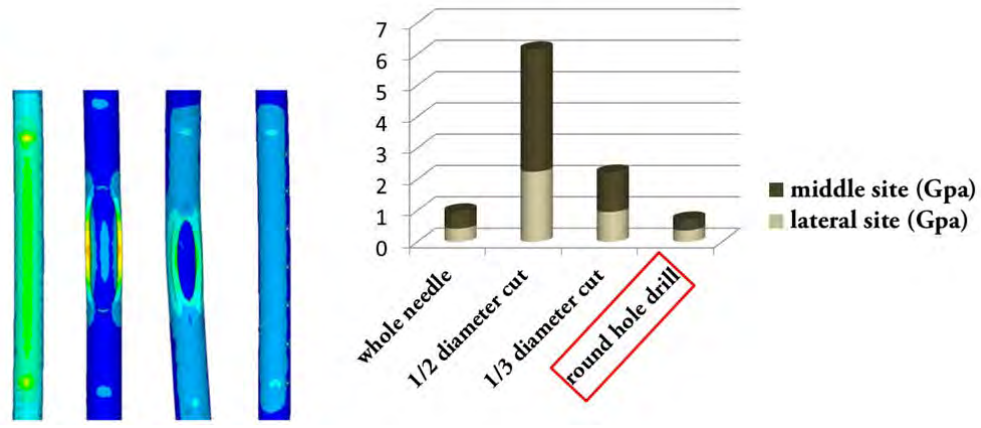


**Figure 5.3.1.** Mechanical simulating testing in FEA, bearing stress at the middle and lateral sites of the vent, as indicated by color. From cold to warm, the color represented bearing stress from small to large. The bearing stress of the middle and lateral sites were analyzed in the histogram. The vent of hole design (in the red pane) was the optimal choice.

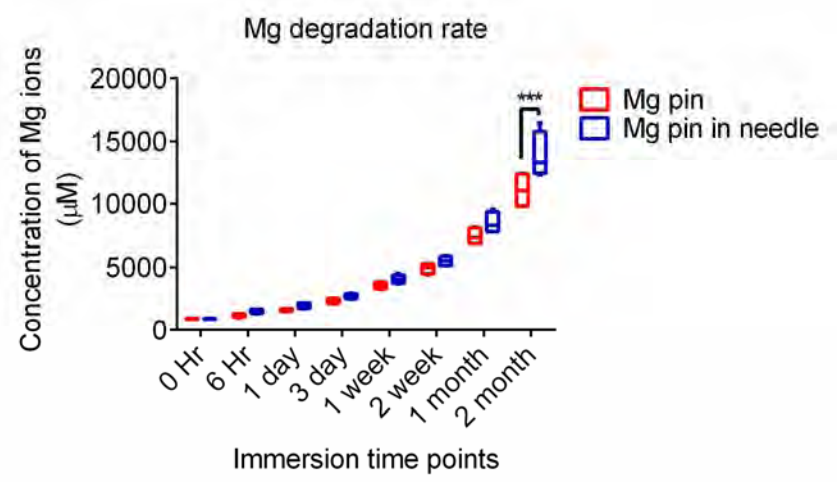


**Figure 5.3.2.** An Mg pin was inserted into the designed needle and its two tips sealed. Needles with Mg pin were immersed into the medium for 2 months. Mg elemental concentrations of the medium at eight time-points were analyzed by ICP-OES in each group (n=3). All values are given as the mean ± S/D. A two-way ANOVA was performed between groups, and significant differences were defined as: ***p< 0.001.

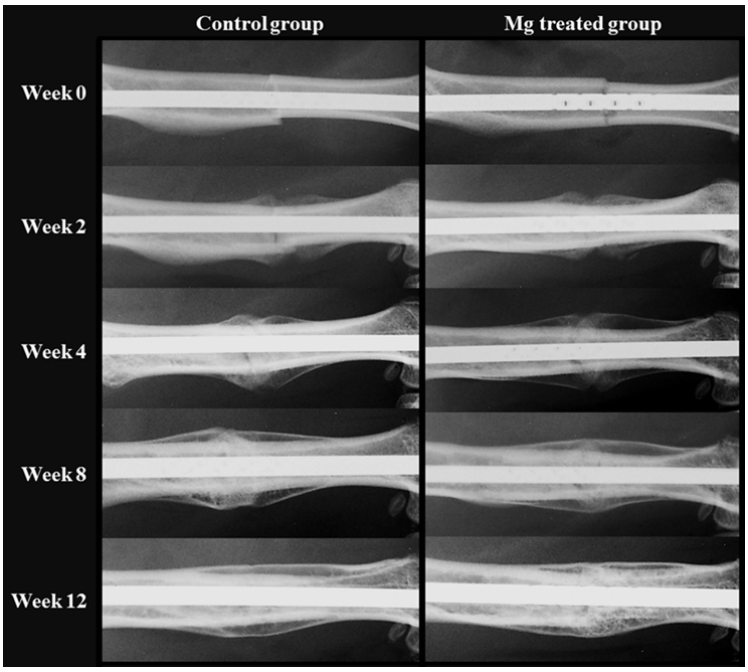


**Figure 5.3.3.** Representative X-ray photography images of femur fracture in the control sample (left side) and the Mg treated sample (right side) at weeks 2, 4, 6, 8, and 12.

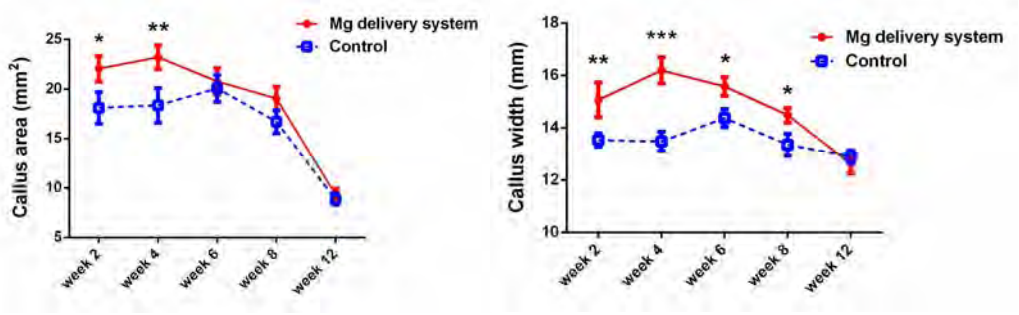


**Figure 5.3.4.** Callus area and callus width of the two groups from weeks 2 to 12 were analyzed. Significantly higher callus areas and callus widths were observed in the Mg treated group at week 4. The difference vanished at week 12. n=6 for each group at each time point. A two-way ANOVA was performed between groups. All values are given as the mean ± S/D. Significant differences were defined as: *p<0.05, **p<0.01, and ***p< 0.001.

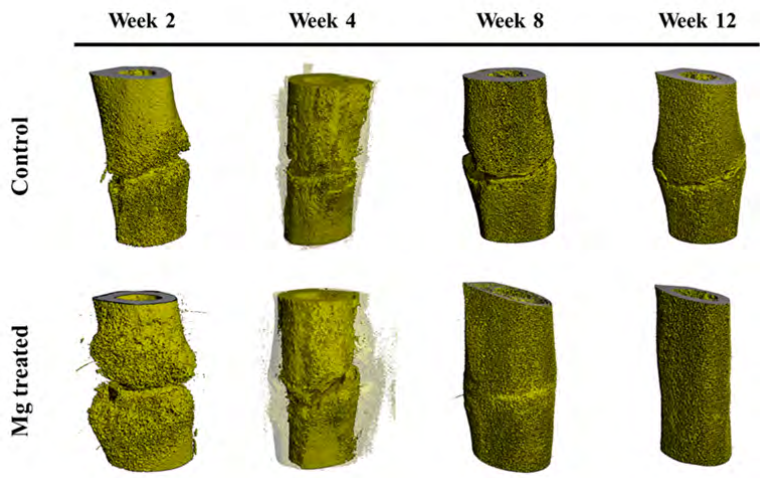


**Figure 5.3.5.** Representative 3-dimensional image of the fracture callus of the control sample (above) and the Mg treated sample (below) at weeks 2, 4, 8, and 12. The callus volume of the Mg treated group was more than that of the control group at weeks 2 and 4. There was no significant difference between the two groups at week 12.

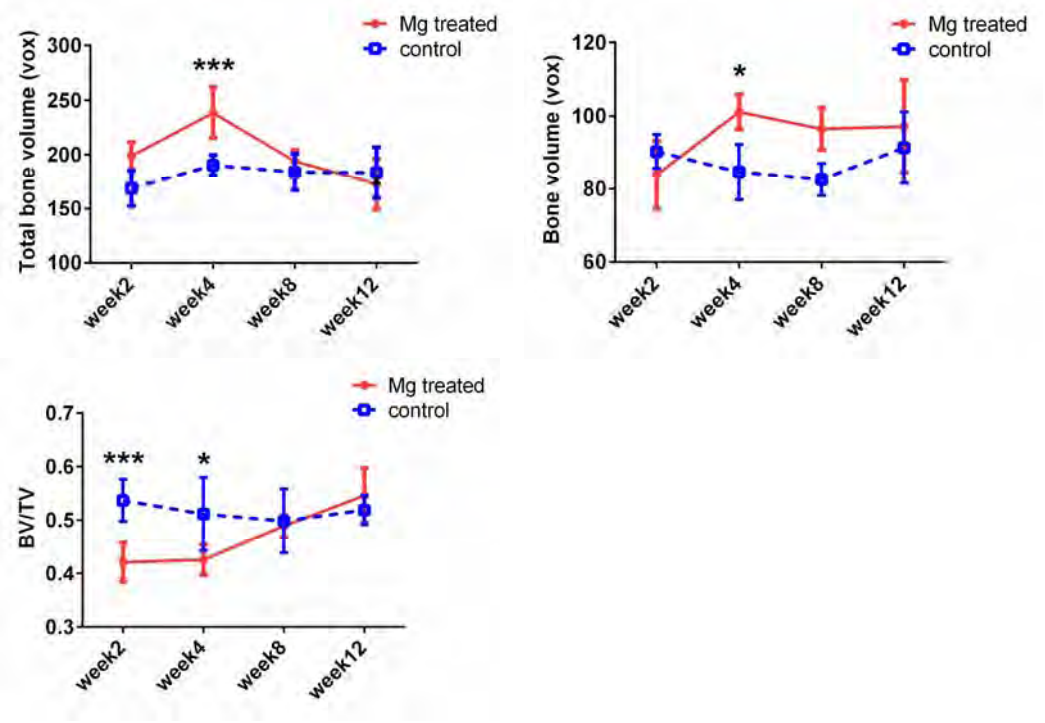


**Figure 5.3.6.** Total callus bone volume (TV), high-density callus bone (BV), and BV/TV as measured by micro-CT at weeks 2, 4, 8, and 12. Significantly higher TV, BV, and BV/TV were observed in the Mg treated group at week 4. A two-way ANOVA was performed between the groups. n=6 for each group at each time point. All values are given as the mean ± S/D. Significant differences were defined as: *p<0.05, **p<0.01, and ***p< 0.001.

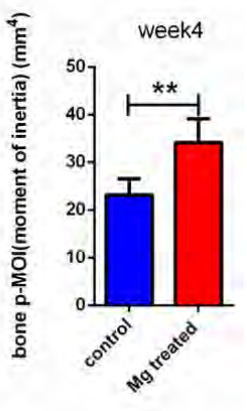


**Figure 5.3.7.** ρ-MOI of the fracture calluses of two groups analyzed by micro-CT at week 4. The Mg treated group was significantly higher than the control group. A Student's t-test compared the two groups. n=6 for each group at each time point. All values are given as the mean ± S/D. Significant differences were defined as: *p<0.05, **p<0.01, and ***p< 0.001.

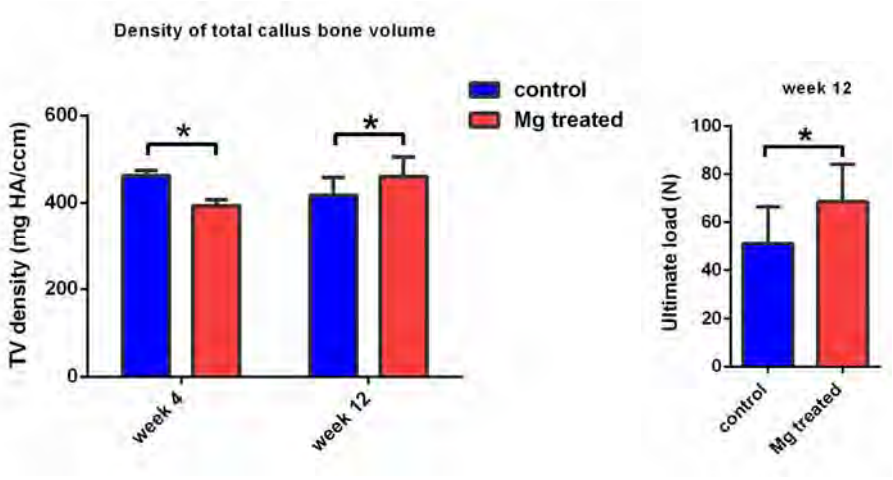


**Figure 5.3.8.** Callus TV density in the two groups at weeks 4 and 12 were represented in first two column graphs. TV density of the Mg treated group was significantly higher than the control group at week 12. The TV Ultimate load by mechanical testing was represented in the last column graphs. The ultimate load of the Mg treated group was significantly higher than the control group at week 12. A Student's t-test compared the two groups. n=6 for each group at each time point in TV/BV density analysis. n=8 for each group at each time point in the ultimate load analysis. All values are given as the mean ± S/D. Significant differences were defined as: *p<0.05, **p<0.01, and ***p< 0.001.

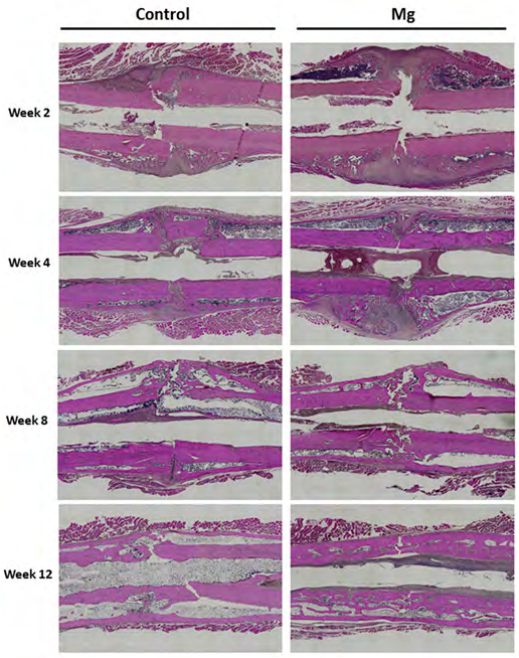


**Figure 5.3.9.** Histomorphological analysis of midsagittal section of healing femoral shaft fracture (6µm) stained with H&E (5×). The callus gap was wider in the Mg treated group than the control group at weeks 2 and 4. No significant difference was observed between the two groups at weeks 8 and 12.

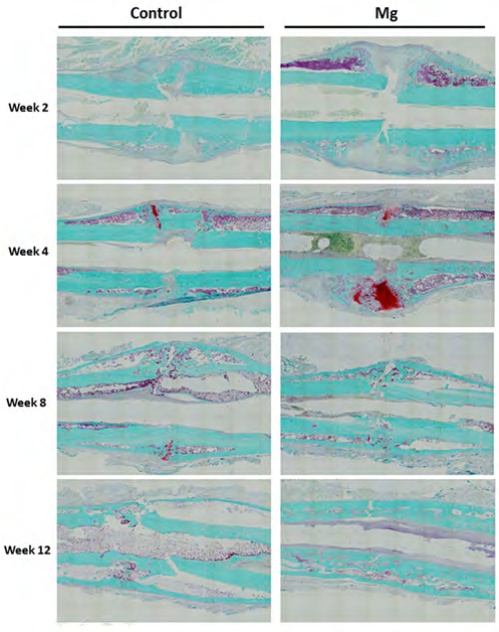


**Figure 5.3.10.** Histomorphological analysis of midsagittal section of healing femoral shaft fracture (6µm) stained with Safranin O (5×). Cartilaginous tissue (red staining) in the callus gap was more in the Mg treated group than in the control group at week 4. Less cartilaginous tissue (red staining) in the callus gap was observed in the Mg treated group than the control group at week 8.

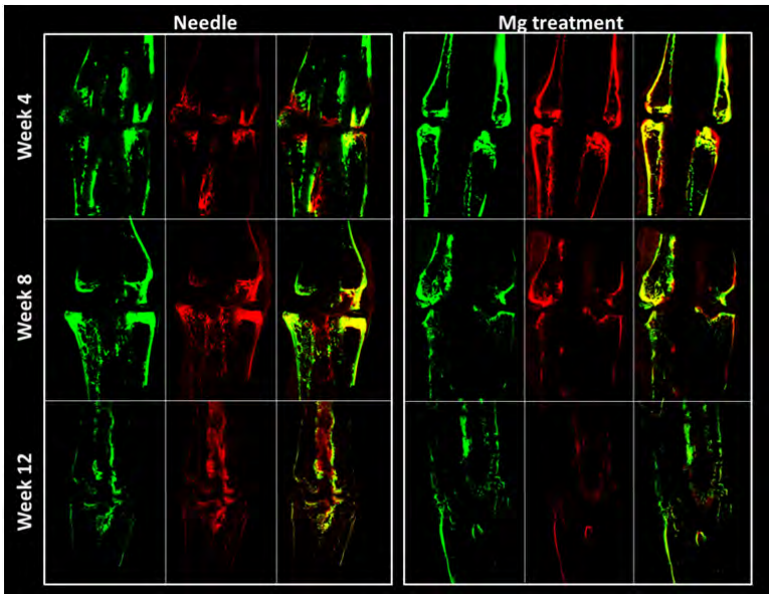


**Figure 5.3.11.** Fluorescence microscopic image with two fluorescent labels: calcein green (green light) and xylene orange (red light). Fracture samples (100μm) at weeks 4, 8, and 12 from the control group (needle) and the Mg treated group (Mg delivery system) were stained (20×). New bone formation in the Mg treated group reached its peak at week 4 and decreased at week 12. The most active new bone formation in the control group was at week 8. It indicated that new bone formation in the Mg treated group was faster than in the control group over the healing term.

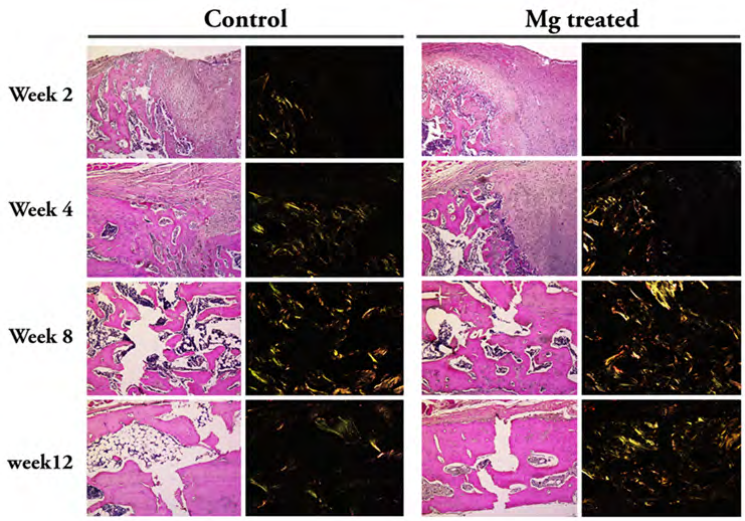


**Figure 5.3.12.** H&E staining and polarized light analysis of callus in the midsagittal section of the healing femoral shaft fracture (100×). Collagen fibers in the Mg treated group showed more regular arrangement than those in control group at weeks 8 and 12. This indicated that more lamellar bone was formed in the Mg treated group at week 12.

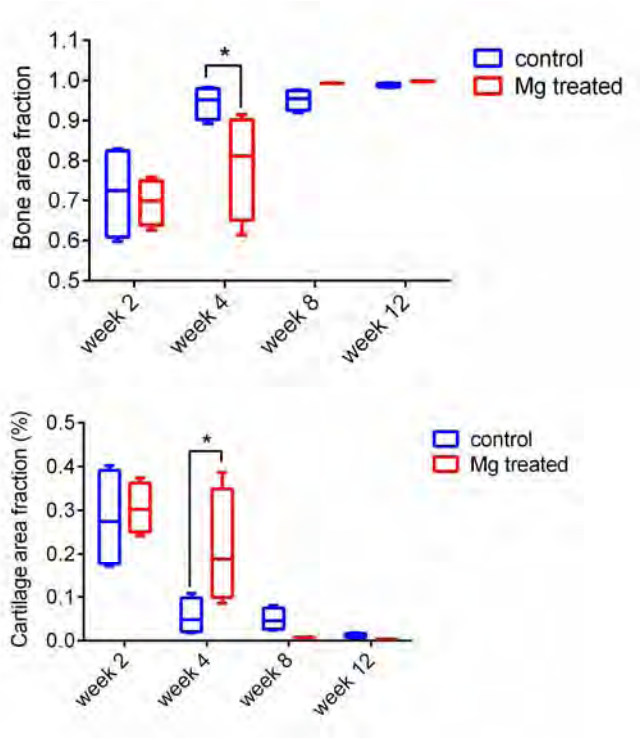


**Figure 5.3.13.** Fraction of bony tissue (above) and cartilaginous tissue (below) compared to total calluses of the control and Mg treated groups at weeks 2, 4, 8, and 12. Quantitative data were based on H&E and Safranin O staining images. Both fractions had significant difference at week 4. n=6 for each group at each time point. All values are given as the mean ± S/D. A two-way ANOVA was performed between groups, significant differences were defined as: *p<0.05, **p<0.01, and ***p< 0.001.

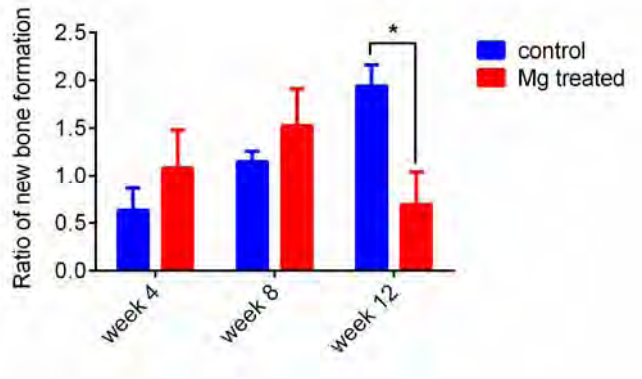


**Figure 5.3.14.** Dynamics of bone formation in the control and Mg treated groups at weeks 4, 8, and 12. Quantitative data were based on fluorescent images. The Mg treated group showed a significantly lower ratio of new bone formation compared with the control group at week 12. n=6 for each group at each time point. All values are given as the mean ± S/D. A two-way ANOVA was performed between groups, significant differences were defined as: *p<0.05, **p<0.01, and ***p< 0.001.

## 5.4 Discussion

Pure Mg is rarely used in fracture repairs due to its low strength and fast degrading rate[245]. Here, we designed an intramedullary nail with a vent at the middle site of the needle. We inserted a pure Mg pin into the needle and utilized Mg ions' bioactive effects to have them exactly release to the fracture line. Our initial design of a unilateral window with a depth of 1/2 the needle's outer diameter was too weak to fix the fracture bone and broke between weeks 4 and 6 after initial fixation. To ensure that the vent would have ample area for Mg ion to release and simultaneously have sufficient bending strength, we chose a design with cruciatedly interlacing holes, applying FEA results, as it possessed the best mechanical performance. Our mechanical test proved that the vent design with real cruciatedly interlacing holes was actually as strong as the intact manufactured needle. We inserted the Mg pin into the needle and sealed its two tips, then put it into the medium to evaluate Mg degradation and Mg ion release *in vitro*. Our results indicated that the Mg degradation rate of the needle capsuled Mg pin was very close to that of the bare Mg pin, which meant that our design had no constriction to Mg pin degradation. At month 2, the Mg ion concentration extracted from the medium immersed with the encapsuled needle was 27% higher than the medium with a bare Mg pin. This might be due to the electrochemical effect between the Mg and the steel interface. This part of our results proved the feasibility of our needle for bone fracture repair since this novel design meant that the soft Mg metal could be directly used in the fracture model. (Figure 5.3.2)

Based on the results in chapter 2, the effect of Mg induced new bone formation was an intramembranous ossification that was mainly dependent on the periosteum stimulation, including neuropeptides (ex. CGRP) and the differentiation of MSCs. In

our X-radiography results, fracture calluses in the Mg treated group showed significantly broad intramembranous hard callus lines compared to the control group at weeks 2 and 4. Soon after the fracture, MSCs from periosteum and bone marrow were recruited into the fracture site and differentiated into the osteoblasts. This intramembranous ossification process happened as early as the first week after the fracture, during which term inflammation cytokines with neuropeptides were integrated into the intramembranous ossification. Mg had an obvious osteogenic effect in this period of time. We observed significantly larger callus areas and widths in the Mg treated group compared to the control groups at weeks 2 and 4. The ratio of callus bridging was higher in the Mg treated fracture bone than in the bones of the control group at weeks 4, 8, and 12. This callus bridging was dependent not only on intramembranous bone formation, but also on a endochondral ossification process. The un-bridging site was filled with cartilaginous tissue when endochondral ossification was not finished. Intramembranous ossification and endochondral ossification were both observed to be faster in the Mg treated group than in the control group, which accounts for the faster callus bridging in the Mg treated fractures. The slow callus bridging indicated a long process of endochondral ossification and remodeling at the bone fracture site in the control group. In Wing-Hoi Cheung's study, the callus area and width were larger in LIPUS treated fractures than in a control only at weeks 2 and 4 but the difference diminished at week 8. This fracture healing trend was similar to the observations in our study, indicating that Mg accelerated bone fracture healing is similar to physical treatment.

Our Micro-CT results showed a similar trend to our X-ray results. The TV of the Mg treated group showed an increase from week 2 to week 4. It then decreased at weeks 8 and 12. There was a rapid and transient hematoma phase and inflammation within 24

hours after the fracture. The inflammation led to the destruction of existing osseous tissue at the fracture bone tips, and this turned the bone debris to hematoma granules. Between weeks 2 and 4 after fracture, hematoma granulation was first enriched with mesenchymal stem cells and inflammatory cells and then replaced by cartilage tissue. Over this period, total callus volume was increased both in the control fracture bones and the Mg treated fracture bones. However, new mineralized bone (BV) decreased in the control fracture bones from weeks 2 to 4 due to osteolysis in the early inflammatory phase, and the destroyed osseous tissue was replaced with newly formed cartilage tissue. By contrast, there was a significant increase of BV at week 4 in the Mg treated group. As we discussed earlier, Mg's osteogenic effect was periosteal bone formation, so the increased BV was mainly derived from vast intramembranous ossification. With double-labeled fluorescence staining, newly formed dense green and red stained osseous tissue was observed at a lateral callus site but not at the middle site (there was cartilage tissue at the middle site of the callus) in the Mg treated group at week 4. Endochondral ossification was finished at weeks 8 and 12. In this period, the cartilage tissue ossified to the woven bone. Meanwhile, the ossified intramembranous woven bone was decreased and reformed to create a more regular lamellar bone. So, the BV in both the control and Mg groups decreased from week 4 to week 8, then it increased after the bone remodeling process. This evolution of TV and BV in the fracture repair matched our observation of histomorphological analysis in H&E staining and Safarnin O staining. Double-labeled fluorescence staining proved that the bone fracture healing process was significantly accelerated in the Mg treated groups compared with the control group. A polarized light image showed that more regular collagen fiber appeared at the end of healing period in the Mg treated group than in control group, which indicated that better remodeling with

more lamellar bone and mechanical properties were achieved in the Mg treated group. Biomechanical testing proved that the ultimate load of the Mg treated bone was 1.3 times that of the control bone.

Of note, the callus area in the Mg-IMN group was significantly larger than in the IMN group at week 4, and then no difference was detectable at week 8 and 12, implying an enhanced bone remodeling in the Mg-IMN group at early healing phase. The faster ratio of new bone formation in Mg-IMN group at week 4 was represented by high fluorescent staining and BV quantification. The $Ca^{2+}$ chelating agent calcein green and xylenol orange only stained the free $Ca^{2+}$ which exiting as non-mineralized ACP. The richly stained osteoid area in Mg-IMN group at week 4 was matched with high BV in micro-CT scanning. At week 12, the thinly stained osteoid in Mg-IMN group represented a low ratio of new bone formation which indicated the finishing bone remodeling process compared to IMN-group. More importantly, because mineralization of HAP and lamella bone alignment are direct undertakers for mechanical strength of bone rather than osteoid in fluorescent staining and BV in micro-CT, the high BMD and well aligned lamella bone in Mg-IMN group indicated a better mechanical strength than IMN group. It was proved in biomechanical testing which showed that the ultimate load of the repaired bone was significantly higher in the Mg-IMN group, as compared to the IMN group. As previously reported, a role of Mg in the crystal structure of extracellular matrix together with better alignment of matrix collagen is the most likely explanation for this clinically relevant finding[246].

Considering that the amount of Mg applied in our study was relatively small, it was still hard to conclude that the long-lasting effects of Mg will always benefit bone fracture healing. If a high mass of Mg were applied to the fracture, could the bone remodeling process still be accelerated? We thought that there should be an optimal

dosage of Mg for fracture healing acceleration, but finding this requires exact calculations with a range of doses distributed over various test programs. Although both normal and osteoporotic bone fractures employed the same regenerative process, indicated above, previous studies have suggested that the capacity for bone healing and remodeling in osteoporotic fractures are reduced[247], probably due to the impairing of intramembranous ossification at an early stage and angiogenesis and osteoprogenitor cell recruitment in endochondral ossification[247].

Our study showed that Mg promoted stem cell recruitment and intramembranous ossification *in vivo*. With regard to angiogenesis, Bernardini D et al had already proven that low doses of Mg inhibited epithelia growth and migration while high doses of Mg significantly stimulated epithelia proliferation and migration and sensitized microvascular cells to migratory signals[245]. There are already many methods used for the treatment of osteoporosis and osteoporotic fractures, such as parathyroid hormone (PTH), bisphosphonates, estradiol, vitamin $D_3$, selective estrogen receptor modulators, calcitonin, and physical therapies such as low intensity pulsed ultrasound (LIPUS) [248-250]. However, drugs and physical therapy require long-term treatment after surgery, and these treatments are relatively high cost. Compared to drug administration and machine-enabled physical therapy, fixing Mg as a treatment material into the intramedullary nail at the surgery procedure was shown to be simple and cost-effective.

**In conclusion**, Mg metal as a direct fixed appliance in a bone fracture was not practical *in vivo*. Our design of an innovative intramedullary nail containing biodegradable and osteogenic Mg for fracture healing, however, was effective. This kind of design significantly accelerated optimized fracture healing in OVX rat models. Based on our study of Mg-induced osteogenic effects and their mechanisms, we

proved that Mg ions significantly enhanced synaptic replasticity in DRG neurons, which promoted synaptic vesicles containing the sensory neuropeptide CGRP to aggregate to the axon terminals for a massive release of stimulation. The Mg ion itself had an osteogenic effect on PDSC and BMSC differentiation. Considering that bone Mg content and sensory neuropeptides were decreased with age in animals, especially since the decreased sensory neuropeptides CGRP and substance P led to a significant delay in wound healing in aged rats[251], we found that we could use Mg metal as a bioactive material to accelerate bone fracture healing.

# **Chapter** 6

## General Conclusion
And
## Future Study

## 6.1 General Conclusion

Mg induced new bone formation at the periosteal region after it was implanted into the rat femur canal. This phenomenon was due to the direct effect of Mg ions on sensory nerve endings in femur periosteum and MSCs. On the one hand, Mg ion enhanced synaptic replasticity and promoted synaptic vesicles aggregated at the axon terminals in DRG neurons. The neuropeptide CGRP released from the nerve endings promoted osteoblastogenesis to MSCs in periosteum, forming new bone. On the other hand, the Mg ion itself induced osteogenic differentiation to MSCs. Mg ion's effects on neurons and MSCs were dependent on cytoplasmic Mg influx under extra-cellular high Mg conditions. This transmembranous Mg influx mainly occurred via the ion channel MagT1, which is ubiquitously expressed in eukaryocyte. We postulated that Mg metal could be used in osteoporotic fracture healing on account of its osteogenic effect. Since pure Mg metal was too soft to fix the fractured bone in rats, we designed a hollow intramedullary nail that contained an internal Mg pin to fix the bone fractures of OVX rats, and this Mg-containing intramedullary nail significantly accelerated and optimized femur fracture healing.

## 6.2 Limitations of the Study

The limitations of our study are mainly restricted to the technology we used in our cell studies and surgery:

**1.** In the surgery, we needed to replace the guiding nail with an intramedullary nail to fix the fractured bone after the closed bone fracture was made. The unavoidable surgery trauma to the fracture bone tips might have interfered with bone healing in our model.

**2.** In addition to Mg ions, hydrogen and hydroxyl were also produced during Mg

degradation. In our study, we did not explore the details effect of hydrogen and hydroxyl on bone fractures. According to other researches, hydrogen is beneficial to wound healing[252].

**3.** Mg could retard the growth of mineral crystals, making them short and tiny. This retarding of mineral crystal growth benefits bone mechanical properties, so the mineral crystal size and morphology of Mg treated fracture callus tissue should be detected by XRD.

## 6.3 Future studies

**1.** For this study, we screened out the cell membrane Mg ion channel MagT1 as an aprincipal channel for cellular Mg influx. However, our findings are just beginning to explain the deep mechanism of synaptic vesicle formation in neuron and osteogenic differentiation in MSCs under high Mg conditions. Since the osteogenic effect of Mg on MSCs had a common channel dependence with MagT1 and with Mg's replasticity to the neuron, we believed that Mg ion's effect on stem cells and neurons should occur through a conjunct mechanism based on myosin-actin system. That is the next step in our research direction for cytoskeleton cell biology.

**2.** In a recent experiment, we found that CD 3 positive T cells were clustered at the newly formed bone region in Mg implanted femur. The new, Mg-induced bone formation at the outer cortical region mostly disappeared when the Mg pin was implanted in the nude mice. This indicated that inflammation enrolled with T cells should be important to Mg-induced osteogenic effects. We postulated that the round story should integrate neuro-immune-osteogenesis in Mg induced osteogenic process. There must be connections with neurofactors, immunofactors and Mg. Considering

that many bone diseases were caused by a defect in the immune system, a thorough understanding of Mg-neuro-immuno interactions could provide a possible solution to bone diseases.

**3.** The application of Mg metal in rat fracture healing still requires further improvement. Since our ultimate purpose was to apply metal Mg to clinical practice, determining the optimum dose of Mg dose and its use modes will be our key points in future study.

The efforts for testing Mg-based implants in animal models and patients can be dated back to a century ago[2,253,254]. Extensive investigations from our multidisciplinary collaborations have recently reported a consistent phenomenon that Mg-based alloys/BMG can significantly promote bone formation *in vivo*[255-259]. However, to date, only one type of Mg-based implants is approved with official CE marking (https://www.gov.uk/ce-marking) for orthopedic application after completion of a small scale clinical trial over a period of 6 months in Germany, that is, an interference screw made of MgYREZr with higher corrosion resistance for the fixation of mild hallux valgus[260].

Commercial implants containing Mg and its alloys are already available in Germany (http://syntellix.de/en/) which selling the WE43 bone staple for the foot bone fracture fixation. Moreover, in 2014, the Korean scientists were undertaking the clinical trails or Mg-Zn-Ca alloy bone staple for the fixture of fractured hand bone. The creation of biodegradable metals is inspiring new research and offering great hope to clinicians, especially after improvements in glassy alloy technology have made Mg more relevant to the hospital bedside. Considering the osteoporotic fractures in aged people are sharply increasing in our nation, it need further exploration of effective treatment

besides conventional FDA-approved drugs including the bisphosphonates, calcitonin-salmon, denosumab (Prolia™), the estrogen agonist/antagonist raloxifene, estrogen/hormone therapy (ET/HT), as well as the anabolic agent teriparatide (Forteo™) to reduce fracture risk. Mg and its alloys used in fracture fixation need proper design to be applied in hip-neck fracture, lumber fracture and radius fracture et al. In the clinical field, the plate design rather than the degradation would be the key point in fracture healing.

More than that, the osteogenic effects, neural synaptic replastcity, and cardiovascular protections of Mg have made it a potential candidate for various treatments. To date, Mg ion (mostly $MgSO_4$ ) has been applied in the prevention of neuron damage in preterm-birth babies[261], to enhance learning and memory[230], to cure acute pancreatitis[262], to prolong the duration of analgesia after interscalene nerve blocking and reduce postoperative analgesic requirements [263,264], and to intravenously relieve acute stroke and lacunar infarct [265, ENREF 253][266]. Our study is the first to apply Mg as a medical treatment to enhance fracture healing. However, since hydroxyl, which is produced in Mg degradation, is harmful to cells and tissues, metal Mg needs to be refined before it is applied clinically. Our hope is that composite materials containing Mg will be developed for use in the field of orthopedics. We believe that Mg, whether metal or salt, will find multiple orthopedic applications, bringing us to continue seeking the best usage modality principles for Mg and for a better understanding of the mechanisms that drive Mg's biological activities.

## Funding Acknowledgement

This work was supported by the RGC, Hong Kong (Ref.No.:14112714, 14114415),

NSFC/RGC (N_CUHK449/13), Innovation and Technology Fund (ITS/350/13), Hong Kong RGC Collaborative Research Fund (CRF, C4028-14GF), and SMART Program, Lui Che Woo Institute of Innovative Medicine, Faculty of Medicine, the Chinese University of Hong Kong.

# References


1. Niinomi, M. Recent metallic materials for biomedical applications. *Metall Mater Trans A* **33**, 477-486 (2002).
2. Staiger, M.P., Pietak, A.M., Huadmai, J. & Dias, G. Magnesium and its alloys as orthopedic biomaterials: A review. *Biomaterials* **27**, 1728-1734 (2006).
3. Jacobs, J.J., Gilbert, J.L. & Urban, R.M. Corrosion of metal orthopaedic implants. *J Bone Joint Surg Am* **80A**, 268-282 (1998).
4. Jacobs, J.J., Hallab, N.J., Skipor, A.K. & Urban, R.M. Metal degradation products - A cause for concern in metal-metal bearings? *Clin Orthop Relat R*, 139-147 (2003).
5. Lhotka, C., Szekeres, T., Steffan, I., Zhuber, K. & Zweymuller, K. Four-year study of cobalt and chromium blood levels in patients managed with two different metal-on-metal total hip replacements. *J Orthopaed Res* **21**, 189-195 (2003).
6. Puleo, D.A. & Huh, W.W. Acute Toxicity of Metal-Ions in Cultures of Osteogenic Cells Derived from Bone-Marrow Stromal Cells. *J Appl Biomater* **6**, 109-116 (1995).
7. Songur, M., *et al.* Electrochemical corrosion properties of metal alloys used in orthopaedic implants. *J Appl Electrochem* **39**, 1259-1265 (2009).
8. Tritschler, B., Forest, B. & Rieu, J. Fretting corrosion of materials for orthopaedic implants: a study of a metal/polymer contact in an artificial physiological medium. *Tribol Int* **32**, 587-596 (1999).
9. Wang, J.Y., Wicklund, B.H., Gustilo, R.B. & Tsukayama, D.T. Titanium, chromium and cobalt ions modulate the release of bone-associated cytokines by human monocytes/macrophages in vitro. *Biomaterials* **17**, 2233-2240 (1996).
10. Hanawa, T. Metallic biomaterials and electrochemistry. *Electrochemistry* **71**, 799-804 (2003).
11. Witte, F. The history of biodegradable magnesium implants: A review. *Acta Biomater* **6**, 1680-1692 (2010).
12. Bushkin, B.I. & Vorontsov, A.V. [Comparative evaluation of conservative and operative methods of treatment of fractures in ionizing radiation casualties; experimental study]. *Ortopediia travmatologiia i protezirovanie* **19**, 13-16 (1958).
13. Niinomi, M. Recent research and development in metallic materials for biomedical, dental and healthcare products applications. *Mater Sci Forum* **539-543**, 193-200 (2007).
14. Salahshoor, M. & Guo, Y.B. Biodegradable Orthopedic Magnesium-Calcium (MgCa) Alloys, Processing, and Corrosion Performance. *Materials* **5**, 135-155 (2012).
15. Brar, H.S., Platt, M.O., Sarntinoranont, M., Martin, P.I. & Manuel, M.V. Magnesium as a biodegradable and bioabsorbable material for medical implants. *Jom-Us* **61**, 31-34 (2009).
16. Brar, H.S., Keselowsky, B.G., Sarntinoranont, M. & Manuel, M.V. Design Considerations for Developing Biodegradable and Bioabsorbable Magnesium Implants. *Jom-Us* **63**, 100-104 (2011).
17. Baghni, I.M., Wu, Y.S., Li, J.Q., Du, C.W. & Zhang, W. Mechanical properties and potential applications of magnesium alloys. *T Nonferr Metal Soc* **13**, 1253-1259 (2003).
18. Mordike, B.L. & Ebert, T. Magnesium - Properties - applications - potential. *Mat Sci Eng a-Struct* **302**, 37-45 (2001).
19. Nassif, N. & Ghayad, I. Corrosion Protection and Surface Treatment of Magnesium Alloys Used for Orthopedic Applications. *Adv Mater Sci Eng* (2013).
20. Zberg, B., Uggowitzer, P.J. & Loffler, J.F. MgZnCa glasses without clinically observable hydrogen evolution for biodegradable implants. *Nat Mater* **8**, 887-891 (2009).
21. Li, H.F., *et al.* In vitro and in vivo studies on biodegradable CaMgZnSrYb high-entropy bulk metallic glass. *Acta Biomater* **9**, 8561-8573 (2013).
22. Gu, X.N., Xie, X.H., Li, N., Zheng, Y.F. & Qin, L. In vitro and in vivo studies on a Mg-Sr binary alloy system developed as a new kind of biodegradable metal. *Acta Biomater* **8**, 2360-2374 (2012).
23. Gu, X.N., Zheng, Y.F., Cheng, Y., Zhong, S.P. & Xi, T.F. In vitro corrosion and biocompatibility of binary magnesium alloys. *Biomaterials* **30**, 484-498 (2009).

24. Gu, X.N., Zheng, W., Cheng, Y. & Zheng, Y.F. A study on alkaline heat treated Mg-Ca alloy for the control of the biocorrosion rate. *Acta Biomater* **5**, 2790-2799 (2009).
25. Gu, X.N., Zheng, Y.F. & Chen, L.J. Influence of artificial biological fluid composition on the biocorrosion of potential orthopedic Mg-Ca, AZ31, AZ91 alloys. *Biomed Mater* **4**(2009).
26. Gu, X.N., *et al.* Surface modification of an Mg-1Ca alloy to slow down its biocorrosion by chitosan. *Biomed Mater* **4**(2009).
27. Zheng, Y.F., Gu, X.N. & Witte, F. Biodegradable metals. *Mat Sci Eng R* **77**, 1-34 (2014).
28. Witte, F., *et al.* In vivo corrosion of four magnesium alloys and the associated bone response. *Biomaterials* **26**, 3557-3563 (2005).
29. Wagner, D.O. & Aspenberg, P. Where did bone come from? An overview of its evolution. *Acta Orthop* **82**, 393-398 (2011).
30. Glimcher, M.J., Bonar, L.C., Grynpas, M.D., Landis, W.J. & Roufosse, A.H. Recent Studies of Bone-Mineral - Is the Amorphous Calcium-Phosphate Theory Valid. *J Cryst Growth* **53**, 100-119 (1981).
31. Wheeler, E.J. & Lewis, D. X-Ray Study of Paracrystalline Nature of Bone Apatite. *Calcified tissue research* **24**, 243-248 (1977).
32. Brown, W.E. & Chow, L.C. Chemical Properties of Bone-Mineral. *Annu Rev Mater Sci* **6**, 213-236 (1976).
33. Termine, J.D. & Posner, A.S. Infrared Analysis of Rat Bone - Age Dependency of Amorphous and Crystalline Mineral Fractions. *Science* **153**, 1523-& (1966).
34. Olszta, M.J., *et al.* Bone structure and formation: A new perspective. *Mat Sci Eng R* **58**, 77-116 (2007).
35. Weiner, S. & Wagner, H.D. The material bone: Structure mechanical function relations. *Annu Rev Mater Sci* **28**, 271-298 (1998).
36. Voet, J.G. & Voet, D. Biochemistry and molecular biology education (BAMBEd). *Biochem Educ* **28**, 124-124 (2000).
37. Eppell, S.J., Tong, W.D., Katz, J.L., Kuhn, L. & Glimcher, M.J. Shape and size of isolated bone mineralites measured using atomic force microscopy. *J Orthopaed Res* **19**, 1027-1034 (2001).
38. Traub, W., Arad, T. & Weiner, S. Three-dimensional ordered distribution of crystals in turkey tendon collagen fibers. *Proc Natl Acad Sci U S A* **86**, 9822-9826 (1989).
39. Dey, A., *et al.* The role of prenucleation clusters in surface-induced calcium phosphate crystallization. *Nat Mater* **9**, 1010-1014 (2010).
40. Nudelman, F., *et al.* The role of collagen in bone apatite formation in the presence of hydroxyapatite nucleation inhibitors. *Nat Mater* **9**, 1004-1009 (2010).
41. Wang, L.J., Lu, J.W., Xu, F.S. & Zhang, F.S. Dynamics of crystallization and dissolution of calcium orthophosphates at the near-molecular level. *Chinese Sci Bull* **56**, 713-721 (2011).
42. Xie, B.Q. & Nancollas, G.H. How to control the size and morphology of apatite nanocrystals in bone. *P Natl Acad Sci USA* **107**, 22369-22370 (2010).
43. Wang, L.J. & Nancollas, G.H. Calcium Orthophosphates: Crystallization and Dissolution. *Chem Rev* **108**, 4628-4669 (2008).
44. Burnell, J.M., Teubner, E.J. & Miller, A.G. Normal Maturational Changes In Bone-Matrix, Mineral, And Crystal Size In the Rat. *Calcified tissue international* **31**, 13-19 (1980).
45. Cao, X., Harris, W.G., Josan, M.S. & Nair, V.D. Inhibition of calcium phosphate precipitation under environmentally-relevant conditions. *Sci Total Environ* **383**, 205-215 (2007).
46. Cao, X.D. & Harris, W. Carbonate and magnesium interactive effect on calcium phosphate precipitation. *Environ Sci Technol* **42**, 436-442 (2008).
47. Xu, N., *et al.* Mechanisms of phosphate retention by calcite: effects of magnesium and pH. *J Soil Sediment* **14**, 495-503 (2014).
48. Salimi, M.H., Heughebaert, J.C. & Nancollas, G.H. Crystal-Growth Of Calcium Phosphates In the Presence Of Magnesium-Ions. *Langmuir* **1**, 119-122 (1985).
49. Lee, T. & Lin, Y.C. Mimicking the Initial Development of Calcium Urolithiasis by Screening Calcium Oxalate and Calcium Phosphate Phases in Various Urinelike Solutions, Time Points, and pH Values at 37 degrees C. *Cryst Growth Des* **11**, 2973-2992 (2011).
50. Boskey, A. Bone mineral crystal size. *Osteoporosis Int* **14**, S16-S20 (2003).
51. Hirayama, M., *et al.* Aging effects of major and trace elements in rat bones and their mutual correlations. *Journal of trace elements in medicine and biology : organ of the Society for Minerals and Trace Elements* **25**, 73-84 (2011).
52. Yerramshetty, J.S. & Akkus, O. The associations between mineral crystallinity and the mechanical properties of human cortical bone. *Bone* **42**, 476-482 (2008).

53. Maguire, M.E. & Cowan, J.A. Magnesium chemistry and biochemistry. *Biometals* **15**, 203-210 (2002).
54. Musso, C.G. Magnesium metabolism in health and disease. *Int Urol Nephrol* **41**, 357-362 (2009).
55. Jahnen-Dechent, W. & Ketteler, M. Magnesium basics. *Clinical Kidney Journal* **5**, i3-i14 (2012).
56. Touyz, R.M. Magnesium in clinical medicine. *Front Biosci* **9**, 1278-1293 (2004).
57. Kayne, L.H. & Lee, D.B.N. Intestinal Magnesium Absorption. *Miner Electrol Metab* **19**, 210-217 (1993).
58. Quamme, G.A. & Dirks, J.H. The Physiology of Renal Magnesium Handling. *Renal Physiol Bioch* **9**, 257-269 (1986).
59. Byrd, R.P. & Roy, T.M. Magnesium: Its proven and potential clinical significance. *South Med J* **96**, 104-104 (2003).
60. Ford, E.S. & Mokdad, A.H. Dietary magnesium intake in a national sample of US adults. *J Nutr* **133**, 2879-2882 (2003).
61. Schlingmann, K.P., *et al.* Hypomagnesemia with secondary hypocalcemia is caused by mutations in TRPM6, a new member of the TRPM gene family. *Nat Genet* **31**, 166-170 (2002).
62. Voets, T., *et al.* TRPM6 forms the Mg2+ influx channel involved in intestinal and renal Mg2+ absorption. *The Journal of biological chemistry* **279**, 19-25 (2004).
63. Schmitz, C., *et al.* The channel kinases TRPM6 and TRPM7 are functionally nonredundant. *The Journal of biological chemistry* **280**, 37763-37771 (2005).
64. Mastrototaro, L., *et al.* Dietary Mg2+ regulates the epithelial Mg2+ channel TRPM6 in rat mammary tissue. *Magnesium research : official organ of the International Society for the Development of Research on Magnesium* **24**, S122-129 (2011).
65. Cao, G., *et al.* Regulation of the epithelial Mg2+ channel TRPM6 by estrogen and the associated repressor protein of estrogen receptor activity (REA). *The Journal of biological chemistry* **284**, 14788-14795 (2009).
66. Groenestege, W.M.T., Hoenderop, J.G., van den Heuvel, L., Knoers, N. & Bindels, R.J. The epithelial Mg2+ channel transient receptor potential melastatin 6 is regulated by dietary Mg2+ content and estrogens. *J Am Soc Nephrol* **17**, 1035-1043 (2006).
67. Elin, R.J. Assessment of magnesium status for diagnosis and therapy. *Magnesium Res* **23**, S194-S198 (2010).
68. Alfrey, A.C. & Miller, N.L. Bone Magnesium Pools in Uremia. *J Clin Invest* **52**, 3019-3027 (1973).
69. MacLeod, D. & Macleod, J. Magnesium: physiology and pharmacology. *Brit J Anaesth* **83**, 972-973 (1999).
70. Alfrey, A.C. & Miller, N.L. Bone magnesium pools in uremia. *The Journal of clinical investigation* **52**, 3019-3027 (1973).
71. Romani, A.M. Cellular magnesium homeostasis. *Archives of biochemistry and biophysics* **512**, 1-23 (2011).
72. Romani, A.M. & Scarpa, A. Regulation of cellular magnesium. *Frontiers in bioscience : a journal and virtual library* **5**, D720-734 (2000).
73. Moe, S.M. Disorders involving calcium, phosphorus, and magnesium. *Primary care* **35**, 215-237, v-vi (2008).
74. Zreiqat, H., *et al.* Mechanisms of magnesium-stimulated adhesion of osteoblastic cells to commonly used orthopaedic implants. *J Biomed Mater Res* **62**, 175-184 (2002).
75. Nadler, J.L., *et al.* Magnesium-Deficiency Produces Insulin-Resistance and Increased Thromboxane Synthesis. *Hypertension* **21**, 1024-1029 (1993).
76. Huerta, M.G., *et al.* Magnesium deficiency is associated with insulin resistance in obese children. *Diabetes Care* **28**, 1175-1181 (2005).
77. Paolisso, G., Scheen, A., Donofrio, F. & Lefebvre, P. Magnesium and Glucose-Homeostasis. *Diabetologia* **33**, 511-514 (1990).
78. Legrand, C., Okitolonda, W., Pottier, A.M., Lederer, J. & Henquin, J.C. Glucose-Homeostasis in Magnesium-Deficient Rats. *Metabolism* **36**, 160-164 (1987).
79. Bo, S. & Pisu, E. Role of dietary magnesium in cardiovascular disease prevention, insulin sensitivity and diabetes. *Curr Opin Lipidol* **19**, 50-56 (2008).
80. Rude, R.K. & Olerich, M. Magnesium deficiency: Possible role in osteoporosis associated with gluten-sensitive enteropathy. *Osteoporosis Int* **6**, 453-461 (1996).
81. Rude, R.K., *et al.* Dietary magnesium reduction to 25% of nutrient requirement disrupts bone

and mineral metabolism in the rat. *Bone* **37**, 211-219 (2005).
82. Rude, R.K. & Gruber, H.E. Magnesium deficiency and osteoporosis: animal and human observations. *The Journal of nutritional biochemistry* **15**, 710-716 (2004).
83. Rude, R.K., Singer, F.R. & Gruber, H.E. Skeletal and hormonal effects of magnesium deficiency. *Journal of the American College of Nutrition* **28**, 131-141 (2009).
84. Ryazanova, L.V., *et al.* TRPM7 is essential for Mg2+ homeostasis in mammals. *Nat Commun* **1**(2010).
85. Rude, R.K., Oldham, S.B., Sharp, C.F. & Singer, F.R. Parathyroid-Hormone Secretion in Magnesium-Deficiency. *J Clin Endocr Metab* **47**, 800-806 (1978).
86. Rude, R.K., Oldham, S.B. & Singer, F.R. Functional Hypoparathyroidism and Parathyroid-Hormone End-Organ Resistance in Human Magnesium-Deficiency. *Clin Endocrinol* **5**, 209-224 (1976).
87. Rude, R.K., *et al.* Low Serum Concentrations of 1,25-Dihydroxyvitamin-D in Human Magnesium-Deficiency. *J Clin Endocr Metab* **61**, 933-940 (1985).
88. Castiglioni, S., Cazzaniga, A., Albisetti, W. & Maier, J.A.M. Magnesium and Osteoporosis: Current State of Knowledge and Future Research Directions. *Nutrients* **5**, 3022-3033 (2013).
89. Lerner, U.H. The role of skeletal nerve fibers in bone metabolism. *Endocrinologist* **10**, 377-382 (2000).
90. Madsen, J.E., *et al.* Sensory nerve ingrowth during bone graft incorporation in the rat. *Acta orthopaedica Scandinavica* **67**, 217-220 (1996).
91. Cooper, R.R. Nerves in Cortical Bone. *Science* **160**, 327-& (1968).
92. Jones, K.B., Mollano, A.V., Morcuende, J.A., Cooper, R.R. & Saltzman, C.L. Bone and brain: a review of neural, hormonal, and musculoskeletal connections. *The Iowa orthopaedic journal* **24**, 123-132 (2004).
93. Hohmann, E.L., Elde, R.P., Rysavy, J.A., Einzig, S. & Gebhard, R.L. Innervation of periosteum and bone by sympathetic vasoactive intestinal peptide-containing nerve fibers. *Science* **232**, 868-871 (1986).
94. Mach, D.B., *et al.* Origins of skeletal pain: sensory and sympathetic innervation of the mouse femur. *Neuroscience* **113**, 155-166 (2002).
95. Buma, P., Verschuren, C., Versleyen, D., Vanderkraan, P. & Oestreicher, A.B. Calcitonin Gene-Related Peptide, Substance-P and Gap-43/B-50 Immunoreactivity in the Normal and Arthrotic Knee-Joint of the Mouse. *Histochemistry* **98**, 327-339 (1992).
96. Hill, E.L. & Elde, R. Distribution of CGRP-, VIP-, D beta H-, SP-, and NPY-immunoreactive nerves in the periosteum of the rat. *Cell and tissue research* **264**, 469-480 (1991).
97. Bliziotes, M., Gunness, M., Eshleman, A. & Wiren, K. The role of dopamine and serotonin in regulating bone mass and strength: studies on dopamine and serotonin transporter null mice. *Journal of musculoskeletal & neuronal interactions* **2**, 291-295 (2002).
98. Konttinen, Y., Imai, S. & Suda, A. Neuropeptides and the puzzle of bone remodeling. State of the art. *Acta orthopaedica Scandinavica* **67**, 632-639 (1996).
99. Elefteriou, F., *et al.* Serum leptin level is a regulator of bone mass. *P Natl Acad Sci USA* **101**, 3258-3263 (2004).
100. Manolagas, S.C., O'Brien, C.A. & Almeida, M. The role of estrogen and androgen receptors in bone health and disease. *Nature reviews. Endocrinology* **9**, 699-712 (2013).
101. Oury, F., *et al.* Endocrine Regulation of Male Fertility by the Skeleton. *Cell* **144**, 796-809 (2011).
102. Windahl, S.H., *et al.* Estrogen receptor-alpha in osteocytes is important for trabecular bone formation in male mice. *P Natl Acad Sci USA* **110**, 2294-2299 (2013).
103. Yadav, V.K., *et al.* A Serotonin-Dependent Mechanism Explains the Leptin Regulation of Bone Mass, Appetite, and Energy Expenditure. *Cell* **138**, 976-989 (2009).
104. Ducy, P. & Karsenty, G. The two faces of serotonin in bone biology. *J Cell Biol* **191**, 7-13 (2010).
105. Spencer, G.J., Hitchcock, I.S. & Genever, P.G. Emerging neuroskeletal signalling pathways: a review. *Febs Lett* **559**, 6-12 (2004).
106. Denhardt, D.T., Noda, M., O'Regan, A.W., Pavlin, D. & Berman, J.S. Osteopontin as a means to cope with environmental insults: regulation of inflammation, tissue remodeling, and cell survival. *Journal of Clinical Investigation* **107**, 1055-1061 (2001).
107. Takayanagi, H. Osteoimmunology and the effects of the immune system on bone. *Nat Rev Rheumatol* **5**, 667-676 (2009).
108. Irie, K., Hara-Irie, F., Ozawa, H. & Yajima, T. Calcitonin gene-related peptide (CGRP)-containing nerve fibers in bone tissue and their involvement in bone remodeling. *Microsc Res*

*Techniq* **58**, 85-90 (2002).
109. Imai, S., Tokunaga, Y., Maeda, T., Kikkawa, M. & Hukuda, S. Calcitonin gene-related peptide, substance P, and tyrosine hydroxylase-immunoreactive innervation of rat bone marrows: An immunohistochemical and ultrastructural investigation on possible efferent and afferent mechanisms. *J Orthopaed Res* **15**, 133-140 (1997).
110. Chiu, I.M., von Hehn, C.A. & Woolf, C.J. Neurogenic inflammation and the peripheral nervous system in host defense and immunopathology. *Nature neuroscience* **15**, 1063-1067 (2012).
111. Xanthos, D.N. & Sandkuhler, J. Neurogenic neuroinflammation: inflammatory CNS reactions in response to neuronal activity. *Nat Rev Neurosci* **15**, 43-53 (2014).
112. Ehrhard, P.B., Erb, P., Graumann, U. & Otten, U. Expression of Nerve Growth-Factor and Nerve Growth-Factor Receptor Tyrosine Kinase Trk in Activated Cd4-Positive T-Cell Clones. *P Natl Acad Sci USA* **90**, 10984-10988 (1993).
113. Lambiase, A., *et al.* Human CD4+ T cell clones produce and release nerve growth factor and express high-affinity nerve growth factor receptors. *J Allergy Clin Immun* **100**, 408-414 (1997).
114. Lucas, D., *et al.* Chemotherapy-induced bone marrow nerve injury impairs hematopoietic regeneration. *Nat Med* **19**, 695-+ (2013).
115. Pagani, F., *et al.* Sympathectomy alters bone architecture in adult growing rats. *J Cell Biochem* **104**, 2155-2164 (2008).
116. Cherruau, M., Facchinetti, P., Baroukh, B. & Saffar, J.L. Chemical sympathectomy impairs bone resorption in rats: A role for the sympathetic system on bone metabolism. *Bone* **25**, 545-551 (1999).
117. Hill, E.L., Turner, R. & Elde, R. Effects of Neonatal Sympathectomy and Capsaicin Treatment on Bone Remodeling in Rats. *Neuroscience* **44**, 747-755 (1991).
118. Offley, S.C., *et al.* Capsaicin-sensitive sensory neurons contribute to the maintenance of trabecular bone integrity. *J Bone Miner Res* **20**, 257-267 (2005).
119. Fujita, T. Biological Effects of Aging on Bone and the Central-Nervous-System. *Exp Gerontol* **25**, 317-321 (1990).
120. Takeda, S., *et al.* Leptin regulates bone formation via the sympathetic nervous system. *Cell* **111**, 305-317 (2002).
121. Zhang, M., Turner, R.T., Evans, G.L. & Sibonga, J.D. Effects of parathyroid hormone on bone formation in a rat model for chronic alcohol abuse. *J Bone Miner Res* **16**, S292-S292 (2001).
122. Qin, W.P., *et al.* The Central Nervous System (CNS)-independent Anti-bone-resorptive Activity of Muscle Contraction and the Underlying Molecular and Cellular Signatures. *Journal of Biological Chemistry* **288**, 13511-13521 (2013).
123. Elefteriou, F. Regulation of bone remodeling by the central and peripheral nervous system. *Archives of biochemistry and biophysics* **473**, 231-236 (2008).
124. Canalis, E., Giustina, A. & Bilezikian, J.P. Mechanisms of anabolic therapies for osteoporosis. *New Engl J Med* **357**, 905-916 (2007).
125. Seeman, E. & Delmas, P.D. Mechanisms of disease - Bone quality - The material and structural basis of bone strength and fragility. *New Engl J Med* **354**, 2250-2261 (2006).
126. Zebaze, R.M.D., *et al.* Intracortical remodelling and porosity in the distal radius and post-mortem femurs of women: a cross-sectional study. *Lancet* **375**, 1729-1736 (2010).
127. Hamann, C., Kirschner, S., Gunther, K.P. & Hofbauer, L.C. Bone, sweet bone-osteoporotic fractures in diabetes mellitus. *Nature Reviews Endocrinology* **8**, 297-305 (2012).
128. Jilka, R.L., Noble, B. & Weinstein, R.S. Osteocyte apoptosis. *Bone* **54**, 264-271 (2013).
129. Seeman, E. The structural and biomechanical basis of the gain and loss of bone strength in women and men. *Endocrin Metab Clin* **32**, 25-+ (2003).
130. Christiansen, C. Consensus Development Conference - Prophylaxis and Treatment of Osteoporosis. *American Journal of Medicine* **90**, 107-110 (1991).
131. Kanis, J.A., *et al.* Assessment of Fracture Risk and Its Application to Screening for Postmenopausal Osteoporosis - Synopsis of a Who Report. *Osteoporosis Int* **4**, 368-381 (1994).
132. Johnell, O. & Kanis, J. Epidemiology of osteoporotic fractures. *Osteoporosis Int* **16**, S3-S7 (2005).
133. Cummings, S.R. & Melton, L.J. Epidemiology and outcomes of osteoporotic fractures. *Lancet* **359**, 1761-1767 (2002).
134. Riggs, B.L. & Melton, L.J. The Worldwide Problem of Osteoporosis - Insights Afforded by Epidemiology. *Bone* **17**, S505-S511 (1995).

135. Compston, J., *et al.* Guidelines for the diagnosis and management of osteoporosis in postmenopausal women and men from the age of 50 years in the UK. *Maturitas* **62**, 105-108 (2009).
136. Kanis, J.A., *et al.* A new approach to the development of assessment guidelines for osteoporosis. *Osteoporosis Int* **13**, 527-536 (2002).
137. Ahmad OB, B.-P.C., Lopez AD, Murray CJL, Lozano R, Inoue M. Age standardization of rates: a new WHO standard. in *World Health Organization, Geneva* (2001).
138. Zhang, Z.Q., Ho, S.C., Chen, Z.Q., Zhang, C.X. & Chen, Y.M. Reference values of bone mineral density and prevalence of osteoporosis in Chinese adults. *Osteoporosis Int* **25**, 497-507 (2014).
139. Ahmad OB, B.-P.C., Lopez AD, Murray CJL, Lozano R, Inoue M. Age standardization of rates: a new WHO standard. *World Health Organization, Gene* (2001).
140. Zhu, H., *et al.* A survey of bone mineral density of healthy Han adults in China. *Osteoporosis Int* **21**, 765-772 (2010).
141. Hou SM, L.X., Xue J, Jian Y, Li WX, Yu H, Zhang YJ. Analysis of bone mineral density of healthy people in Shanxi of China. *J Fourth Mil Med Univ* **23:1115–1117**(2002).
142. Yeh LR, C.C., Lai PH. Normal bone mineral density in anteroposterior, lateral spine and hip of Chinese men in Taiwan: effect of age change, body weight and height. *J Chin Med Assoc* **67:287–295**(2004).
143. Nelson, D.A., Pettifor, J.M. & Norris, S.A. Race, Ethnicity, and Osteoporosis. *Osteoporosis, Vols I and Ii, 3rd Edition*, 667-687 (2008).
144. Qu, B., *et al.* The economic burden of fracture patients with osteoporosis in western China. *Osteoporosis Int* **25**, 1853-1860 (2014).
145. Vortkamp, A., *et al.* Recapitulation of signals regulating embryonic bone formation during postnatal growth and in fracture repair. *Mech Develop* **71**, 65-76 (1998).
146. Ferguson, C., Alpern, E., Miclau, T. & Helms, J.A. Does adult fracture repair recapitulate embryonic skeletal formation? *Mech Develop* **87**, 57-66 (1999).
147. Claes, L., Recknagel, S. & Ignatius, A. Fracture healing under healthy and inflammatory conditions. *Nat Rev Rheumatol* **8**, 133-143 (2012).
148. Kolar, P., Gaber, T., Perka, C., Duda, G.N. & Buttgereit, F. Human Early Fracture Hematoma Is Characterized by Inflammation and Hypoxia. *Clin Orthop Relat R* **469**, 3118-3126 (2011).
149. Chung, R., Cool, J.C., Scherer, M.A., Foster, B.K. & Xian, C.J. Roles of neutrophil-mediated inflammatory response in the bony repair of injured growth plate cartilage in young rats. *J Leukocyte Biol* **80**, 1272-1280 (2006).
150. Claes, L., Eckert-Hubner, K. & Augat, P. The effect of mechanical stability on local vascularization and tissue differentiation in callus healing. *J Orthopaed Res* **20**, 1099-1105 (2002).
151. Marsell, R. & Einhorn, T.A. The biology of fracture healing. *Injury* **42**, 551-555 (2011).
152. Claes, L.E. & Heigele, C.A. Magnitudes of local stress and strain along bony surfaces predict the course and type of fracture healing. *J Biomech* **32**, 255-266 (1999).
153. Granero-Molto, F., *et al.* Regenerative Effects of Transplanted Mesenchymal Stem Cells in Fracture Healing. *Stem Cells* **27**, 1887-1898 (2009).
154. Kitaori, T., *et al.* Stromal Cell-Derived Factor 1/CXCR4 Signaling Is Critical for the Recruitment of Mesenchymal Stem Cells to the Fracture Site During Skeletal Repair in a Mouse Model. *Arthritis Rheum* **60**, 813-823 (2009).
155. Cho, T.J., Gerstenfeld, L.C. & Einhorn, T.A. Differential temporal expression of members of the transforming growth factor beta superfamily during murine fracture healing. *J Bone Miner Res* **17**, 513-520 (2002).
156. Marsell, R. & Einhorn, T.A. The role of endogenous bone morphogenetic proteins in normal skeletal repair. *Injury* **40**, 4-7 (2009).
157. McKibbin, B. The biology of fracture healing in long bones. *The Journal of bone and joint surgery. British volume* **60-B**, 150-162 (1978).
158. Bassett, C.A. & Herrmann, I. Influence of oxygen concentration and mechanical factors on differentiation of connective tissues in vitro. *Nature* **190**, 460-461 (1961).
159. Einhorn, T.A. The science of fracture healing. *Journal of orthopaedic trauma* **19**, S4-6 (2005).
160. Claes, L. Biomechanical principles and mechanobiologic aspects of flexible and locked plating. *Journal of orthopaedic trauma* **25 Suppl 1**, S4-7 (2011).
161. Melnyk, M., Henke, T., Claes, L. & Augat, P. Revascularisation during fracture healing with soft tissue injury. *Archives of orthopaedic and trauma surgery* **128**, 1159-1165 (2008).
162. Hollevoet, N., Verdonk, R., Kaufman, J.M. & Goemaere, S. Osteoporotic fracture treatment.

*Acta Orthop Belg* **77**, 441-447 (2011).
163. Heini, P.F. The current treatment--a survey of osteoporotic fracture treatment. Osteoporotic spine fractures: the spine surgeon's perspective. *Osteoporosis international : a journal established as result of cooperation between the European Foundation for Osteoporosis and the National Osteoporosis Foundation of the USA* **16 Suppl 2**, S85-92 (2005).
164. Cheung, W.H., Chin, W.C., Qin, L. & Leung, K.S. Low intensity pulsed ultrasound enhances fracture healing in both ovariectomy-induced osteoporotic and age-matched normal bones. *J Orthopaed Res* **30**, 129-136 (2012).
165. Giannoudis P, T.C., Almalki T, et al. Fracture healing in osteoporotic fractures: is it really different? A basic science perspective. *Int J Care Inj* **38S1:S90–S99.**(2007).
166. Rubin, M.P., Chechurin, R.E. & Zubova, O.M. [Osteoporosis: diagnosis, current approaches to treatment, prophylaxis]. *Terapevticheskii arkhiv* **74**, 32-37 (2002).
167. Consensus development conference: diagnosis, prophylaxis, and treatment of osteoporosis. *The American journal of medicine* **94**, 646-650 (1993).
168. Riis, B.J. Biochemical markers of bone turnover. II: Diagnosis, prophylaxis, and treatment of osteoporosis. *The American journal of medicine* **95**, 17S-21S (1993).
169. Canalis, E., Economides, A.N. & Gazzerro, E. Bone morphogenetic proteins, their antagonists, and the skeleton. *Endocr Rev* **24**, 218-235 (2003).
170. Krishnan, V., Bryant, H.U. & MacDougald, O.A. Regulation of bone mass by Wnt signaling. *Journal of Clinical Investigation* **116**, 1202-1209 (2006).
171. Murray, T.M., Rao, L.G., Divieti, P. & Bringhurst, F.R. Parathyroid hormone secretion and action: Evidence for discrete receptors for the carboxyl-terminal region and related biological actions of carboxyl-terminal ligands. *Endocr Rev* **26**, 78-113 (2005).
172. Dempster, D.W., Cosman, F., Parisien, M., Shen, V. & Lindsay, R. Anabolic Actions of Parathyroid-Hormone on Bone (Vol 14, Pg 690, 1994). *Endocr Rev* **15**, 261-261 (1994).
173. Pickard, B.W., Hodsman, A.B., Fraher, L.J. & Watson, P.H. Type 1 parathyroid hormone receptor (PTH1R) nuclear trafficking: association of PTH1R with importin alpha1 and beta. *Endocrinology* **147**, 3326-3332 (2006).
174. Jingushi, S., Mizuno, K., Matsushita, T. & Itoman, M. Low-intensity pulsed ultrasound treatment for postoperative delayed union or nonunion of long bone fractures. *Journal of orthopaedic science : official journal of the Japanese Orthopaedic Association* **12**, 35-41 (2007).
175. Pilla, A.A., *et al.* Non-invasive low-intensity pulsed ultrasound accelerates bone healing in the rabbit. *Journal of orthopaedic trauma* **4**, 246-253 (1990).
176. Leung, K.S., *et al.* Low-Magnitude High-Frequency Vibration Accelerates Callus Formation, Mineralization, and Fracture Healing in Rats. *J Orthopaed Res* **27**, 458-465 (2009).
177. Ding, Y., Arai, M., Kondo, H. & Togari, A. Effects of capsaicin-induced sensory denervation on bone metabolism in adult rats. *Bone* **46**, 1591-1596 (2010).
178. Grant, A.D., Tam, C.W., Lazar, Z., Shih, M.K. & Brain, S.D. The calcitonin gene-related peptide (CGRP) receptor antagonist BIBN4096BS blocks CGRP and adrenomedullin vasoactive responses in the microvasculature. *Brit J Pharmacol* **142**, 1091-1098 (2004).
179. Leung, K.S., *et al*. Low-magnitude high-frequency vibration accelerates callus formation, mineralization, and fracture healing in rats. *Journal of orthopaedic research : official publication of the Orthopaedic Research Society* **27**, 458-465 (2009).
180. Zheng, L.F., *et al.* Calcitonin gene-related peptide dynamics in rat dorsal root ganglia and spinal cord following different sciatic nerve injuries. *Brain Res* **1187**, 20-32 (2008).
181. Erne, P., Schier, M. & Resink, T.J. The road to bioabsorbable stents: Reaching clinical reality? *Cardiovasc Inter Rad* **29**, 11-16 (2006).
182. Wang, Y.B., *et al.* Biodegradable CaMgZn bulk metallic glass for potential skeletal application. *Acta Biomater* **7**, 3196-3208 (2011).
183. Gu, X.N., *et al.* Corrosion of, and cellular responses to Mg-Zn-Ca bulk metallic glasses. *Biomaterials* **31**, 1093-1103 (2010).
184. Castellani, C., *et al.* Bone-implant interface strength and osseointegration: Biodegradable magnesium alloy versus standard titanium control. *Acta Biomater* **7**, 432-440 (2011).
185. Tamimi, F., *et al.* Biocompatibility of magnesium phosphate minerals and their stability under physiological conditions. *Acta Biomater* **7**, 2678-2685 (2011).
186. Chalmers, J., Gray, D.H. & Rush, J. Observations on the induction of bone in soft tissues. *The Journal of bone and joint surgery. British volume* **57**, 36-45 (1975).
187. Urist, M.R. Bone: formation by autoinduction. *Science* **150**, 893-899 (1965).
188. Holzer, P. Capsaicin: cellular targets, mechanisms of action, and selectivity for thin sensory

neurons. *Pharmacological reviews* **43**, 143-201 (1991).
189. Ishizuka, K., Hirukawa, K., Nakamura, H. & Togari, A. Inhibitory effect of CGRP on osteoclast formation by mouse bone marrow cells treated with isoproterenol. *Neuroscience letters* **379**, 47-51 (2005).
190. Valentijn, K., *et al.* Effects of calcitonin gene-related peptide on bone turnover in ovariectomized rats. *Bone* **21**, 269-274 (1997).
191. Huebner, A.K., *et al.* The role of calcitonin and alpha-calcitonin gene-related peptide in bone formation. *Archives of biochemistry and biophysics* **473**, 210-217 (2008).
192. Zaidi, M., Moonga, B.S. & Abe, E. Calcitonin and bone formation: a knockout full of surprises. *The Journal of clinical investigation* **110**, 1769-1771 (2002).
193. Naot, D. & Cornish, J. The role of peptides and receptors of the calcitonin family in the regulation of bone metabolism. *Bone* **43**, 813-818 (2008).
194. Doods, H., *et al.* Pharmacological profile of BIBN4096BS, the first selective small molecule CGRP antagonist. *Brit J Pharmacol* **129**, 420-423 (2000).
195. Castaneda-Corral, G., *et al.* The Majority of Myelinated and Unmyelinated Sensory Nerve Fibers That Innervate Bone Express the Tropomyosin Receptor Kinase A. *Neuroscience* **178**, 196-207 (2011).
196. Brain, S.D., Williams, T.J., Tippins, J.R., Morris, H.R. & Macintyre, I. Calcitonin Gene-Related Peptide Is a Potent Vasodilator. *Nature* **313**, 54-56 (1985).
197. Sakaguchi, Y., Sekiya, I., Yagishita, K. & Muneta, T. Comparison of human stem cells derived from various mesenchymal tissues - Superiority of synovium as a cell source. *Arthritis Rheum* **52**, 2521-2529 (2005).
198. Chang, H. & Tate, M.L.K. Concise Review: The Periosteum: Tapping into a Reservoir of Clinically Useful Progenitor Cells. *Stem Cell Transl Med* **1**, 480-491 (2012).
199. De Ugarte, D.A., *et al.* Comparison of multi-lineage cells from human adipose tissue and bone marrow. *Cells Tissues Organs* **174**, 101-109 (2003).
200. Dominici, M., *et al.* Minimal criteria for defining multipotent mesenchymal stromal cells. The International Society for Cellular Therapy position statement. *Cytotherapy* **8**, 315-317 (2006).
201. Jones, E. & McGonagle, D. Human bone marrow mesenchymal stem cells in vivo. *Rheumatology* **47**, 126-131 (2008).
202. Morikawa, S., *et al.* Prospective identification, isolation, and systemic transplantation of multipotent mesenchymal stem cells in murine bone marrow. *J Exp Med* **206**, 2483-2496 (2009).
203. Jacobs, J.W., Goodman, R.H., Chin, W.W., Dee, P.C. & Habener, J.F. Calcitonin Messenger-Rna Encodes Multiple Polypeptides in a Single Precursor. *Science* **213**, 457-459 (1981).
204. Amara, S.G., Jonas, V., Rosenfeld, M.G., Ong, E.S. & Evans, R.M. Alternative RNA processing in calcitonin gene expression generates mRNAs encoding different polypeptide products. *Nature* **298**, 240-244 (1982).
205. Rosenfeld, M.G., *et al.* Production of a novel neuropeptide encoded by the calcitonin gene via tissue-specific RNA processing. *Nature* **304**, 129-135 (1983).
206. Lu, J.T., *et al.* Mice lacking alpha-calcitonin gene-related peptide exhibit normal cardiovascular regulation and neuromuscular development. *Mol Cell Neurosci* **14**, 99-120 (1999).
207. McCoy, E.S., *et al.* Peptidergic CGRP alpha Primary Sensory Neurons Encode Heat and Itch and Tonically Suppress Sensitivity to Cold. *Neuron* **78**, 138-151 (2013).
208. Mrak, E., *et al.* Calcitonin gene-related peptide (CGRP) inhibits apoptosis in human osteoblasts by beta-catenin stabilization. *J Cell Physiol* **225**, 701-708 (2010).
209. Villa, I., *et al.* Effects of calcitonin gene-related peptide and amylin on human osteoblast-like cells proliferation. *Eur J Pharmacol* **409**, 273-278 (2000).
210. Cornish, J., *et al.* Comparison of the effects of calcitonin gene-related peptide and amylin on osteoblasts. *J Bone Miner Res* **14**, 1302-1309 (1999).
211. Wang, L.P., *et al.* Calcitonin-gene-related peptide stimulates stromal cell osteogenic differentiation and inhibits RANKL induced NF-kappa B activation, osteoclastogenesis and bone resorption. *Bone* **46**, 1369-1379 (2010).
212. Engler, A.J., Sen, S., Sweeney, H.L. & Discher, D.E. Matrix elasticity directs stem cell lineage specification. *Cell* **126**, 677-689 (2006).
213. Vogel, V. & Sheetz, M.P. Cell fate regulation by coupling mechanical cycles to biochemical signaling pathways. *Current opinion in cell biology* **21**, 38-46 (2009).
214. Baneyx, G., Baugh, L. & Vogel, V. Fibronectin extension and unfolding within cell matrix fibrils controlled by cytoskeletal tension. *P Natl Acad Sci USA* **99**, 5139-5143 (2002).

215. Eyckmans, J., Lin, G.L. & Chen, C.S. Adhesive and mechanical regulation of mesenchymal stem cell differentiation in human bone marrow and periosteum-derived progenitor cells. *Biology open* **1**, 1058-1068 (2012).
216. Nguyen, T.Y., Liew, C.G. & Liu, H.N. An In Vitro Mechanism Study on the Proliferation and Pluripotency of Human Embryonic Stems Cells in Response to Magnesium Degradation. *Plos One* **8**(2013).
217. Nguyen, T.Y., Garcia, S., Liew, C.G. & Liu, H.N. Effects of magnesium on growth and proliferation of human embryonic stem cells. *Ieee Eng Med Bio*, 723-726 (2012).
218. Kim, B.S., Kim, J.S., Park, Y.M., Choi, B.Y. & Lee, J. Mg ion implantation on SLA-treated titanium surface and its effects on the behavior of mesenchymal stem cell. *Mat Sci Eng C-Mater* **33**, 1554-1560 (2013).
219. Feske, S., Skolnik, E.Y. & Prakriya, M. Ion channels and transporters in lymphocyte function and immunity. *Nat Rev Immunol* **12**, 532-547 (2012).
220. Kasprowicz, J., *et al.* Inactivation of clathrin heavy chain inhibits synaptic recycling but allows bulk membrane uptake. *J Cell Biol* **182**, 1007-1016 (2008).
221. Shi, W.W., *et al.* Brain Tumor Regulates Neuromuscular Synapse Growth and Endocytosis in Drosophila by Suppressing Mad Expression. *J Neurosci* **33**, 12352-12363 (2013).
222. Wang, D., *et al.* Drosophila twinfilin is required for cell migration and synaptic endocytosis. *J Cell Sci* **123**, 1546-1556 (2010).
223. Henkel, A.W., Lubke, J. & Betz, W.J. FM1-43 dye ultrastructural localization in and release from frog motor nerve terminals. *P Natl Acad Sci USA* **93**, 1918-1923 (1996).
224. Zhou, H. & Clapham, D.E. Mammalian MagT1 and TUSC3 are required for cellular magnesium uptake and vertebrate embryonic development. *P Natl Acad Sci USA* **106**, 15750-15755 (2009).
225. Chokshi, R., Fruasaha, P. & Kozak, J.A. 2-Aminoethyl diphenyl borinate (2-APB) inhibits TRPM7 channels through an intracellular acidification mechanism. *Channels* **6**, 362-369 (2012).
226. Goytain, A. & Quamme, G.A. Identification and characterization of a novel mammalian Mg2+ transporter with channel-like properties. *Bmc Genomics* **6**(2005).
227. Kneussel, M. & Wagner, W. Myosin motors at neuronal synapses: drivers of membrane transport and actin dynamics. *Nat Rev Neurosci* **14**, 233-247 (2013).
228. Peng, A., Rotman, Z., Deng, P.Y. & Klyachko, V.A. Differential Motion Dynamics of Synaptic Vesicles Undergoing Spontaneous and Activity-Evoked Endocytosis. *Neuron* **73**, 1108-1115 (2012).
229. Slutsky, I., Sadeghpour, S., Li, B. & Liu, G.S. Enhancement of synaptic plasticity through chronically reduced Ca2+ flux during uncorrelated activity. *Neuron* **44**, 835-849 (2004).
230. Slutsky, I., *et al.* Enhancement of Learning and Memory by Elevating Brain Magnesium. *Neuron* **65**, 165-177 (2010).
231. Bowser, D.N. & Khakh, B.S. Two forms of single-vesicle astrocyte exocytosis imaged with total internal reflection fluorescence microscopy. *P Natl Acad Sci USA* **104**, 4212-4217 (2007).
232. Kozik, P., *et al.* A human genome-wide screen for regulators of clathrin-coated vesicle formation reveals an unexpected role for the V-ATPase. *Nat Cell Biol* **15**, 50-U105 (2013).
233. Monterroso, B., *et al.* Mg2+-Linked Self-Assembly of FtsZ in the Presence of GTP or a GTP Analogue Involves the Concerted Formation of a Narrow Size Distribution of Oligomeric Species. *Biochemistry-Us* **51**, 4541-4550 (2012).
234. Monterroso, B., Rivas, G. & Minton, A.P. An Equilibrium Model for the Mg2+-Linked Self-Assembly of FtsZ in the Presence of GTP or a GTP Analogue. *Biochemistry-Us* **51**, 6108-6113 (2012).
235. Schmitz, C., Deason, F. & Perraud, A.L. Molecular components of vertebrate Mg2+-homeostasis regulation. *Magnesium research : official organ of the International Society for the Development of Research on Magnesium* **20**, 6-18 (2007).
236. Zhou, H. & Clapham, D.E. Mammalian MagT1 and TUSC3 are required for cellular magnesium uptake and vertebrate embryonic development. *Proc Natl Acad Sci U S A* **106**, 15750-15755 (2009).
237. Wolf, F.I. & Trapani, V. MagT1: a highly specific magnesium channel with important roles beyond cellular magnesium homeostasis. *Magnesium research : official organ of the International Society for the Development of Research on Magnesium* **24**, S86-91 (2011).
238. Chubanov, V., *et al.* Disruption of TRPM6/TRPM7 complex formation by a mutation in the TRPM6 gene causes hypomagnesemia with secondary hypocalcemia. *P Natl Acad Sci USA* **101**, 2894-2899 (2004).

239. Jin, J., *et al.* Deletion of Trpm7 Disrupts Embryonic Development and Thymopoiesis Without Altering Mg(2+) Homeostasis. *Science* **322**, 756-760 (2008).
240. Li, Y.J. & Duckles, S.P. Effect of Age on Vascular Content of Calcitonin Gene-Related Peptide and Mesenteric Vasodilator Nerve Activity in the Rat. *Eur J Pharmacol* **236**, 373-378 (1993).
241. Kawasaki, H., Saito, A. & Takasaki, K. Age-Related Decrease of Calcitonin Gene-Related Peptide Containing Vasodilator Innervation in the Mesenteric Resistance Vessel of the Spontaneously Hypertensive Rat. *Circ Res* **67**, 733-743 (1990).
242. Chow, D.H.K., Leung, K.S., Qin, L., Leung, A.H.C. & Cheung, W.H. Low-Magnitude High-Frequency Vibration (LMHFV) Enhances Bone Remodeling in Osteoporotic Rat Femoral Fracture Healing. *J Orthopaed Res* **29**, 746-752 (2011).
243. Milgrom, C., *et al.* The Area Moment of Inertia of the Tibia - a Risk Factor for Stress-Fractures. *J Biomech* **22**, 1243-1248 (1989).
244. Augat, P., Reeb, H. & Claes, L.E. Prediction of fracture load at different skeletal sites by geometric properties of the cortical shell. *J Bone Miner Res* **11**, 1356-1363 (1996).
245. Eftekhari, M.H., Rostami, Z.H., Emami, M.J. & Tabatabaee, H.R. Effects of "vitex agnus castus" extract and magnesium supplementation, alone and in combination, on osteogenic and angiogenic factors and fracture healing in women with long bone fracture. *Journal of research in medical sciences : the official journal of Isfahan University of Medical Sciences* **19**, 1-7 (2014).
246. Xia, W. & Springer, T.A. Metal ion and ligand binding of integrin alpha5beta1. *Proceedings of the National Academy of Sciences of the United States of America* **111**, 17863-17868 (2014).
247. Namkung-Matthai, H., *et al.* Osteoporosis influences the early period of fracture healing in a rat osteoporotic model. *Bone* **28**, 80-86 (2001).
248. Hao, Y.J., *et al.* Changes of microstructure and mineralized tissue in the middle and late phase of osteoporotic fracture healing in rats (vol 41, pg 631, 2007). *Bone* **42**, 1240-1240 (2008).
249. Cheung, W.H., Chin, W.C., Qin, L. & Leung, K.S. Low intensity pulsed ultrasound enhances fracture healing in both ovariectomy-induced osteoporotic and age-matched normal bones. *Journal of orthopaedic research : official publication of the Orthopaedic Research Society* **30**, 129-136 (2012).
250. Fu, L., Tang, T., Miao, Y., Hao, Y. & Dai, K. Effect of 1,25-dihydroxy vitamin D3 on fracture healing and bone remodeling in ovariectomized rat femora. *Bone* **44**, 893-898 (2009).
251. Khalil, Z. & Helme, R. Sensory peptides as neuromodulators of wound healing in aged rats. *J Gerontol a-Biol* **51**, B354-B361 (1996).
252. Ohsawa, I., *et al.* Hydrogen acts as a therapeutic antioxidant by selectively reducing cytotoxic oxygen radicals. *Nat Med* **13**, 688-694 (2007).
253. Zheng, Y.F., Gu, X.N., Witte, F. Biodegradable metals. *Materials Science & Engineering R-Reports* **77**, 1–34 ( 2014).
254. Witte, F. The history of biodegradable magnesium implants: a review. *Acta biomaterialia* **6**, 1680-1692 (2010).
255. Gu, X.N., Xie, X.H., Li, N., Zheng, Y.F. & Qin, L. In vitro and in vivo studies on a Mg-Sr binary alloy system developed as a new kind of biodegradable metal. *Acta biomaterialia* **8**, 2360-2374 (2012).
256. Li, H.F., *et al.* In vitro and in vivo studies on biodegradable CaMgZnSrYb high-entropy bulk metallic glass. *Acta biomaterialia* **9**, 8561-8573 (2013).
257. Wang, Y.B., *et al.* Biodegradable CaMgZn bulk metallic glass for potential skeletal application. *Acta biomaterialia* **7**, 3196-3208 (2011).
258. Li, Z., Gu, X., Lou, S. & Zheng, Y. The development of binary Mg-Ca alloys for use as biodegradable materials within bone. *Biomaterials* **29**, 1329-1344 (2008).
259. Witte, F., *et al.* In vivo corrosion of four magnesium alloys and the associated bone response. *Biomaterials* **26**, 3557-3563 (2005).
260. Windhagen, H., *et al.* Biodegradable magnesium-based screw clinically equivalent to titanium screw in hallux valgus surgery: short term results of the first prospective, randomized, controlled clinical pilot study. *Biomedical engineering online* **12**, 62 (2013).
261. Crowther, C.A., Hiller, J.E., Doyle, L.W., Haslam, R.R. & Trial, A.C. Effect of magnesium sulfate given for neuroprotection before preterm birth - A randomized controlled trial. *Jama-J Am Med Assoc* **290**, 2669-2676 (2003).
262. Schick, V., *et al.* Effect of magnesium supplementation and depletion on the onset and course of acute experimental pancreatitis. *Gut* **63**, 1469-1480 (2014).
263. Lee, A.R., *et al.* Magnesium added to bupivacaine prolongs the duration of analgesia after

interscalene nerve block. *Can J Anesth* **59**, 21-27 (2012).
264. Bilir, A., Gulec, S., Erkan, A. & Ozcelik, A. Epidural magnesium reduces postoperative analgesic requirement. *Brit J Anaesth* **98**, 519-523 (2007).
265. Lees, K.R., *et al*. Magnesium for acute stroke (Intravenous Magnesium Efficacy in Stroke trial): randomised controlled trial. *Lancet* **363**, 439-445 (2004).
266. Lecrux, C., *et al*. Effects of magnesium treatment in a model of internal capsule lesion in spontaneously hypertensive rats. *Stroke* **39**, 448-454 (2008).

# Appendix

FACULTY OF MEDICINE
THE CHINESE UNIVERSITY OF HONG KONG
香港中文大學
醫學院

Tel 電話 : (852) 3943 6798
Fax 傳真 : (852) 2603 5011
E-mail 電郵 : aeec@med.cuhk.edu.hk
Homepage 網址 : http://www.aeec.med.cuhk.edu.hk

May 13, 2013

Professor Prof. QIN Ling
Dept of Orthopaedics and Traumatology
Faculty of Medicine

Dear Professor Qin,

Animal Experimentation Ethics Approval

I am pleased to confirm that the Animal Experimentation Ethics Committee agrees to grant ethical approval for your research project entitled "Intramedullary nail filled with osteoinductive pure Mg for enhancing bone fracture repair and the mechanism behind it" (Ref No. 13/003/MIS).

Please also note that the approval is for the procedures described in your application and variation from these procedures requires an additional endorsement from the AEEC.

Thank you for your attention.

Yours sincerely,

Professor LAN Hui Yao
Chairman
Animal Experimentation Ethics Committee

cc Director, Laboratory Animal Services Centre

*Serving the community through quality education, caring practice, and advancement of health sciences.*

(Appendix I)

***Papers***

Zhang Yifeng, Xu Jiankun et al. Implant-derived magnesium induces local neuronal production of CGRP to promote better bone fracture healing in rodent. (Under preparation)

***Conference abstracts***

Zhang Yifeng, Xu Jiankun et al. A novel fixative needle carried mg can promote fracture healing in Ovx rats. ORS Annual Meeting. 2015.3.28

(Appendix II)